UNDERSTANDING ELECTRODE MICROSTRUCTURAL INFLUENCE ON LITHIUM-SULFUR BATTERY

A Thesis

by

DARREN LAW

Submitted to the Office of Graduate and Professional Studies of
Texas A&M University
in partial fulfillment of the requirements for the degree of

MASTER OF SCIENCE

Chair of Committee,	Partha P. Mukherjee
Committee Members,	Hong Liang
	Sarbajit Banerjee
Head of Department,	Andreas A. Polycarpou

May 2017

Major Subject: Mechanical Engineering

ABSTRACT

The lithium ion battery is the center of attention for many electronic devices. However, its energy and power still cannot fully satisfy demand for transport vehicles and grid storage applications as its theoretical limit approaches. Additionally, its cathode materials can be costly and heavy. In response to this problem, lithium sulfur chemistry has arisen as a promising solution with its significantly higher capacity and energy density. Theoretically, a sulfur molecule S_8 accepts 16 electrons and reduces to S^{2-} ions, leading to a theoretical capacity of 1675.12 mAh/g of sulfur.

Although the Li-S cell exhibits a good theoretical capacity, the experimental performance of Li-S cells is quite poor compared to this thermodynamic limit. The Li-S cells are assembled with solid sulfur impregnated in a background carbon matrix. This sulfur dissolves during discharge and converts to insoluble lithium sulfide (Li_2S). During typical charging, the opposite process takes place, i.e., Li_2S dissolves and eventually forms solid sulfur. This in turn gives rise to electrode structure being evolved in time, thus leading to transport limitations and corresponding loss of performance.

A mathematical model is developed to simulate the electrochemical operation of Li-S cell. The cathode microstructure evolution is accounted for from microstructural characterizations using pore scale simulations. Different initial microstructural configurations are assigned based on different mean pore size and porosity. For a given

number of solid products, the time evolution is a strong function of this initial configuration.

The performance simulations explore the effects of different sulfur loading, charge-discharge rates and electrochemical operation windows for different cathode architectures. The results reveal the bottlenecks stemming out of pore blockage due to uneven precipitation. They further highlight the relative importance of electrochemical reaction rates and precipitation-dissolution kinetics.

ACKNOWLEDGEMENTS

I would like to thank my committee chair, Dr. Mukherjee, and my committee members, Dr. Banerjee, Dr. Liang, for their guidance and support throughout the course of this research.

CONTRIBUTORS AND FUNDING SOURCES

Contributors

This work was supported by a thesis committee consisting of Professor Partha P. Mukherjee and Hong Liang of the Department of Mechanical Engineering and Professor Sarbajit Banerjee of the Department of Chemistry.

Funding Sources

Graduate study was supported by the BakerRisk/Quentin and Jana Baker Graduate Fellowship, funded through the Texas A&M Foundation, and a faculty research initiation grant to Dr. Mukherjee from the Texas A&M Mechanical Engineering Department.

TABLE OF CONTENTS

LIST OF FIGURES

Page

LIST OF TABLES

Page

1. INTRODUCTION TO THE Li-S BATTERY

As pollution on earth began to post a serious threat to our environment, demand for renewable energy (e.g., wind, solar and hydro) increases. In present time, electric vehicle also began to gain more popularity due to environmental concerns. Hence, efficient and economical energy storage system is a necessity. Over the past decade, researchers performed countless experiments and modeling to study the mechanism of lithium battery. Lithium batteries have a wide range of applications in our daily life operations (e.g., cell phone and laptop). In a simplistic way, battery has two electrodes which are referred to anode and cathode. There is a wide range of materials which could be paired to create a working battery. Ideally, the most suitable pairing of anode and cathode materials should have a large potential difference as well as high capacity. Other factors such as the material availability in nature, material properties, manufacturing cost, and processing ability are equally essential to consider before selection. Recent years, researchers have taken interest in the lithium sulfur (Li-S) battery. Li-S battery was believed to be a promising candidate after lithium ion (Li-ion) battery. It has theoretical specific capacity of 1675 mAh/g and its theoretical energy density is 3 to 5 times higher than that of Li-ion battery [1]. Sulfur has some good elemental properties such as light weight, low cost and non-toxic. It is abundant in nature. Despite all these advantages, it also comes with disadvantages. Sulfur has a relatively low conductivity which is about $5x10^{-30}$ S/cm [2]. Compensating this exclusive property of sulfur, countless efforts were spent on it.

In general, Li-S cell has five main components similar to other lithium batteries and they are negative electrode, current collector, separator, positive electrode and electrolyte. The negative electrode or anode supplies electrons through the current collector to the positive electrode or cathode during discharge. The separator is an insulating material which only allows ion to travel between cathode and anode. The cathode usually holds the active material which is sulfur in Li-S cell. The electrolyte is usually a solvent contained with ionic salts such as lithium ions (Li^+). In Li-S cell, lithium metal is commonly used in the anode and the cathode comprised elemental sulfur, electronic conductors and binders [1]. Unlike Li-ion cell which works on intercalation, Li-S battery reaction mechanism is based on dissolution of polysulfides. Polysulfides are defined as S_x ($2 \leq x \leq 8$) and they are highly soluble. The chemical and electrochemical reactions of Li-S battery are shown below [3]:

$$Li \leftrightarrow Li^+ + e^- \quad (1)$$

$$\frac{1}{2}S_8^{2-} \leftrightarrow \frac{1}{2}S_{8(l)} + e^- \quad (2)$$

$$2S_6^{2-} \leftrightarrow \frac{3}{2}S_8^{2-} + e^- \quad (3)$$

$$\frac{3}{2}S_4^{2-} \leftrightarrow S_6^{2-} + e^- \quad (4)$$

$$S_2^{2-} \leftrightarrow \frac{1}{2}S_4^{2-} + e^- \quad (5)$$

$$S^{2-} \leftrightarrow \frac{1}{2}S_2^{2-} + e^- \quad (6)$$

$$S_{8(l)} \leftrightarrow S_{8(s)} \quad (7)$$

$$2Li^+ + S^{2-} \leftrightarrow Li_2S_{(s)} \quad (8)$$

Reaction 7 and 8 are chemical reaction while the rest are electrochemical reactions. In a typical Li-S cell discharge profile, the curve consists of two plateaus. Each plateau represents a set of electrochemical/chemical reactions. Figure 1 shows the discharge and charge curve of a Li-S cell.

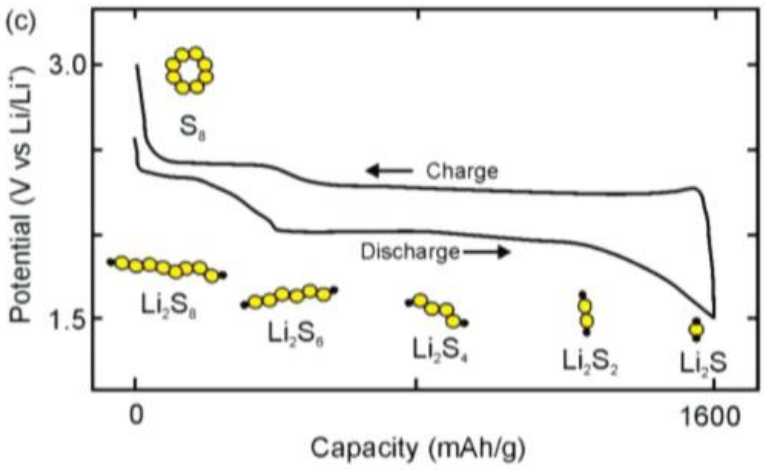

Figure 1. Discharge and charge curves of a Li-S cell [4]

Initially, S_8 is formed and turned into liquid form. As discharge continues, the polysulfides accept electrons and generate a lithium polysulfides which could be reduced to lower order lithium polysulfides. In upper plateau (2.3-2.4 V), lithium polysulfides Li_2S_x (x = 6 to 8) are generated while lower order lithium polysulfides Li_2S_x (x = 2 to 4) are generated at lower plateau (2.1V) [5]. Toward the end, precipitation occurs and

insoluble products such as Li_2S are formed. The nature of Li_2S is considered electrically insulating. Li_2S can accumulate over long period of cycling. When Li_2S are no longer electrochemically accessible, it will lead to loss of active material which results in capacity fading.

In the present time, Li-ion battery is widely available in the renewable energy market. However, Li-S battery has not been fully commercialized due to many issues and set back. Researchers still have not been able to reach its theoretical capacities. There are four main problems which influence the Li-S cell performance: (1) Dissolution of lithium polysulfides (2) Insulating nature of sulfur and Li_2S (3) Volume expansion in the cathode (4) Polysulfide shuttle effect. Many research efforts have been made to combat against these problems. The following four sections will discuss different methods in combating these problems in Li-S cell.

1.1 Challenges in Lithium-Sulfur Battery

1.1.1 Dissolution of Lithium Polysulfides

Long chained polysulfides are highly soluble and often diffuse through the separator to the negative electrode. Under chemical reactions, the lithium metal can react with the polysulfides which leads to a loss of active material. In response to this issue, many efforts have been made to mitigate the dissolution of lithium polysulfides [6]. Shin et al mentioned three different methods. First method is a protection layers or additives such as conductive polymer, nano-sized or mesoporous metal oxide, and graphene oxide were added to the cathode. Shin described this method can only partially suppress the dissolution of polysulfides since the process is thermodynamically favorable [6]. Second method focus mainly on the anode by providing a protective layer. Last method is the substitution or modification of electrolyte. Main goal of these method is to prevent polysulfides from dissolving into the electrolyte.

In an experimental study by Ji et al, a highly ordered nanostructured carbon-sulfur cathode was created. The cathode structure was coated with conductive polymer named polyethylene glycol (PEG) to further trap the trap the highly polar polysulfide species [7]. In the comparison study, cathode with PEG has an initial discharge capacity of 1320 mAh/g while regular cathode only achieved an initial discharge capacity of 1005 mAh/g. In addition, small fading was observed in the first 10 cycles. Although a high specific capacity was obtained for cathode coated with PEG, it is necessary to determine whether the improvement is related to the dissolution of polysulfides. Ji et al continued the study by measuring the percentage of sulfur found in electrolyte. It was observed that

the use of PEG reduced the amount of polysulfides from dissolving into the electrolyte. However, more than 20% of sulfur are found in the electrolyte of the PEG-coated cathode cell which implies PEG did not eliminate this problem.

Another experimental study was done by Song el al to mitigate the dissolution of polysulfides by adding additives. Song et al did an experimental study by adding nano-sized additives into the sulfur cathode. The nano-sized additives were believed to have polysulfide adsorbing effect and promote Li/S redox reaction. Song el al described the nano-sized additives was well mixed with other cathode components and has no side reactions. A performance comparison study was performed between cathode with and without the additives. The cathode with nano-sized additives was found to have an initial discharge capacity of 1185 mAh/g while the regular cathode has an initial discharge capacity of 741 mAh/g. The result implies the nano-sized additives did help to reduce the polysulfide dissolution into the liquid electrolyte by adsorbing polysulfides within the sulfur cathode [8]. Similar to previous experiment, a sulfur quantitative analysis was conducted to determine the amount of sulfur dissolved in the electrolyte. The same conclusion was observed from the previous study with the conductive polymer. $Mg_{0.6}Ni_{0.4}O$ showed its promising effect of adsorbing polysulfides but the issue continues to grow over many cycles. Another study was conducted with the use of nitrogen doping. Song et al introduced a novel cathode material called mesoporous nitrogen-doped carbon (MPNC)-sulfur nanocomposite to show nitrogen doping can effectively induce chemical adsorption of sulfur on the high surface area carbon framework [9]. Song et al investigated the adsorption of sulfur on MPNC using an X-ray

adsorption near edge structure spectroscopy (XANES). From the results, they found out that nitrogen doping promotes more chemical adsorption between sulfur and oxygen-containing functional groups. Using this phenomenon, they believed that sulfur can be immobilized due to oxygen-sulfur bonding. A higher specific capacity was achieved with MPNC-sulfur nanocomposite compared to that of those cathodes without nitrogen doping.

Other than using additives, another group also has created its own unique cathode material by using graphene oxide (GO). Ji et al successfully synthesized a GO-sulfur nanocomposites using heat treatment [10]. GO has multiple advantages such as accommodation of volume changes, promotion of electrical contact with sulfur and adsorption of sulfur. Ji et al mentioned GO contains variety of functional groups which have strong adsorption ability toward sulfur and prevent lithium polysulfide from dissolving into the electrolyte during cycling. Using transmission electron microscopy (TEM), the surface morphology of GO-S nanocomposites can be seen. Sulfur is homogenously dispersed into the GO surface and no significant bulk of sulfur was seen from the image. The GO-S nanocomposites achieved an initial discharge capacity of 1320 mAh/g at 0.02 C.

Though many efforts were made on the dissolution of polysulfides in Li-S cathode, considerable efforts were also made in that of the Li-S anode. Traditionally, many literatures have use lithium metal as the anode for Li-S cell. However, dendrite formation in Li anode is a great safety concern for Li anode as it causes short-circuit and other safety concerns within the cell. As mentioned before, a protection layer on lithium

metal could be a solution toward dissolution of polysulfides. Jing et al proposed a method by using a porous Al_2O_3. The porous Al_2O_3 serves as a protection layer which prevents side reaction between lithium polysulfides and Li anode. With the application of the protection layer, initial discharge capacity of 1215 mAh/g was achieved [11] which is higher than that of a regular anode. A study on the surface morphology was also conducted by Jing et al and surface morphology of protected lithium anode versus fresh lithium anode after 50 cycles was investigated. The fresh lithium anode contains multiple cracks on its surface which implies the frequent occurrence of side reactions. However, the protected lithium anode with layer has almost identical surface morphology which implies the suppression of side reactions between lithium polysulfides and lithium anode.

The last method in mitigating the dissolution of polysulfides is electrolyte modifications. Jin et al did an experimental study on the use of gel polymer electrolyte in Li-S cell. The gel polymer electrolyte (GPE) was prepared by combining ionic liquid based electrolyte into a porous membrane [12]. With the aid of GPE, the cell achieved an initial discharge capacity of 1217.7 mAh/g. Wen et al described the GPE might have slow down the dissolution of polysulfides into the anode side by reducing the solubility of lithium polysulfides in ionic-liquid based electrolytes. Though GPE seems to be a good solution, Shin et al proposed a different approach. In their experimental study, they used a concentrated electrolyte to mitigate polysulfide dissolution [13]. Zhang et al described the solubility of lithium polysulfides is affected by the concentration of lithium ions in the electrolyte due to the common ion effect. Therefore, high

concentration of lithium ions will lead to a decrease in the solubility of lithium polysulfides. A comparison study was conducted and the electrolyte with a higher concentration of Li salts has the highest initial discharge capacity and a lower amount of overcharge during the charge reaction. Further confirming the theory, Zhang et al let a lithium metal to dissolve in each electrolyte with concentration of Li salts at 0.05, 0.25 and 2.5 M. They found that the increase of concentration of Li salts leads to a decrease in the amount of polysulfides present in the electrolyte. From the experiment, it could be seen that high concentration of salts increases the viscosity of the electrolyte which results in a slower diffusion of polysulfides.

1.1.2 Insulating Nature of Sulfur and Li_2S

Sulfur itself has poor electrical conductivity like its insoluble product, Li_2S. Most common approach to this issue is to combine sulfur with high electronic conductivity materials. High electronic conductivity materials are important because agglomeration of Li_2S is not desirable. Not only these insoluble products cause an increase of internal resistance of the cell, it also causes fast capacity fading if left alone. In terms of high electronic conductivity, carbon is one of the most ideal material. Within the allotropes of carbon materials, activated carbon, carbon blacks, carbon nanotubes and graphene are the common substrates and additives used in experiments [4]. Other than its high electronic conductivity, carbon materials also have good specific surface area and porous. High surface area is desirable for sulfur cathode due to more electrical contact between the carbon and sulfur. Thus, more electrochemical reactions can occur. A porous structure is also important because it allows more sulfur to settle in and enhance

the overall specific energy density. Other conductive polymers include polyaniline, metal oxides and metal organic frameworks [4]. Pope et al tabulated a list of sulfur cathodes incorporated with different conductive materials and normalized many properties for comparison. Functional graphene sheet (FGS) was commonly used in experiments and it has the highest specific energy density (about 500 Wh/kg). High specific cathode capacity (about 1300-1450 mAh/g) can be found with in FGS, multi-walled carbon nanotubes (MWCNTs), polypyrrole (PPy) and sulfurized-polyacrylonitrile (S-PAN). It can also be seen that carbon materials have a higher S: A ratio compared that of the other conductive polymers such as S-PAN, polyaniline, and titanium disulphide (TiS) which implies carbon materials might be more porous.

1.1.3 Volume Expansion of Cathode

The volume expansion/contraction of the cathode is about 76% [2]. If agglomeration of insoluble product happens or loss of contact between sulfur and active area occurs, the structure can greatly expand. If polysulfides migrate away positive electrode, there will be a loss of material and the structure could collapse. Typically, the elastic substrates with preserved cavities or porous structure can help to deal with volume change of cathode [14]. As mentioned before, carbon materials provide good porous structure in this case. Though, it is noteworthy to mention that an appropriate porous structure is required since it could affect the amount of active material. The overall specific energy density can vary depending on the amount of active material.

1.1.4 Polysulfide Shuttle Effect

As time passes by, most batteries do not maintain its original state of charge even when they are left unused. Self-discharge is a common issue in the field of batteries. Li-S cell also has its own form of self-discharge and it goes hand in hand with the dissolution of polysulfides. During discharge, polysulfides are continuously forming at the cathode and causes a concentration gradient. Then, polysulfides can diffuse to the anode and chemical reaction occurs between lithium and low order polysulfides which eventually lead to the creation of Li_2S. As time proceed, concentration of these low order polysulfides increase and causes another concentration gradient. These lower order polysulfides diffuse back to cathode for oxidation to become high order polysulfides. Overtime, these polysulfides are diffusing back and forth during cell operation. This phenomenon is known as the polysulfide shuttle effect and it is known to cause corrosion of lithium anode and loss of active material. Several research groups have tried to combat this issue by adding different additives such as lithium nitrate ($LiNO_3$), lithium difluoro(oxalato) borate (LiDFOB) and lithium bis(oxalato) borate (LiBOB) into the electrolyte [15-17]. The most popular additive which is used in literature is $LiNO_3$ and it was claimed to suppress or reduce the polysulfide shuttle effect by forming a film that prevents the polysulfides to come in contact with lithium anode [18]. Literatures have reported improved performance over many cycles with the addition of $LiNO_3$. [15, 19, 20].

Wen et al performed a study on the addition of $LiNO_3$ in the electrolyte and concluded that an improved cycling efficiency was observed due to the protection film

generated on the lithium anode of the cell [15]. Not only did they found improved cycling efficiency, they also studied the cycling efficiency of lithium deposition and lithium dissolution on various amount of $LiNO_3$ in the electrolyte. 0.4M $LiNO_3$ seems to have the best cycling efficiency even when compared to that of no $LiNO_3$. It is also noteworthy to mention that 0.5M $LiNO_3$ has a lower cycling efficiency compared to that of 0.4M $LiNO_3$ which implies there might be an optimal value for $LiNO_3$. To further confirm the beneficial effect of $LiNO_3$, scanning electron microscopy (SEM) images of fresh lithium metal, lithium metal after cycling with $LiNO_3$ were also taken for comparison. A smooth and dense film can be seen on top of the lithium metal. In contrast, the lithium metal cycled with regular electrolyte has uneven surface. It is essential to mention that same amount of sulfur content was found in both regular electrolyte and $LiNO_3$ modified electrolyte. It suggests that $LiNO_3$ has no effect on the polysulfide dissolution.

Although $LiNO_3$ seems like a good solution toward polysulfide shuttle effect, other research groups have claimed that $LiNO_3$ might not be suitable due to the consumptions of $LiNO_3$ at lower potential [13, 21]. This lower potential limit could bring back the polysulfide shuttle effect when $LiNO_3$ is completely consumed. In addition, the cell will have a poorer performance. Zhang conducted a study on the cut-off voltage of Li-S cell with $LiNO_3$ modified electrolyte and found that reductions of $LiNO_3$ and Li_2S_2 occur when the cut-off voltage of the cell reach below 1.8 V after performing the cyclic voltammograms (CV) [13]. In addition, a galvanostatic cycling test was conducted to compare the capacity retention of the two cells by operating them

at 1.5-2.8 V and 1.8-2.8 V. At operating voltage of 1.8-2.8 V, the cell has a significant higher capacity retention over 100 cycles compared to that of the cell at operating voltage of 1.5-2.8 V. After Zhang's study, Rosenman et al further emphasized the need for a new suitable additive due to the irreversible consumption of $LiNO_3$ at lower potential (<1.9 V). With their electrochemical measurements, they found traces of nitrite ions in the cell which has a cut-off voltage of 1.7 V. The appearance of nitrite ions in the cell must be related to the reduction of nitrate ions. From galvanostatic cycling test, they also found out that around 29% of the initial nitrate concentration disappears after switching the cut-off voltage from 1.9 to 1.7. Rosenman et al concluded that nitrate ions were reduced to nitrite ions on the surface of the sulfur cathode at low potential (<1.9V) followed by reaction with electrolyte solution [21]. With the depreciation of nitrate ions which are used for the passivation of lithium anode, the polysulfide shuttle effect will occur.

Other than $LiNO_3$, LiBOB was also chosen as an alternative additive for improving Li-S cell performance. Xiong et al performed a study on the effect of LiBOB on Li-S cell and reached a discharge capacity of 1191 mAh/g with relatively small amount of LiBOB while maintain a reversible capacity of 756 mAh/g over 50 cycles [17]. From electrochemical measurements, two passivating films was found in the lithium anode with addition of LiBOB while one passivating film was found in the lithium anode without the addition of LiBOB. Based on an earlier observation from $LiNO_3$, a proper amount of LiBOB is needed for a better cell performance. The surface morphology of lithium anode with addition of LiBOB remains smooth and dense even

though it has a few minor holes which suggest that the passivation film was effective [17]. In addition to all these beneficial effects, the cell was operated at 1.7-2.4 V which is below the cut-off voltage limit (<1.9) for $LiNO_3$.

1.2 Components of Lithium-Sulfur Cell

After discussing the four main problems in Li-S cell, it is also worthwhile to explore the individual cell components found in literatures. As mentioned before, five main components of the Li-S cell are anode, current collector, separator, cathode and electrolyte. In the following five sections, the advantages and disadvantages of material substitutions and arrangement techniques for each component will be discussed.

1.2.1 Anode

Adequate research has been done on the anode of Li-S cell. Lithium metal is a common choice as anode material. However, there are problems come with lithium metal. Lithium anode is highly reactive material and side reactions often occur with electrolyte and polysulfides during cell operation. During cycling, it continuously reacts with lithium polysulfides which leads to the deposition of insoluble Li_2S. The results are lower capacity retention and cycle life. In addition, dendrite formation is a major concern for the use of lithium metal since it causes serious safety hazard. Researchers have suggested many alternative solutions for this undesirable problem of lithium anode. Common solution is a passivation layer on the Li anode which was mentioned before in previous sections. The passivation layer permeates Li ion to migrate outward and prevent further reactions with polysulfides. Other solution is a lithium sulfide (Li_2S)

cathode which could entirely eliminate the use of lithium metal as anode and be paired with a lithium-free anode materials [22]. Compatible lithium-free anode materials included Si, Sn and other alloy [14]. In an experimental study, Hassoun et al demonstrated the use of lithium-free anode materials by creating a Li-S cell with a silicon-carbon nanocomposite anode They were also capable of prelithiating the anode to avoid any undesired side reactions at the surface of the anode as well as of reaching optimal cell balance [23]. Another experimental study by Yang et al also used silicon nanowire anode. Silicon has a higher theoretical capacity compared to lithium but Yang et al mentioned that silicon nanowire undergoes 400% volume change during charging/discharge process. [22]. It is noteworthy to mention that Yang et al paired this lithium-free anode with a Li_2S cathode. Lastly, Fu et al did a different approach by using sandwiched electrodes. The configuration composed of pristine Li_2S powder in between two layers of self-weaving, binder free carbon nanotube electrodes [24]. This method has three benefits which are fast ion transport, efficient electron conduction and confining of discharge products within the sandwiched electrode upon cycling.

1.2.2 Current Collector

As cell operation began, current collectors provide a pathway for electrons to travel between cathode and anode. In most literature, copper (Cu) foil and aluminum (Al) foil are common materials used as current collectors in Li-S cell. Anode and cathode both have its own current collector. Cu foil is mainly used as current collector for anode while Al foil is used as current collector for cathode. Typically, both Cu foil and Al foil account for 15-20% by weight and 10-15% by cost of the entire Li-S battery

[25]. The weight of current collector is important because it provides more spaces for other components of the cell which might increases the overall specific energy density. Current collector should also remain attached to the electrodes for efficient transfer of electrons. Finally, it should remain chemically stable against other components within the cell when operated in a specific range of voltage. Otherwise, internal resistance of the cell could increase from the corrosion of the current collector which eventually lead to reduced cell performance.

Although Al foil was the common choice as current collectors, other materials have been used and tested in literatures. Recently, 3-dimensional (3D) current collectors have gain considerable popularity in the field of current collectors. Some examples of 3D current collectors include metal, graphene foams, woven or nonwoven mats of carbon fiber and carbon nanotubes [4]. Zhang's group used a metal cotton (MC) as current collector. Not only the MC serves as a current collector, Zhang el al mentioned that it serves as an electron transport network to improve the electronic conductivity of the cathode, a container to absorb the active material, a cage to retain polysulfides in the cathode region during cycling [26]. A wire-like structure was seen in SEM images. The MC structure is a very ductile and provides sufficient pore spaces for active materials while providing sufficient specific surface area for electrochemical reactions. It also helps during volume expansion as the structure is highly flexible. Sulfur was found to be mixed in uniformly with the MC structure. Other than metal, carbon material has also been studied as current collectors. Zhang el al did a study to compare Ni foam and carbon fiber cloth as current collectors [27]. Carbon fiber cloth can allow a high sulfur

content deposited in its 3D structure, which provides enhanced electronic conductivity [26]. Using Brunauer-Emmet-Teller (BET) measurements, Zhang et al determined that carbon fiber cloth has a higher specific surface area and a higher porosity than those of Ni foam. It implies that carbon fiber cloth can hold more sulfur material than Ni foam. Along with its flexible structure, it could also accommodate for volume expansion. Electrochemical performance study was also conducted to compare both Ni foam and carbon fiber cloth as current collectors. Li-S cell with carbon fiber clearly has a higher discharge capacity compared to that of Li-S cell with Ni foam. Zhang el al has further concluded that the high specific surface area of carbon fiber cloth could be the main reason for the increase of cell performance. In addition, the carbon fiber can act as adsorbents for polysulfides product from electrochemical reactions which is not possible for Ni-foam [26]. Thus, it prevents polysulfides from diffusing out of the cathode. Another carbon material which was found in literature is carbon nanotube. Cheng used a combination of Al foam and CNT as 3D current collectors for cathode [28]. Al foil does not provide good electrons transport as sulfur loading increases. Increase in sulfur loading implies a thicker electrode which makes diffusion of ions more difficult. Therefore, the electron pathway also becomes longer and more difficult to travel. However, the combination of Al foam and CNT can offers vast void space to accommodate huge amount of active materials and interconnected channels with short diffusion pathway and low resistance [28].

1.2.3 Separator

Separator is one of the most important part of the cell which serves as an insulator. It only allows ion to pass between cathode and anode while prohibit electrons from going through. Undesirable events such as short circuit of a cell could happen when the separator is failed to perform its function. Separators are mainly porous membranes which are made of glass-fiber or polyolefin materials [29]. The most commercially available separators are provided by Celgard. It provides variety of separators with different porosity and pore sizes. Celgard 2400 with 41% porosity and 0.043 μm pore size is overall the most popular choice, used in ~30% of the studies with a Celgard type separator [30]. In Li-S cell, the main challenge is preventing lithium polysulfides from diffusing through the separator to the anode. The dissolution of polysulfides and polysulfides shuttle effects go hand in hand with the selection of separator. In literature, there are some efforts toward the functionalization of separators. Two common methods include coating the separators either with lithium-conducting polymers or polysulfide absorbents. Zhang et al has reported coating a gel polymer electrolyte (GPE) onto a Celgard 3401 separator [31]. It was found the coating of GPE creates an adsorption layer which could adsorbs lithium polysulfides and traps them in the separator. Wei also reported enhanced cell performance using a separator modified with a polyvinylidene fluoride-carbon (PVDF-C) layer [32]. The PVDF-C layer confines polysulfides on the cathode side while promoting conductivity of the electrode.

1.2.4 Cathode

A cathode in a Li-S cell is composed of carbon substrate, elemental sulfur and binder. The selection of carbon family is important. Ideally, the carbon substrate should be porous and have sufficient active area. Active area can help to promote electrochemical reactions. Porous carbon substrate are classified into macrospores (pore diameter of > 50 nm), mesopores (2-50 nm) and micropores (<2 nm) [14]. Pores provide pathways for ions to travel through the entire electrode. Binder holds active material and conductive additives with its adhesive property.

1.2.4.1 Carbon Substrate

As mentioned before, conductive additives are vital in Li-S cell. Many research efforts have been done on using various conductive additive to increase cell performance from Pope et al review article. Carbon based substrate was commonly found in literature and used as part of the cathode to promote electronic conductivity of insulating sulfur and its insoluble products. It has good surface area which allows more electrical contact between sulfur and carbon. In the selection of carbon substrates, there are many factors to consider which could influence the overall cell performance. In general, those factors are pore size, porosity, tortuosity and specific surface area. Pore size usually define as the diameter of the pore. Most pore size is ranging from nanometer to micrometer for carbon substrates. Porosity is defined as amount of active material over the volume of the entire electrode. High porosity can accommodate more active material. Typically, carbon substrate can accommodate more sulfur than other materials. Although high

porosity is desirable, attention in mechanical stability could be at risk if porosity goes beyond a limit. Tortuosity is defined as the actual traveling distance between two points over the direct distance between those two points. For example, a tortuosity value of one implies that there is no obstacle in the path. Thus, the actual traveling distance between two points is the same as the direct distance between two points. This factor provides an insight on the difficulty of ions to travel from one place to another during diffusion process. Specific surface area is defined as available surface area over volume of the electrode. High specific surface area promotes better interaction or contacts between carbon and sulfur.

1.2.4.2 Binder

The role of a binder is important because it holds electrode materials and current collector altogether. A potential candidate of binder should have high adhesive property. Not only it holds the structure framework together, it also provides a good electric network between conductive carbon and active material. In literature, polyethylene oxide (PEO) and polyvinylidene fluoride (PVDF) are most commonly used binder in Li-S cell [2]. However, both binders have poor adhesion properties when used in Li-S cell [33].

Improving the adhesion properties, other materials have been used for testing. Sun et al used gelatin to replace PEO as a binder in Li-S cell. The gelatin was described to have great hydrophilic properties and is noticeably insoluble in common used organic electrolyte solvents which keeps the electrode stable [34]. In addition, gelatin makes a solution highly viscous which is great for adhesion agent for bonding. From

electrochemical measurements, Sun et al compared both gelatin and PEO as a binder. Both cells have equal proportion of active material, binder and carbon additive. The cell with gelatin was found to have a higher discharge capacity and cycle retention compared to that of the cell with PEO. The voltage drop at the second plateau is smaller for the cell with gelatin as a binder under different discharge rates. As mentioned, second plateau is highly associated with lithium polysulfides Li_2S_x (x = 2 to 4). Sun concluded that gelatin is highly effective as a dispersion agent which distributes sulfur and its soluble product homogenously [34]. Thus, it reduces agglomeration of polysulfides in the cathode during cycling. Bulk sulfur agglomerates can be seen in the morphology of the cathode. On the other hand, the cathode with gelatin has a homogenous distribution of cathode materials. In another study, Bao et al used Na-alginate as a binder for the sulfur cathodes and conducted a comparison study between Na-alginate and PVDF [35]. PVDF usually requires N-methy-2-pyrrolidone (NMP) as a solvent. However, NMP is described as toxic and vaporous organic solvents [35]. In addition, both PVDF and NMP are expensive and difficult to recycle. Similar to previous conclusion with the gelatin, Li-S cell with Na-alginate as a binder was found to have a better performance. From impedance measurements, Li-S cell with Na-alginate also has a lower resistance which implies better kinetics. Also, the morphology of Na-alginate sulfur cathode was found to be more porous than that of PVDF sulfur cathode. Sun et al mentioned that more porous structure is better for absorbing of the electrolyte and buffering of the volume changes [34].

Although binder is an important aspect in Li-S cell, there are experimental studies conducted on binder-free electrodes. Most of studies in binder-free electrodes believed that binder is not necessary in Li-S cell if sulfur can be well dispersed onto the conductive substrates. Sun et al confined sulfur nanocrystals in super-aligned carbon nanotube (SACNT) without the use of any binder while obtaining an initial specific capacity of 1071 mAh/g was obtained at 1C and a 85% capacity retention after 100 cycles [36]. Relying on superior properties of SACNT such as its porosity, adhesiveness, flexibility and unique network structures, the use of binder is eliminated. Elazari et al used a binder-free electrode by impregnating melted sulfur onto active carbon fiber cloth and achieved a higher initial capacity [37]. Lastly, Hagen et al also used melted sulfur to infiltrate into CNT without the use of binder [38]. Hagen et al claimed that high energy density can be achieved with binder-free electrode.

1.2.4.3 Elemental Sulfur

Sulfur is the active material used in Li-S cell. The amount of sulfur in the cathode is referred as sulfur loading in literature. Many researches claimed that a high sulfur loading is desirable because it could obtain a higher energy density. Typically, a cathode consists of 30 to 40% conductive agent and 10-20% binder which confines the sulfur loading to 50-60% [39]. It was found that there are more publications using a sulfur loading of 50% or higher in sulfur cathodes. However, almost half of the total publications used a sulfur loading of 50% or less. This indicates there might be a substantial reasoning for using low sulfur loading. Bruckner et al did a study on the influence of sulfur loading on cycle performance in Li-S cell [40]. Four sample cells

were prepared with sulfur loading of 20%, 40%, 60% and 80% with constant amount of electrolyte. All cells were tested for 200 cycles at C/5 or 2.5C. Lowest sulfur loading turns out to have the lowest capacity degradation. No significant sulfur utilization was seen at all for 80% sulfur loading. Cells with 20% and 40% sulfur loading has a fast degradation compared to that of the cell with 60% sulfur loading at C/2 which implies there might be an optimized value for sulfur loading. Bruckner stated that increasing sulfur content in the cathode can also decrease the sulfur utilization [40].

In preparation of sulfur cathode, integration of sulfur within the conductive substrate is also vital. A homogenously mixture of sulfur and conductive material is highly desirable because there are more electrical contacts. Thus, more sulfur can participate in the electrochemical reactions. On the opposite side, bulk sulfur is not desirable because some sulfur might not be utilized during process. There are many methods to prepare sulfur cathode. Manthiram et al conducted a review on various experimental techniques for sulfur carbon composite cathodes [41]. Table 1 shows a summary of experimental methods in literatures.

Method	Binding between S and C	features
Mixing	Weak	
Ball-milling	Medium	High energy ball milling
Thermal treatment	Strong	Good for mesoporous carbons Superficial sulfur removed by the second step
Heterogeneous nucleation	Very strong	Molecular infiltration Producing hazardous H_2S gas Involving the fewest chemicals

Table 1. Experimental preparation methods for sulfur carbon composite cathodes [41]

Mixing and ball-milling are not very effective in terms binding sulfur and carbon. On the other hand, thermal treatment and heterogeneous nucleation seems to have a stronger binding between sulfur and carbon. The thermal treatment is good for mesoporous carbon and it also provides good molecular infiltration. The heterogeneous nucleation uses a low cost and simple process which involves least number of chemicals for preparation. Ji et al heated sulfur to 155°C and mix it with a carbon material called CMK-3 [7]. The melting point of sulfur is 115°C. By heating sulfur to 155°C, the sulfur

can diffuse into the carbon substrate easily and creates a homogenous mixture. Bulk sulfur can be seen in SEM images. After heat treatment, the bulk sulfur completely disappears which indicates that the sulfur is effectively distributed throughout the CMK-3 channels. For heterogeneous nucleation method, Su et al synthesized a sulfur-carbon composite involving the precipitation of elemental sulfur at the interspaces between carbon nanoparticles in aqueous solution at room temperature [42]. Initially, carbon black (Super P) was suspended in the sodium thiosulfate ($Na_2S_2O_3$) solution. By adding hydrochloric acid (HCL), chemical reaction caused sulfur to precipitate into the interspaces of the carbon black. As time passed, carbon black particles also began to self-assemble to wrap around the sulfur particles. This experiment demonstrates a simple process of sulfur incorporation by using only a few chemicals.

1.2.4.4 Electrolyte

Electrolyte promotes ion transport between cathode and anode within the cell. A typical electrolyte consists of salt and one or more solvents. The main source of Li^+ comes directly from the salts in the electrolyte. Li^+ is a requirement to complete the electrochemical reactions. Example of salts used in Li-S cell are Lithium bis(trifluoromethanesulfonyl)imide (LiTFSI) and Lithium triflate (LiTf) [30]. Most salts are required to dissolve in one or more solvents. Some examples of solvents are 1,3 dioxolane (DOL), dimethoxyethane (DME) and tetraethylene glycol dimethyl ether (TEGDME) [33]. Generally, a good electrolyte for Li-S cells has some strict requirements. The requirements are high ionic conductivity, low viscosity, and low solubility of polysulfides, chemically stable [2]. High ionic conductivity allows efficient

transport of lithium ions. Low viscosity allows more electrolyte to move into the small pores of the electrode. Minimal solubility of polysulfides prevents the polysulfide shuttle effects. Chemical stability is important because electrolyte could react with lithium metal which causes the corrosion of anode. Electrolyte can split into multiple categories and they are liquid based, ionic liquid based and non-liquid based. Liquid based electrolyte has relatively low viscosity and it is simple to prepare [30]. It could easily penetrate the pores of the electrodes and promote good transport of ions. However, liquid based electrolyte is often associated with dissolution of polysulfides and the transport of the intermediate species between cathode and anode. Ionic liquid based electrolyte is mostly flame-retardant and non-vaporous [30]. Compared to liquid based electrolyte, it is safer to process and have less problems due to its great thermal properties. However, it is more viscous compared to liquid based electrolyte which implies a reduced ionic conductivity. Non-liquid electrolyte provides good mechanical stability, less risk of leakage and inhibit the polysulfide dissolution [30].

While there are all kinds of electrolyte, there is also study on the relationship between amount of electrolyte and cell performance. Bruckner et al did a study on the influence of amount of electrolyte in Li-S cell performance [40]. They initially made four cells with different amount of electrolyte. From their study, it was found that the cell with high amount of electrolyte has the best performance.

1.3 Lithium-Sulfur Cathode

Countless cathode structures have been experimented and compared over the years. A standardized approach is critically needed to fully understand the limits of cell performance in terms of microstructural effects. As mentioned in previous sections, Li-S cell has various problems such as the shuttling effect, volume expansion, dendrite formation…etc. Although many solutions and efforts were made to mitigate these problems, all evidences are pointing toward optimizing the morphology of the electrode. Therefore, it is important to investigate the morphology evolution of the electrode. It should be noted that this thesis will mainly focus on the cathode of Li-S cell. The main parameters which made up of the cathode are conductive additive, elemental sulfur and binder. The combination of these parameters can affect the pore volume, active area, tortuosity and effective conductivity of the cathode. During discharge, these microstructural properties can change over time. Before performing a parametric study, it is necessary to explore various cathode structures in the literatures to fully understand their unique properties.

Over the years, many researchers came up with various methods to improve Li-S cell performance. These methods mainly focus on the cathode of the cell because most people believe that it is the primary limiting factor in the performance of Li-S cell. Experimental methods include the use of additives, encapsulation of elemental sulfur, changing pore size and adjusting sulfur loading, and applying other conductive substrates. In the following sections, multiple cathode microstructures found in literatures will be discussed.

Many literatures have chosen allotropes of carbon as the cathode host due to their high electronic conductivity, high porosity and good pore sizes. These advantages create a suitable environment for sulfur as well as improve cell performance. In the following section, six different allotropes of carbon used in literatures will be discussed.

1.3.1 Graphene

Many literatures have reported improve cell performance with the implementation of graphene. Many researchers take its advantages of confining sulfur, promoting electronic conductivity and preventing the dissolution of polysulfide. Park et al was able to impregnate sulfur into graphene sheet and used it as the cathode of the Li-S cell [43]. The interspace between the graphene sheets is large so it can accommodate many sulfur particles. Using this feature along with other chemicals, Park et al could create many active sites which promote nucleation of sulfur on the graphene sheets and growth of sulfur particles. After sulfur impregnation process, it was found that the pore volume of the graphene has decreased from 1.08 cm^3/g to 0.05 cm^3/g which implies the graphene sheets were able to accommodate a good sulfur loading [43]. Through analysis, 83.3 weight% of sulfur and 16.7 weight% of carbon were detected [43]. It further supports the evidence that graphene sheets can accommodate many sulfurs. The BET surface area was found to be 305.4 m^2/g. Lastly, the electrical conductivity of the sulfur-graphene cathode was measured to be 1.0×10^1 S/cm which is better than that of typical sulfur-carbon cathode [43]. Electrochemical performance was compared between sulfur-graphene cathode and sulfur-carbon cathode. S-graphene cathode has a better discharge capacity compared to that of S-carbon cathode. Another experiment conducted by Xu et

al also utilized graphene sheets to wrap up the sulfur in a core shell structure [44]. The encapsulation method can mitigate polysulfides from dissolving outward to the electrolyte while accommodating volume expansion during discharge operation and providing efficient transport of lithium ions. In addition, there is extra void space in the shell structure which allows the sulfur particles to expand if needed. Similar to previous experiment by Park, 83.3 weight% of sulfur was encapsulated into the sulfur-graphene composite [44]. It is important to mention that the size of sulfur particles was uniform in the shell and the average size was estimated to be 2 μm. In terms of electrochemical measurements, the cynic voltammetry shows no large changes in increasing cycles. It could imply that the core shell structure does prevent dissolution of polysulfides into the electrolyte. Aside from sulfur graphene cathode, other researchers incorporated graphene in other carbon frameworks to create a hybrid structure. Three examples are sulfur/polyacrylonitrile (PAN)/graphene nanocomposite cathode [45], sulfur/PPy/graphene multi-composites cathode [46] and graphene/single-walled carbon nanotube cathode [47]. While some of them have better discharge capacity compared to its non-hybrid cathode, all three hybrid cathodes demonstrated good capacity retention over long period of cycling

1.3.2 Graphite

Sulfur/expanded graphite (EG) was studied by Li et al as a composite cathode [48]. Expanded graphite has a layered structure which has a good surface area. The spacing between each layer is about 2 nm to 10 μm but it was only able to take in 40 weight% of sulfur during preparation [48]. The BET surface area of expanded graphite

was found to be 19.5 m^2/g which is relatively low compared to that of graphene [48]. Li et al also studied the effect of heated S-EG composite cathode on electrochemical performance. Interestingly, the discharge capacity significantly decreased for the heated S-EG composite cathode. It is important to mention that the BET surface area was lower for the heated sample compared to that of non-heated sample which could might be the reason behind the difference in performance. Although the S-EG composite cathode was only able to have a 40 weight% sulfur loading, the discharge capacity of the first cycle at 100 mA/g was 1290 mAh/g. Zheng et al did a similar experiment in which they heated up sulfur to reduce graphite oxide [49]. GO is a layered structure with multiple oxide groups on each layer. The space between each layer is relatively small. Zheng et al reported the gap thickness between the layers is around 0.34 nm [49]. Heating the sulfur from room temperature to a high temperature, sulfur will turn from S_8 to S_2. When the sulfur becomes sulfur vapor, it could react with the oxide group on top resulting reduced GO and forming SO_2 gas. In gas form, more sulfur can easily intercalate into the reduced GO. At the end, Zheng et al were able to have a 52 weight% sulfur loading and confirm that the gap between the layers increased after sulfur intercalation [49].

1.3.3 Multi-Walled Carbon Nanotube (MWCNT)

MWCNT is notorious for its well electrical conductivity, thermal property and mechanical property. Han et al have reported the implementation of MWCNT in Li-S batteries was found to improve rate capabilities as well as cycle life of the cathode [50]. Han et al did a comparison study with two cathodes with/without MWCNT. It was found that the pore size of MWCNT is around 40 nm which makes the preparation process

difficult. Yuan et al mentioned that it is difficult to disperse sulfur into MWCNT during preparation which makes the application of MWCNT rather impractical [51]. However, its relative small pore size can prevent polysulfides from dissolving into the electrolyte. In addition, its tunnel like structure provide a better conductive network compared to other conductive additives. In Han's experiment, they compared the BET surface area between MWCNT and acetylene black. It was found that MWCNT has a BET area of 238 m^2/g while acetylene black has a BET area of 62 m^2/g [50]. It implies MWCNT has a relatively high surface area which is great for electrochemical reactions. The cathode with MWCNT addition has a better discharge capacity and capacity retention over 60 cycles. Another experiment conducted by Chen et al, they were able to enlarge pore size of the MWCNT to a range of 1-5 μm which allows a higher sulfur [52]. Chen et al utilized the function groups which are found along the carbon nanotubes to restrain the polysulfides. Using ball milling, sulfur and MWCNT were blended closely and a sphere-like structure was created. During cycling, the volume expansion can be accommodated by this structure. The sphere also traps polysulfide and prevent them from diffusing outward. In addition, it helps to trap some electrolyte in the cathode which could enhance the ion transport. Su et al also reported good electrochemical performance at high C-rate from a self-weaving sulfur carbon composite cathodes [53]. Using ultra-sonication, a bundle of MWCNT was put in a chemical solution to separate into different pieces. This allows sulfur to infiltrate into the MWCNT more easily. The morphology of the composite cathode was also compared before and after cycling over 50 cycles at 2C.

It was concluded that the morphology of composite cathode after cycling remains the same as that before cycling.

1.3.4 Carbon Blacks

Carbon blacks are also common conductive additive used in Li-S cathode. Jozwiuk et al did a comparison with various carbon blacks from different manufacturing companies [54]. The most popular carbon black seen in literature is Ketjenblack. In the experiment, Jozwiuk et al compared four different carbon blacks which are Printex-A, Super C65, Printex-XES and Ketjenblack EC-600JD [54]. The cathode has a sulfur to conductive additive ratio of 1.7 to 1. Comparing the BET surface area with all different carbon blacks, Ketjenblack has the highest BET surface area while Printex-A has the lowest BET surface area. The high surface area value might be the reason toward the popularity of Ketjenblack found in literatures. Looking further into the effect of carbon blacks on cell performance, electrochemical measurement was conducted over 200 cycles. Ketjenblack EC-600JD has the highest capacity retention as well as specific capacity. Jozwiuk et al concluded the increase in specific capacity might be related to high BET surface area. Further supporting this correlation, all four carbon blacks were put into vials and mixed with polysulfides solution. It was found that the adsorption of polysulfides is the highest for carbon black with high surface area [54]. Zheng et al have also performed a similar comparison study with four different carbon frameworks which include Ketjenblack, graphene, Acetylene Black (AB) and Hollow Carbon Nano Sphere (HCNS) [55]. Table 2 shows the BET surface area, pore volume and initial discharge capacity of all four carbon frameworks.

Carbon	**KB**	**Graphene**	**AB**	**HCNS**
Surface area/m^2g^{-1}	1576	890-1120	123.6	75.5
Total Pore volume cm^3g^{-1}	4.86	~6.2	0.53	0.38
C/S composite	**KB/S**	**Graphene/S**	**AB/S**	**HCNS/S**
Surface area/m^2g^{-1}	11.6	12	2.8	1.88
Total Pore volume cm^3g^{-1}	0.12	0.13	0.04	0.016
Initial discharge capacity at 0.2 C/mAh g^{-1}	1253	1117	1004	774

Table 2. BET surface area, pore volume and initial discharge capacity of KB, graphene, AB and HCNS [55]

KB has the highest BET surface area while second highest goes to graphene. Both KB and graphene have relatively good pore volume compared to the rest. After the input of elemental sulfur, KB and Graphene has almost the same value for BET surface area. However, it is evident that KB/S has the highest initial discharge capacity. This result further supports the positive relationship between surface area and discharge capacity. Higher surface area could provide more active sites for sulfur to react. Kim et al also mentioned that increasing surface area of carbon frameworks helps to promote sulfur utilization as well as lowering current density [56]. Thus, a higher discharge capacity is obtained.

1.3.5 Carbon Fibers

Carbon fibers have also gain attention recently due to its high electronic conductivity, porous structure and ability to confine polysulfides. Elazari et al reported a sulfur impregnated activated carbon fiber cloth (ACF cloth) as a binder free cathode [37]. The ACF cloth has a BET surface area of 2000 m^2/g while it is 1200 m^2/g after sulfur impregnation. The pore size of the ACF cloth was estimated to be less than 2 nm. It was also found that melted sulfur easily diffuses into the carbon fiber and settled in. After sulfur impregnation, the carbon framework almost remains unchanged. Interestingly, the discharge capacity increased for first six cycles and high capacity retention was achieved. Elazari et al concluded that the further reduction of the pore size and ACF cloth thickness can improved sulfur loading and utilization [37]. Thus, the overall discharge capacity will increase. Rao et al also incorporated carbon nanofibers (CNF) as part of the cathode materials [57]. In the study, a core shell structure was created and two cathodes with/without the addition of CNF were compared. It was found that the cathode with CNF has a faster kinetics for reaction. In electrochemical measurements, the cathode with CNF could reach 72% of the theoretical specific capacity for Li-S cell in the initial cycle. The cycle performance also showed that the cathode with CNF has a better capacity retention over 50 cycles. Rao et al concluded CNF provides a good electrical network which allow faster transport of ions into the electrode and good retention of polysulfides. Hollow carbon nanofiber (HCNF) also has been investigated by several groups. Zheng et al created a hollow carbon nanofiber encapsulated sulfur cathode [58]. Their research group believed in containment of

polysulfides and reduced contact between polysulfides and electrolyte are ways to mitigate the shuttle effect. They also believed that good electrical contact is required for insoluble products to prevent agglomeration. Based on those reasons, they designed a HCNF cathode. HCNF has a tunnel-like structure which accommodate more sulfur. The cathode was coated with an anodic aluminum oxide (AAO) membrane which prevents sulfur from depositing into the exterior of the carbon fibers. The sulfur is only able to have contact with the electrolyte in both ends of the tunnels while the carbon nanofibers has an intimate contact with the sulfur along the tunnel. Lithium ion can also travel into anywhere of the tunnel through the exterior of the carbon nanofibers which reduce the diffusion path and provide easily transport of electrons. Li et al also did a similar structure by using HNCF[59]. However, the sulfur was wrapped around the exterior of the HNCF. The pore diameter of the HNCF was reported to be 100 nm while Zheng et al reported a pore diameter of 200-300 nm for their HNCF. However, Li-S cell made by Li et al has a better discharge capacity compared to that of Zheng et al. In addition, Li et al only has a sulfur loading of 60.8 weight % while Zheng et al has a sulfur loading of 75 weight %. This result might imply the importance of pore diameter and sulfur loading. Lastly, Cao et al incorporated alginate fibers with carbon fibers and created a lotus root-like structured carbon fibers which are used to encapsulate sulfur [60]. Alginate fibers were carbonated and grinded together with potassium hydroxide (KOH). KOH is mainly used to activate the carbonated alginate fibers (ACF). As more KOH is added, the pore increase and the wall thickness the tube structure also decreases [60]. After heat treatment with other chemicals, final product was collected. Sulfur was deposited using

the melt diffusion strategy. The pore size of the carbon fibers is extremely small and the range is 1-50 nm. ACF cathode was described as a hierarchical pores structure. Four samples of ACF were made in different ratio of carbonated alginate fibers and KOH. It was found that ACF cathode with the most KOH has the highest BET surface area as well as pore volume. The highest discharge capacity was also found in the cathode with the most KOH. Cao et al concluded that large surface area provides better contact between sulfur and carbon fibers. With the hierarchical pores structures and even distribution of the sulfur, a high initial discharge capacity can be achieved.

1.3.6 Activated Carbon

Due to its high surface area after activation and easy preparation, activated carbon has gained popularity as cathode host materials. Active carbon is great choice of material due to its wide use in commercial applications and large scale production [61]. The preparation of activated carbon is cheap and the material used for the process is abundant in nature and good for environment [62]. Typically, KOH is a common chemical substance used in the activation of carbon [62-64]. Liang et al created a hierarchically structured carbon/sulfur nanocomposite using a soft template synthesis [63]. In the preparation process, mesoporous carbon (MPC) particles were used to mix with KOH and heat treated to 800 °C. After washing away any unwanted products, the heat-treated mixing was boiled in hydrochloric acid (HCl). The mixing was washed again and the final product is the activated MPC. Using BET method, it was found that the BET surface area of MPC before activation is 368.5 m^2/g which have significantly increased to 1566.1 m^2/g after KOH activation [63]. In addition, the pore volume and

pore diameter have increased. The carbon substrate which resulted from the activation process is a bimodal porous carbon. This bimodal porous carbon substrate contains features of both mesoporous carbon and microporous carbon. It allows a high sulfur loading which increase the overall energy density of the battery and retain polysulfides products within the small pores. Electrochemical measurements also show that the cell with bimodal porous carbon has a higher capacity retention and discharge capacity than that of the cells with mesoporous carbon and microporous carbon. Interestingly, seven samples containing bimodal porous carbon with different sulfur loading were also tested. It was found that low sulfur loading has the best discharge capacity. The sample with 11.7 weight% of sulfur loading has achieved an initial discharge capacity of 1584 mAh/g which is almost 94% of the theoretical capacity for Li-S battery [63]. Jiang has also reported activated carbon with ultrahigh specific surface area and large pore volume by adding litchi shells as part of the cathode material [64]. The specific surface area was found to be 3164 m^2/g and the pore size of the activated carbon is in the range of 5 to 10 μm in diameters. After incorporation of sulfur, no sign of sulfur agglomeration was observed. Two sulfur composites were made for electrochemical performance comparison. The sulfur composites with KOH as activation agent shows improved in performance as well as capacity retention. The improved performance was mainly contributed by the increased in surface area and pore volume. The high surface area provides a great conductive framework for the sulfur since sulfur is dispersed uniformly throughout the structure. In addition, large pore volume helps to accommodate more sulfur.

Other than activated carbon with ultrahigh surface area, commercial activated carbon products were also tested. Lee et al used three commercial activated carbon products, CXV, YP17D and 3S to test the performance as Li-S cathode materials based on their individual difference in BET surface area and pore volume and pore size distribution [61]. Table 3 shows the structural properties of all three commercial activated carbon products.

	BET SSA (m^2/g)	Pore Volume (cc/g)	Pore Size Distribution
YP17D	1586	0.80	0.7-2.5 nm
3S	971	0.78	0.7-30 nm
CXV	1488	1.27	0.8-30 nm

Table 3. Structural properties of YP17D, 3S and CXV as activated carbon [61]

YP17D has the highest BET surface area while CXV has the largest pore volume. The pore size distribution is relatively similar for 3S and CXV and YP17D has the smallest range. In the electrochemical performance study, it was found that 3S cathode has the best performance out of the three at room temperature despite having the lowest BET surface area. However, 3S cathode didn't have a good capacity retention compared to the others. Some reasons could be its relatively large pore size and low

surface area which cause its inability to confine polysulfides products over long cycling. Interestingly, the cell performance of the three samples changed significantly when the temperature was maintained at 70 °C. YP17D cathode with its high BET surface area has the highest discharge capacity. Lee et al concluded that the blockage in the pores is reduced at higher temperature and high temperature provides a better advantage for microporous activated carbon [61].

2. METHODOLOGY

Based on the literature review, an approach was created and used to determine microstructural effect on electrochemical performance of Li-S battery. A good and logical representation of the cathode is required. Using a commercial software called GeoDict, microstructure of the Li-S cathode can be created with different size, porosity, pore shape and percentage of conductive additives. After obtaining the microstructures, internal programs are used to calculate tortuosity, effective conductivity and active area of the microstructures. Additionally, an additional function in the interfacial area program allows user to add precipitation or secondary phase into the initial microstructure. Based on the calculated active area and tortuosity, comparison study was conducted to obtain correlations between transport properties and the microstructural properties. Lastly, cell discharge calculations were conducted to investigate the microstructural effects on Li-S cell performance. In the following sections, the steps toward obtaining the results will be discussed.

2.1 Microstructure Creation

GeoDict[65] is the primary software used to create the cathode microstructure. Not only GeoDict allows users to create multiple variation of microstructures, but it also provide a good 3D visualization. Creating a large-scale structure could be accurate but it could also be time consuming and inefficient in computation. Therefore, smaller scale structure within reasonable range of accuracy was considered. A statistical study on the

microstructure size was conducted beforehand to ensure the results are similar to each other.

Microstructure can be created in GeoDict with various sizes, shapes and forms. Based on literature review, most Li-S cathodes from experiment were found to have spherical pores which encapsulate the active material, sulfur. Therefore, a spherical pore structure was used as the base model in GeoDict. In the parametric study, initial porosity of the cathode is selected to be 60%, 70%, 80% and 90%. Initial porosity is high because most Li-S cathodes from literature have reported to have more than 50% sulfur loading. Typical range of pore sizes found in literature is 0.5 μm to 10 μm. Table 4 shows the values used for the parametric study.

Initial Porosity (%)	60, 70, 80, 90
Conductive Additive (%)	10, 20, 30, 40
Precipitation Addition (%)	0, 10, 20, 30, 40, 50
Pore Size (μm)	1, 5, 10

Table 4. Initial porosity, mean pore diameter and precipitation addition

In microstructure modeling process, the size of the structure can be adjusted with box size and voxel length. The box size represents the number of boxes which made up of the entire structure and it can be adjusted in x, y and z directions. Voxel length represents the length of a single box. For example, a voxel length of 1 μm and box size of 100 would be a structure composed of 100 x 100 x 100 boxes and each box has a length of 1 μm. After creating the microstructure, three internal programs were used to calculate the active area, tortuosity and effective conductivity of the cathode microstructure. Before going in details for the next step, the functions of the three internal programs will be discussed.

2.2 Secondary Phase Addition and Interfacial Area

Active area defines as the electronically conductive reaction sites for electrochemical reactions to take place. The two main functions of the program are to add volume percentage of secondary phase into the initial microstructure and to calculate the interfacial area at different intervals. In the program, there are six input parameters as shown in Table 5.

Number of boxes in x-direction	Mx
Number of boxes in y-direction	My
Number of boxes in z-direction	Mz
Energy Partition Coefficient	W2ndry
Volume percent of secondary phase	vol2
Number of simultaneous deposition sites	Nsimultaneous

Table 5. List of input parameters for interfacial area program

In the microstructure modeling, Mx, My and Mz are known parameters. These three parameters allow the program to determine the dimensions of the microstructure. vol2 allows user to add a percentage of secondary phase into the microstructure. As mentioned in the literature review, the precipitate forms during chemical reaction in Li-S cell is Li_2S. Therefore, the secondary phase is considered as solid sulfur and Li_2S in this program. As deposition increases, concentration of solid sulfur and Li_2S increases which lead to the agglomeration of Li_2S or surface passivation. Determining the location of the precipitates, Energy Partition Coefficient and simultaneous deposition sites were implemented. The Energy Partition Coefficient provides a preference of where the precipitates settle. The simultaneous deposition sites are the total amount of site where the precipitates simultaneously settle in the microstructure. Initially, the program reads a microstructure data file and provides a coordinate number for every box. The

microstructure data file consists of multiple layers of numbers. When the layers combined, it becomes a three-dimensional matrix. There are two numbers, 1 and 0 where 1 is defined as primary phase or conductive material and 0 is defined as empty space or pore. As it reads the data file, the program checks for the available sites by considering x, y, z directions of the microstructure. A site is only considered as a candidate if it is a conductive material with empty space as neighbors. Otherwise, empty space with no conductive material as a neighbor cannot be considered as candidate site. When available deposition sites were found, the number 0 or empty space becomes 2 where 2 represents the precipitate. In nature, precipitation occurs in random location and it is rather difficult to predict its location. Therefore, a random number generator was also included as part of the program to randomize the sites which the precipitates settle. Aside from becoming a site candidate, the program has an additional deposition requirement. Energy values are assigned to individual site. The energy values vary based on the location and site with high energy values are more likely to be selected. Although this method is good, there is also a problem. The energy values changes as precipitates are deposited at each iteration. The structure before and after an iteration has different energy values. Therefore, it is necessary to sum up all energy values to create a linear relationship for all iterations.

The program also records the number of interfacial faces at a specific percentage of precipitation addition. There are three possible interfacial faces in the microstructure after precipitation addition. First interfacial face is between conductive additive and empty space. Second interfacial face is between conductive additive and precipitate.

Third interfacial face is between empty space and precipitate. After obtaining the number of interfacial faces, a function was made to calculate the total interfacial area between 0, 1 and 2. The number of interfaces at each face provide information to active area and surface passivation. Before calculating the specific area for each phase, it is necessary to understand the composition of an irregular shape (i.e. Sphere). Assuming a sphere with a fine and detailed resolution, its general shape is perceived as sphere. Though in reality, the sphere consists of many boxes as the resolution of the sphere decreases. If the volume of the sphere and the box (Mx by My by Mz) are known, it is possible to approximate the number of boxes to fill up the entire spheres. With this analogy, it is possible to correlate resolution, surface area of the sphere and the number of interfacial faces altogether. An equation was formulated to calculate the specific dimensionless area of each interfacial face and it is defined as,

$$a_{ij} = \frac{4\pi(128^2)(R)f_{ij}}{308598(Mx * My * Mz)}$$

where a_{ij} is the interfacial area, R is the radius of spherical pore and f_{ij} is the total number of the interfacial faces. It should be noted that the constants are found based on a statistical study performed internally.

2.3 Tortuosity and Conductivity

Tortuosity is a dimensionless quantity which is largely associated with morphology of porous electrode. It determines the effective diffusivity in the governing equations such as material balance and charge conversation. Tortuosity provides information of ion travel paths. Similar to previous program, this program also uses the number 0, 1 and 2 for pore, conductive material and precipitate, respectively. The difference is that it calculates tortuosity for the new microstructure generated by the previous program. The new microstructure contains precipitation addition. There is a total of six input parameters for the program as shown in Table 6.

Number of boxes in x-direction	Mx
Number of boxes in y-direction	My
Number of boxes in z-direction	Mz
Diffusivity of empty space	D0
Diffusivity of conductive material	D1
Diffusivity of precipitate	D2

Table 6. Input parameters for tortuosity program

To calculate tortuosity, D0 was set to 1 while D1 and D2 were set to 0. The reason is that conductive material and precipitate are considered as “physical barriers” in the travel path of the ions. Initially, the program determines the porosity of the microstructure since each microstructure could contain various percentage of precipitation addition. Then, it assigns the D0, D1 and D2 to each material phase of the microstructure. Afterward, it begins to calculate the tortuosity in x, y and z direction by solving a diffusion equation and it is defined as,

$$\nabla \cdot (D\nabla c) = 0$$

where D is diffusivity and c is concentration. Accounting for a specific direction (x, y or z) of tortuosity, insulated boundaries are imposed at other faces of the cube. For boundary conditions, the initial concentration of one face was set to 1 while the opposite face was set to 0 to create a concentration gradient. Solving for the concentration, a concentration expression is obtained which could be used in Flick’s law of diffusion to find the tortuosity. Equation X shows Flick’s law of diffusion.

$$J = -D\frac{\varepsilon}{\tau_n}\frac{\partial c}{\partial n}$$

where J is the molar flux, D is the diffusivity, ε is the porosity of the microstructure and τ_n is the tortuosity in x, y or z direction. Tortuosity is the only unknown parameter in the equation. Figure 2 show the samples of concentration fields of a microstructure in x, y and z direction.

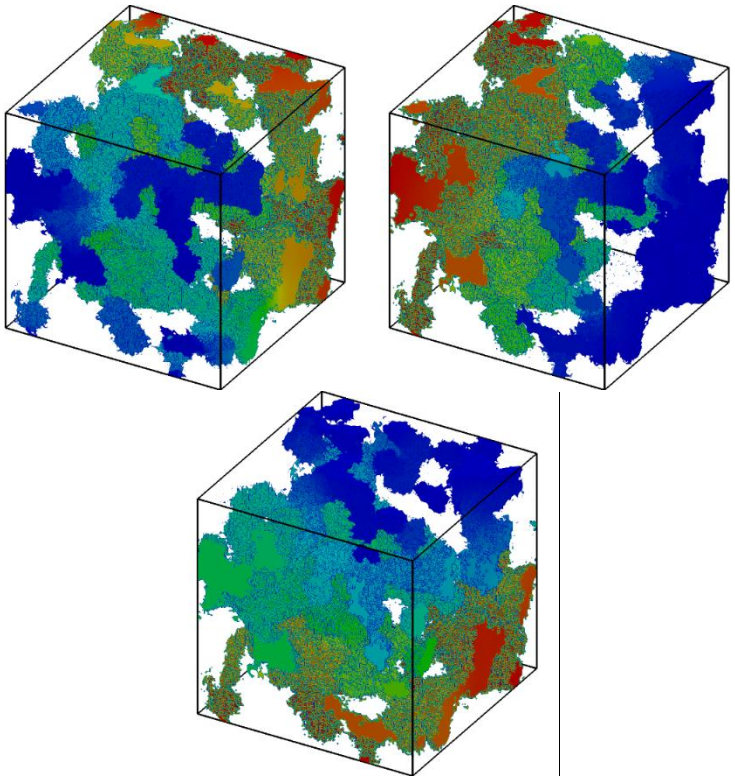

Figure 2. x, y, z concentration fields of a microstructure (Top to bottom)

As seen in Figure 2, the concentration gradient only goes from high (red) to low (blue) in a specific direction. Similar technique was used to calculate conductivity. However, D1 was set to 1 while D0 and D2 were set to 0. In the microstructure, conductive material has a higher electronic conductivity compared to that of precipitates and empty space. As mentioned before, precipitate has an insulating property in Li-S cell. It should be noted that D1, D0 and D2 do not represent diffusivities anymore in conductivity case. The two equations used for conductivity calculation are

$$\nabla \cdot (\sigma \nabla \phi) = 0$$

$$J = -\sigma_n \frac{\partial \phi}{\partial n}$$

where σ is conductivity, σ_i is conductivity in x, y, or z direction and ϕ is potential. The boundary is similar to tortuosity calculation. One face of the cube has a potential of 1 and its opposite face has a potential of 0. All other faces have an insulated boundary conditions. Figure 3 shows the potential fields of a microstructure in x, y, z direction.

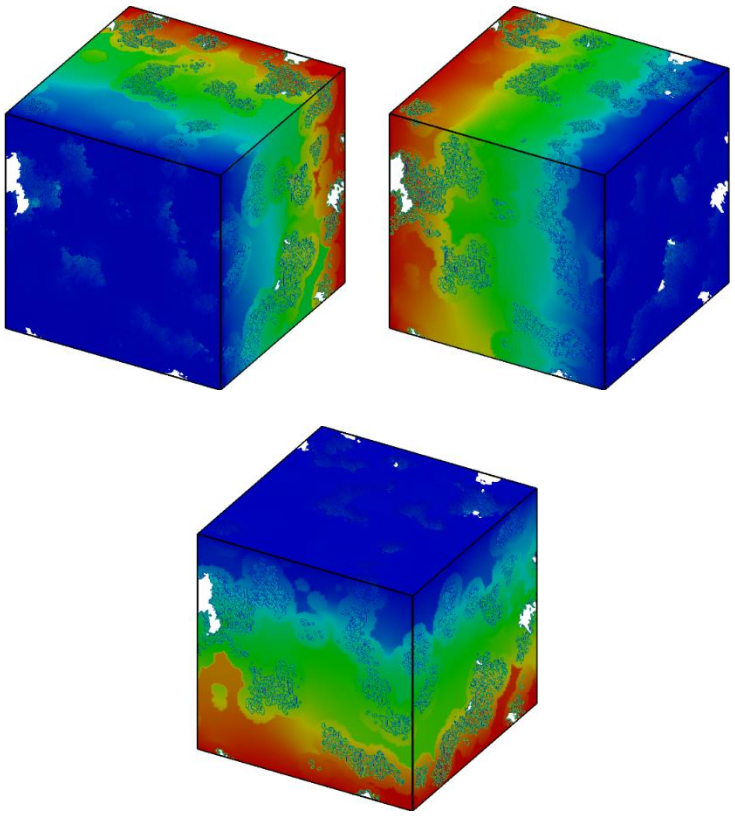

Figure 3. x, y, z potential fields of a microstructure (Top to bottom)

Herein, the potential goes from high (red) to low (blue) in one direction similar to previous figure.

2.4 Microstructure Statistical Study

The purpose of this statistical study was conducted to determine a logical resolution for the microstructure model. Voxel length and box size are the two main factors to study first. In addition to those studies, microstructures are also randomly generated in GeoDict with the same set of parameters to check if the results are

consistent. It should be noted that all microstructures followed a set of conditions throughout the entire study as shown in Table 7.

Initial porosity	80%
Mean pore radius	10 μm
Precipitation addition	50%
Energy partition coefficient (w)	0.5

Table 7. Conditions for microstructure statistical study

Eight parameters were studied and compared for accuracy and consistency. Table 8 shows the eight parameters for the statistical study.

Area 01	a01
Area 12	a12
Area 20	a20
Tortuosity	τ
Conductivity	σ
Porosity	ε_0
Conductive material	CM
Precipitation Addition	ε_2

Table 8. Parameters for statistical study

Area 01 represents the effective interfacial active area in the microstructure. Area 12 represents the interfacial area between conductive material and precipitates. Area 20 represents the interfacial area between precipitates and pore space. As precipitation addition increases, area 12 and area 20 also increase.

2.4.1 Statistical Study: Voxel Length

Six microstructures with different voxel lengths were created while total voxel length of the microstructure remains constant. Figure 4 shows the 3D models of the six microstructures.

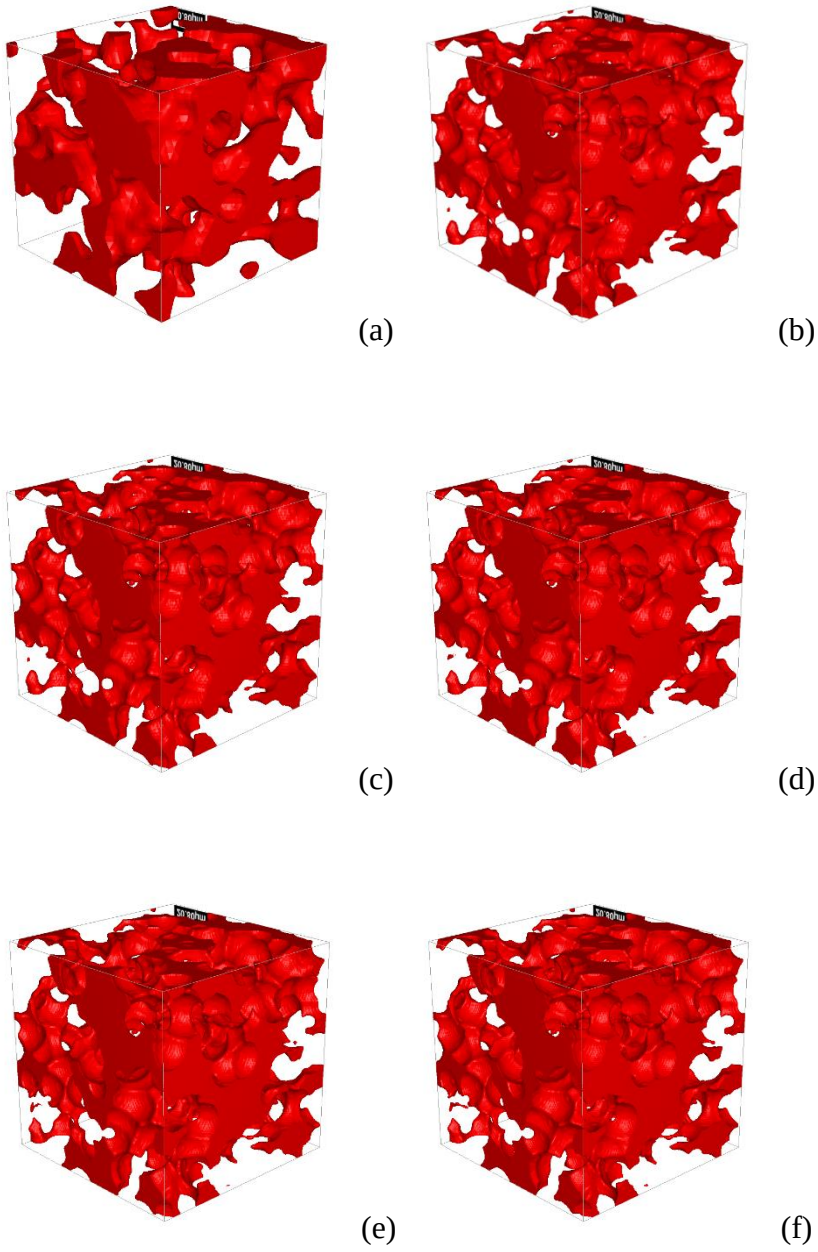

Figure 4. Microstructure with voxel length of (a) 5/2 (b) 5/4) (c) 1 (d) 5/6 (e) 5/7 (f) 5/8

The red represents the conductive material and the white represents the pore space. As the voxel length goes down, the resolution of the microstructure becomes finer. Comparing 4(a) to 4(f), the microstructure clearly has a better resolution and more details. Table 9 shows the values for each parameter in voxel length statistical study.

Voxel length	a01	a21	a20	τ	σ	ε_0	CM	ε_2
5/2	0.02	0.75	1.45	6.13	0.03	29.38	19.93	50.67
5/4	0.01	0.86	1.83	4.42	0.04	29.40	19.89	50.70
1	1.134E-04	0.88	1.92	3.78	0.04	29.85	19.88	50.26
5/6	4.633E-06	0.89	1.97	3.72	0.04	29.37	19.86	50.75
5/7	6.808E-06	0.89	1.99	3.46	0.05	29.80	19.87	50.31
5/8	0	0.90	2.01	3.42	0.05	29.34	19.87	50.78

Table 9. Voxel length statistical study

The average tortuosity decreases as the voxel length decreases. Voxel length from 1 to 5/8 has similar values from 3.4 to 3.7 while voxel length for 5/2 and 5/4 are at completely out of range. Other similar trends can be observed in conductivity, area 21 and area 20. Thus, it can be concluded that a voxel length of 1 is considered as a fair

value to be used for the performance study because it retains a good resolution and it has similar values with other microstructures. The overall percentages distribution for conductive material, precipitation addition and final porosity are also very close to each other. This result shows that the interfacial area program and GeoDict have consistent values during microstructure creation.

2.4.2 Statistical Study: Box Size

In this study, a voxel length of 1 was used while all other parameters remain the same. Figure 5 shows the five microstructures with various box size.

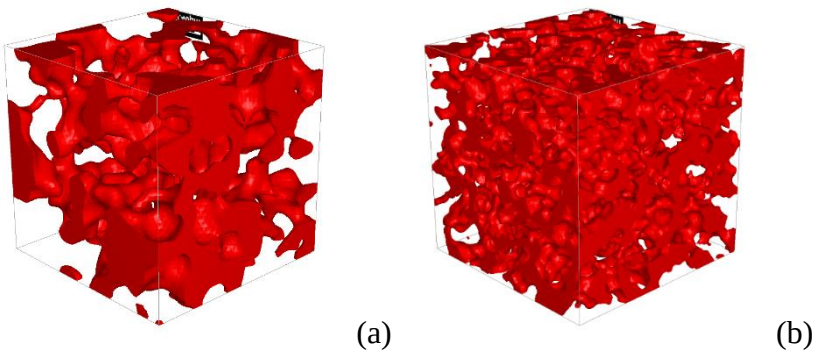

(a) (b)

Figure 5. Microstructure with box size of (a) 50 (b) 100 (c) 150 (d) 200

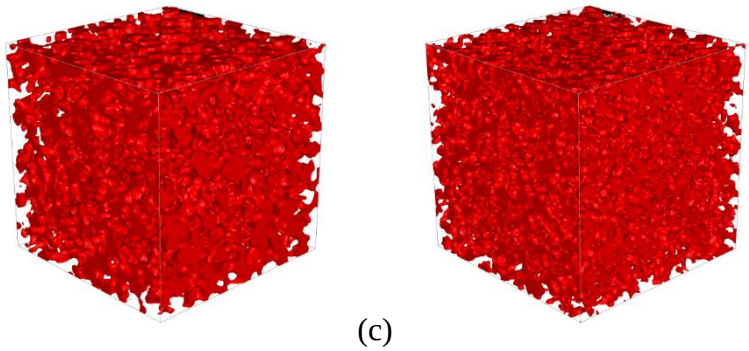

(c) (d)

Figure 5. Continued

As the box size increases, the resolution of the microstructure becomes finer. Comparing 5(a) and (d), Figure 5 (d) is densely packed since it contains more boxes than that of 5(a). Table 10 shows the values for each parameter in box size statistical study.

Box size	a01	a21	a20	τ	σ	ε_0	CM	ε_2
50	0.0001067	0.86	1.85	4.04	0.03	30.23	19.60	50.15
100	0.0001201	0.88	1.93	3.87	0.04	29.84	19.8	50.26
200	8.105E-05	0.91	1.95	3.86	0.05	29.72	19.96	50.31
400	9.174E-05	0.91	1.97	3.56	0.05	29.69	19.99	50.31

Table 10. Box size statistical study

As shown in Table 10, tortuosity decreases as the box size increases. The box size of 100, 150 and 200 have similar values for tortuosity and they are 3.8718783, 3.8693373 and 3.5628, respectively. Similar trends were observed in area 21, area 20 and conductivity. Box size of 100 was chosen because its value is closer to other finer microstructures. Box size of 150 and 200 were not considered because it will significantly increase the overall computational time. Similar to previous study, the overall percentages distribution for conductive material, precipitation addition and final porosity in all different box sizes are close to each other. Again, the consistency of interfacial area program and GeoDict are demonstrated.

2.4.3 Statistical Study: Primary Multiple Run

After determining the appropriate voxel length and box size, a multi-run study was conducted. The purpose of this study is to determine the consistency of GeoDict microstructures in terms of its percentage distribution for porosity or conductive material. Using a voxel length of 1 and a box size of 100, the same microstructure was created seven times to test the accuracy of the GeoDict microstructures. Figure 6 shows the seven microstructures before and after precipitation created with same set of conditions.

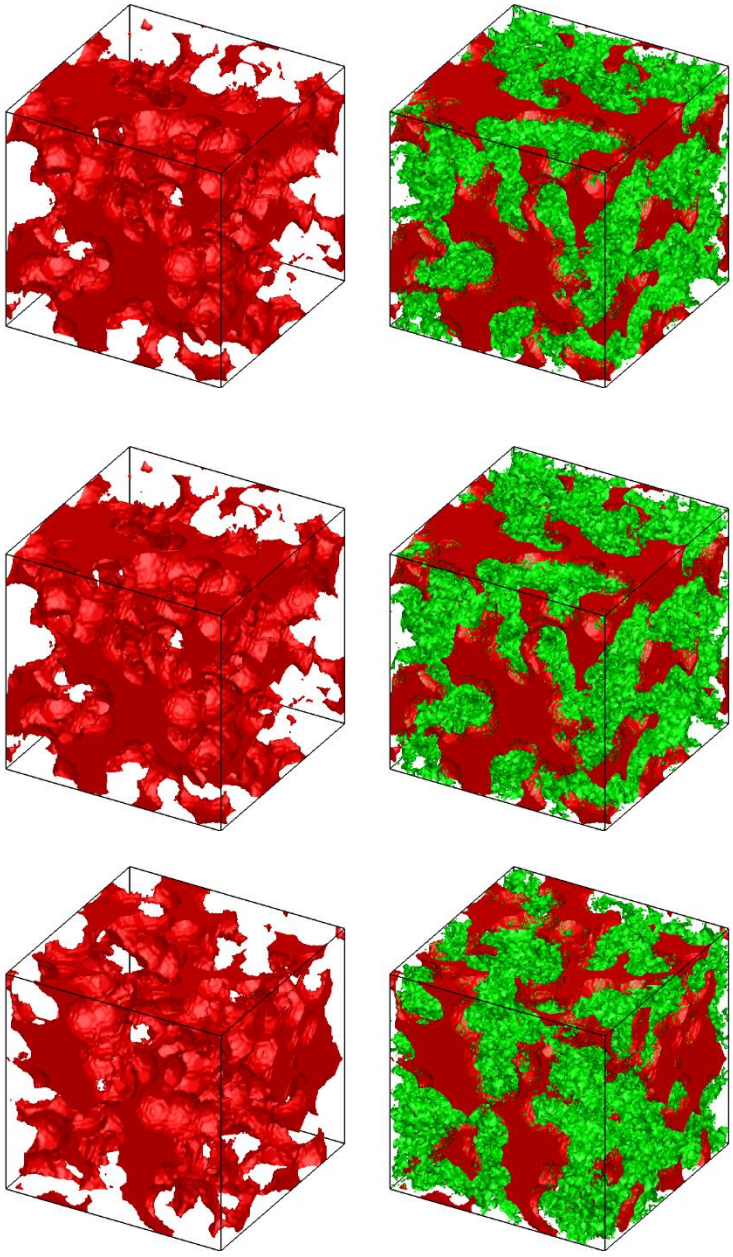

Figure 6. Microstructures created with the same parameters in GeoDict

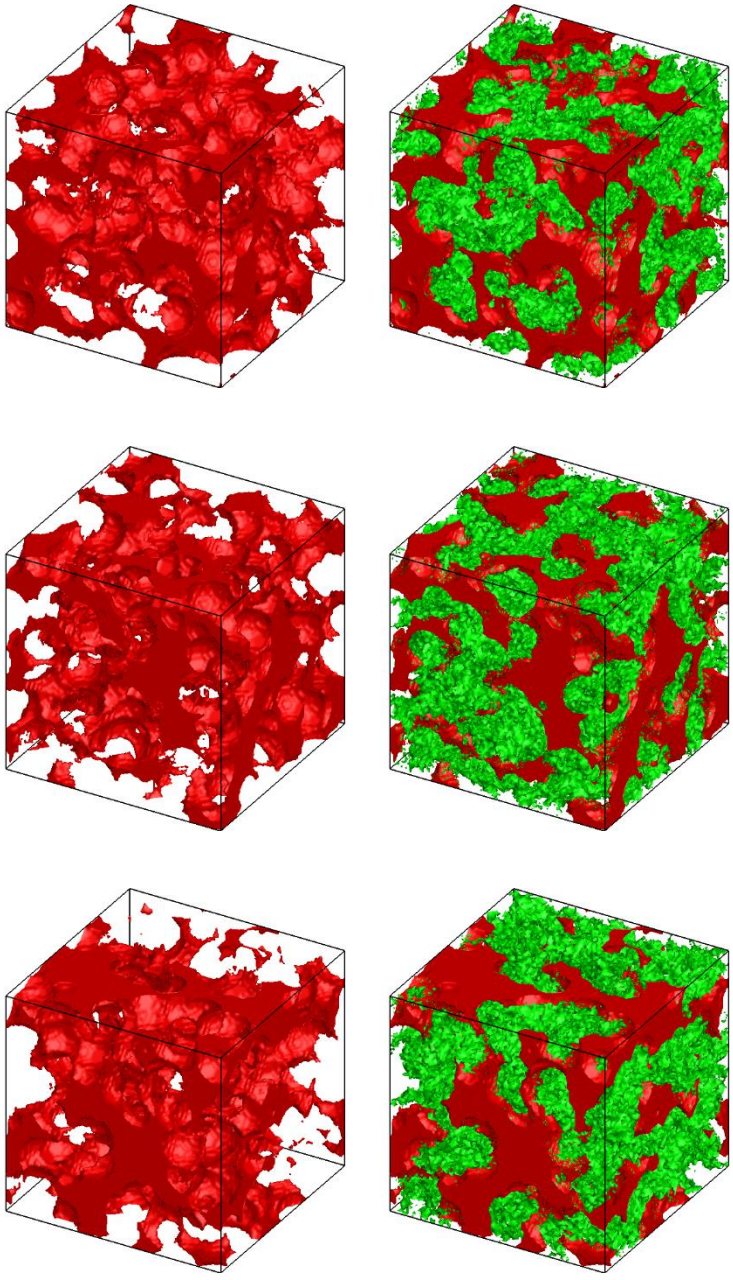

Figure 6. Continued

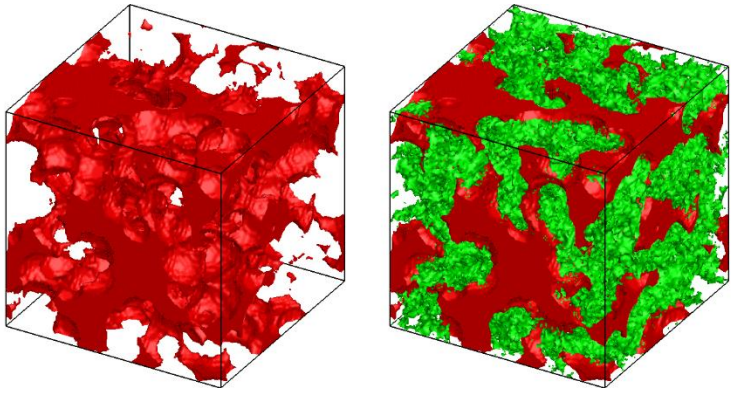

Figure 6. Continued

As shown in Figure 6, the microstructures look different from each other but they were created with the same parameters. Although some microstructures might have the same base structure, they are different from each other after precipitation addition. Table 11 shows the values for each parameter in primary multiple run statistical study.

Runs	a01	a21	a20	τ	σ	ε_0	CM	ε_2
1	8.673E-05	0.88	1.93	3.8499617	0.05	29.8447	19.8831	50.2722
2	5.337E-05	0.88	1.93	3.864965	0.05	29.8442	19.8831	50.2727
3	5.337E-05	0.86	1.90	3.8608413	0.05	29.853	19.946	50.201
4	0.0002002	0.92	2.01	3.9541507	0.05	29.5765	19.9194	50.5041
5	0.0001868	0.95	2.06	4.3358083	0.05	29.4775	19.9707	50.5518
6	0.0001134	0.88	1.92	3.785132	0.05	29.8508	19.8831	50.2661
7	0.0001201	0.88	1.93	3.8718783	0.05	29.8484	19.8831	50.2685

Table 11. Primary multiple run statistical study

The percentages distribution for conductive material, precipitation addition and porosity are similar to each other for all seven runs. The tortuosity ranges from 3.785132 to 4.3358083. Area 21, area 20 and conductivity for all seven runs are close to each other. It can be concluded that the microstructures from GeoDict have consistent values for percentages distribution.

2.4.4 Statistical Study: Simultaneous Deposition Sites

After confirming the consistency of GeoDict, it is necessary to consider the interfacial area program. One microstructure was used for this study while simultaneous deposition site (NSimultaneous) is the changing variable. As mentioned before,

NSimultaneous is an input parameter which dictates the number of deposition sites for the precipitates to settle simultaneously. In every iteration in the program, a designated amount of empty space can be deposited on. Therefore, it is important to see the effect of NSimultaneous on the microstructure evolution. Herein, NSimultaneous is divided by N to either increase or decrease the number of deposition sites. Figure 7 shows examples of microstructures with various N factors.

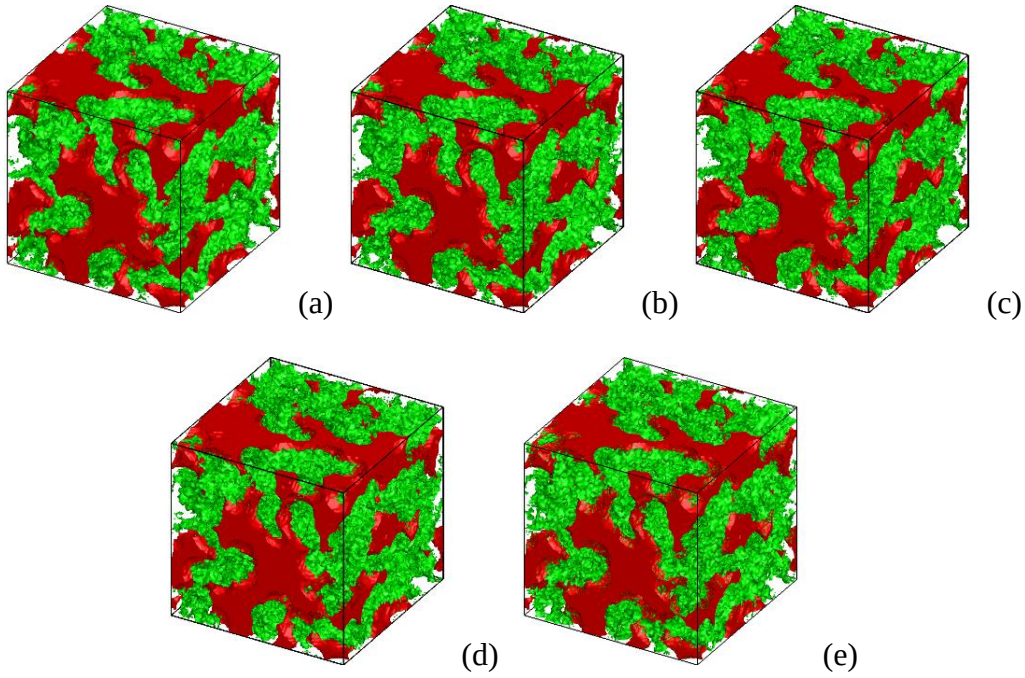

Figure 7. Microstructures with various N factors: (a)25 (b)50 (c)100 (d)200 (e)400 and N = 25 (left) N = 400 (right)

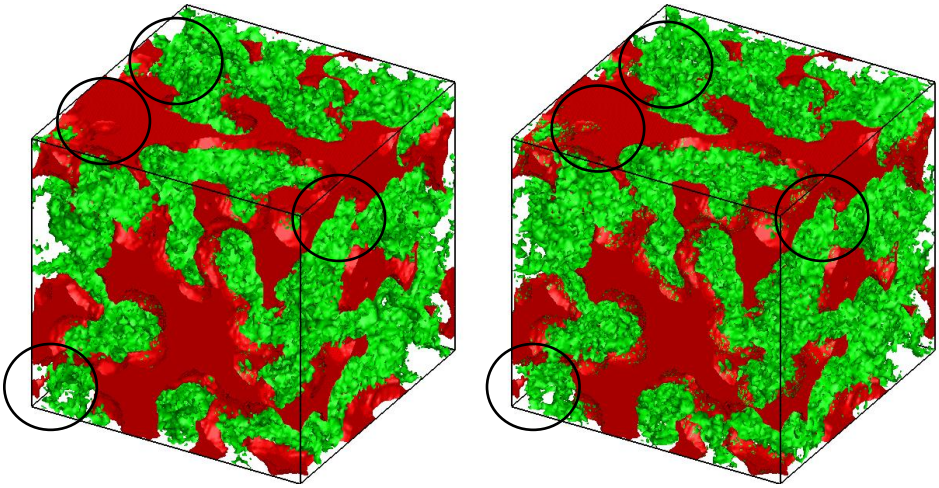

Figure 7. Continued

The red represents the conductive material and the green represents the precipitate. The number of deposition sites is smallest when N equals to 400 while it is the highest when N equals to 25. In both microstructures, some precipitates settle on top of the conductive material. Most precipitates form cluster in the empty space. Both models show pore blockage and surface passivation due to precipitation. Comparing the black circles in Figure 7, more precipitates are visible on top of the conductive material for the right microstructure. The reason is that more precipitates were deposited at once with a higher number of deposition sites. The probability of the precipitates settle in a repeated location is higher. In contrast, low number of deposition sites means less precipitates were deposited at once. The chance of a repeating location is smaller. Table 12 shows the values for each parameter in simultaneous deposition site statistical study.

N	a01	a21	a20	τ	σ	ε_0	CM	ε_2
25	2.002E-05	0.8802378	1.6659042	3.77	0.05	28.8387	19.8831	51.2782
50	3.336E-05	0.8802244	1.8395886	3.80	0.05	29.8439	19.8831	50.273
100	8.673E-05	0.8801711	1.9346204	3.84	0.05	29.8447	19.8831	50.2722
200	0.0001201	0.8801377	1.994152	3.89	0.05	29.9406	19.8831	50.1763
400	0.0001534	0.8801044	2.0079357	3.92	0.05	30.0021	19.8831	50.1148

Table 12. Simultaneous deposition site statistical study

As shown in Table 12, area 21, area20 and tortuosity have relatively close values for all N values. The simultaneous deposition site dictates locations of precipitates settle on. Therefore, area 21 and area 20 are the two most important parameters for comparison. Herein, 100 was chosen as the value for N because its values for area 21 and area 20 are within the range for all N values. The percentage difference is significantly small. In addition, there is a less than 5% difference between the highest and lowest tortuosity values. The percentages distribution for conductive material, precipitation and porosity are similar with each other. It should be noted that the average conductivity remains the same because this study is based on one microstructure.

6.4.5 Statistical Study: Secondary Multiple Run

The purpose of secondary multiple run is to see the accuracy of the interfacial area program. One microstructure was used for this study and the program was used seven times to add 50% precipitation into the microstructures as shown in Figure 8.

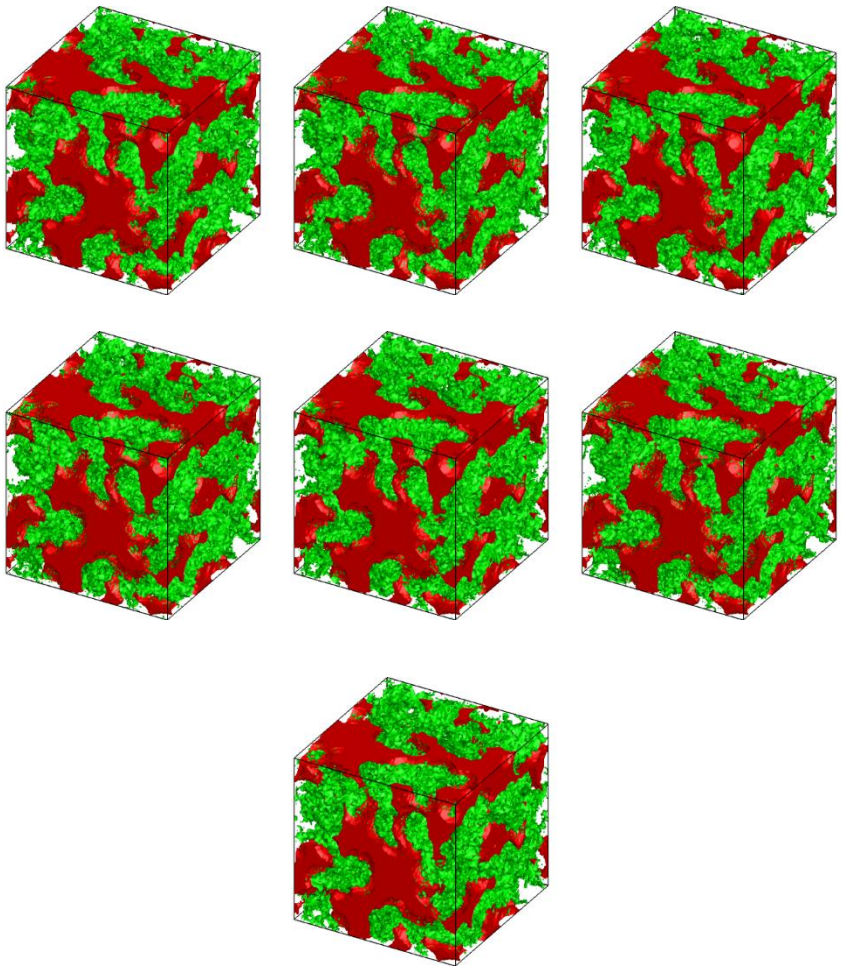

Figure 8. Seven microstructures with 50% precipitation addition

All seven microstructures have random distribution of precipitates while their base structure remains the same. Table 13 shows the values for each parameter in secondary multiple run statistical study.

Runs	a01	a21	a20	τ	σ	ε_0	CM	ε_2
1	8.006E-05	0.8801777	1.92	3.86	0.05	29.8567	19.8831	50.2602
2	7.339E-05	0.8801844	1.92	3.90	0.05	29.8484	19.8831	50.2685
3	8.006E-05	0.8801777	1.92	3.87	0.05	29.8464	19.8831	50.2705
4	9.34E-05	0.8801644	1.92	3.80	0.05	29.8344	19.8831	50.2825
5	8.006E-05	0.8801777	1.92	3.77	0.05	29.831	19.8831	50.2859
6	9.34E-05	0.8801644	1.92	3.80	0.05	29.8485	19.8831	50.2684
7	8.673E-05	0.8801711	1.93	3.96	0.05	29.8518	19.8831	50.2651

Table 13. Secondary multiple run statistical study

As shown in Table 13, the values for precipitation addition are consistent. Similarly, area 01, area 21, area 20 and tortuosity for all seven runs are congruous. Therefore, it can be concluded that the program produces consistent and accurate results.

2.5 Energy Partition Coefficient

After determining confirming the accuracy of the active program and GeoDict, the last parameter within the interfacial area program is the Energy Partition Coefficient. The purpose of this study is to provide multiple correlations between Energy Partition Coefficient, porosity, precipitation addition, active area and tortuosity. Four microstructures were created with different initial porosities in GeoDict. A precipitation addition of 50% was used and four different Energy Partition Coefficients were compared. Microstructures data file were generated and recorded in every 10% interval. Table 14 shows the range of values used for this study and Figure 9 to 12 show the corresponding microstructures for all four Energy Partition Coefficients.

Initial Porosity	60%, 70%, 80%, 90%
Energy Partition Coefficient	0.2, 0.4, 0.6, 0.8
Recorded Precipitation Addition	0%, 10%, 20%, 30%, 40%

Table 14. Ranges of values for Energy Partition Coefficient study

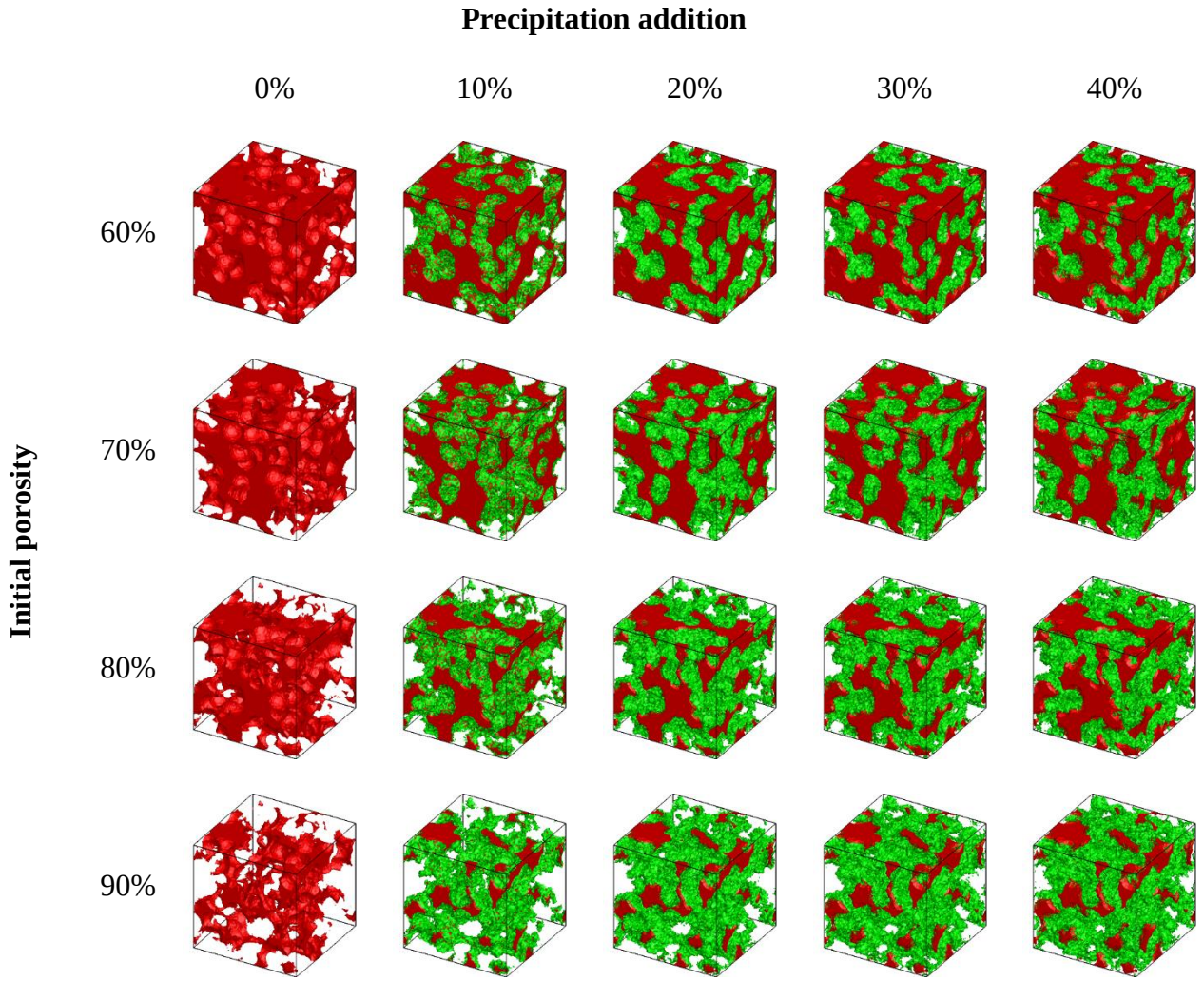

Figure 9. Microstructures for Energy Partition Coefficient of 0.2

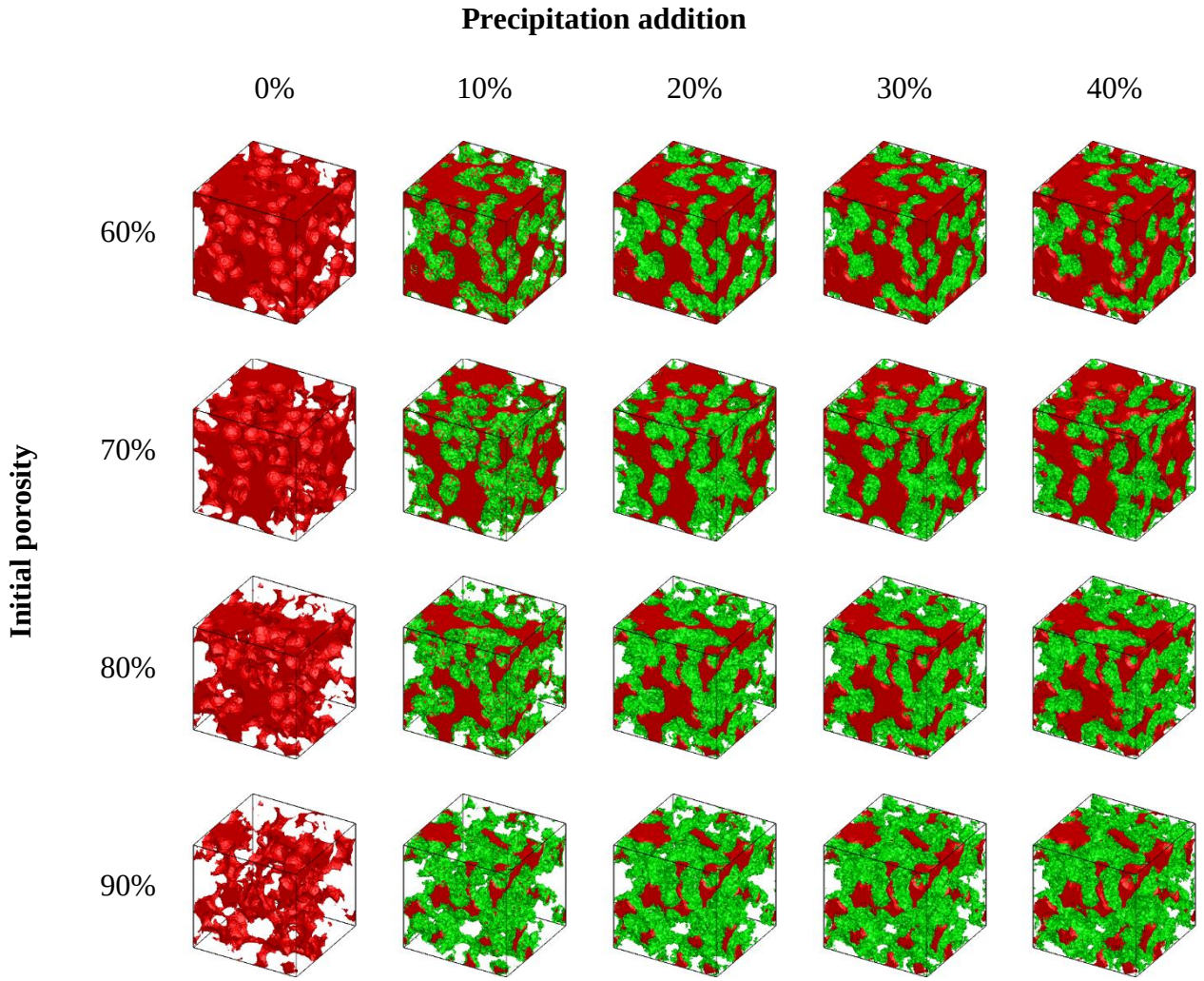

Figure 10. Microstructures for Energy Partition Coefficient of 0.4

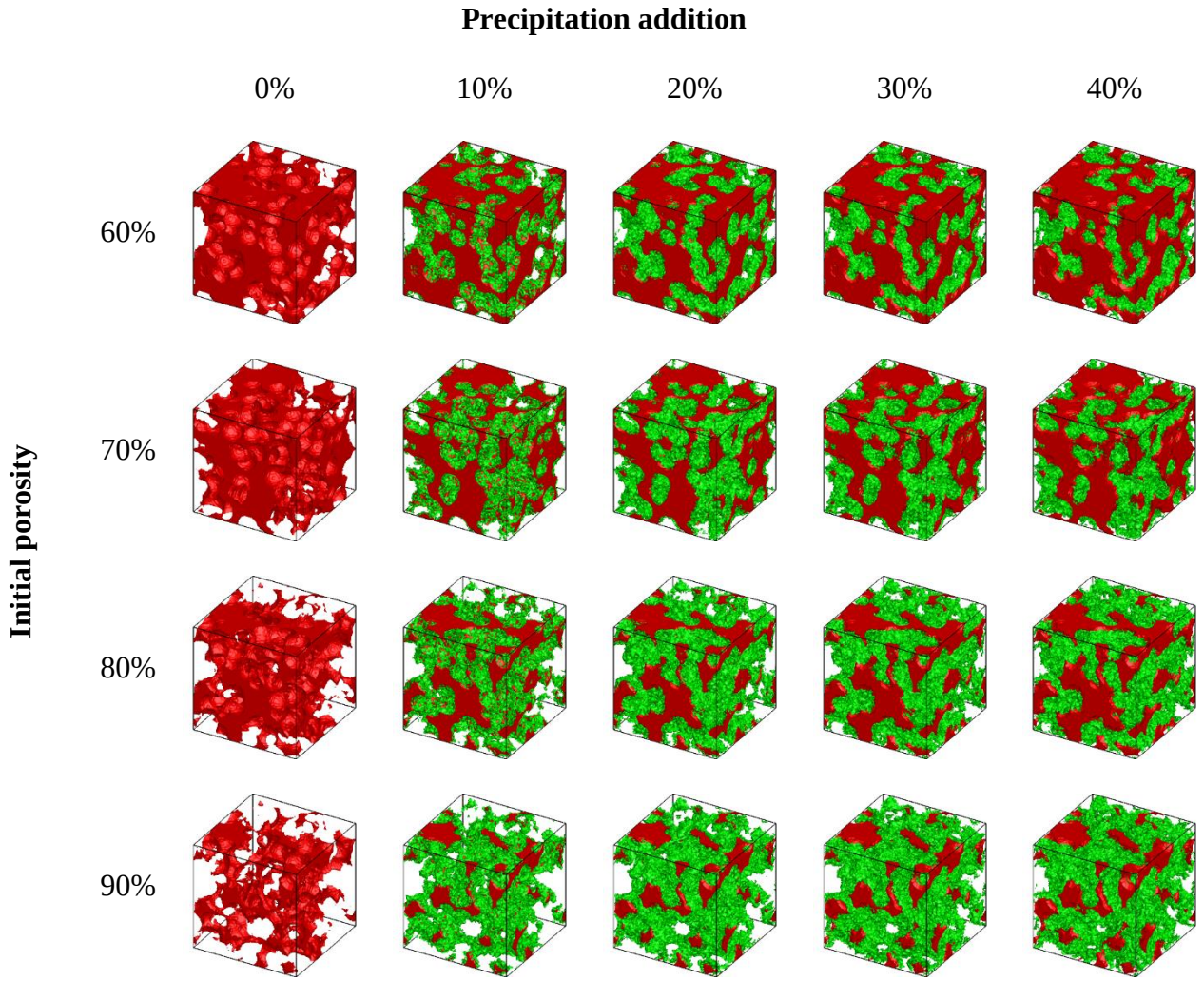

Figure 11. Microstructures for Energy Partition Coefficient of 0.6

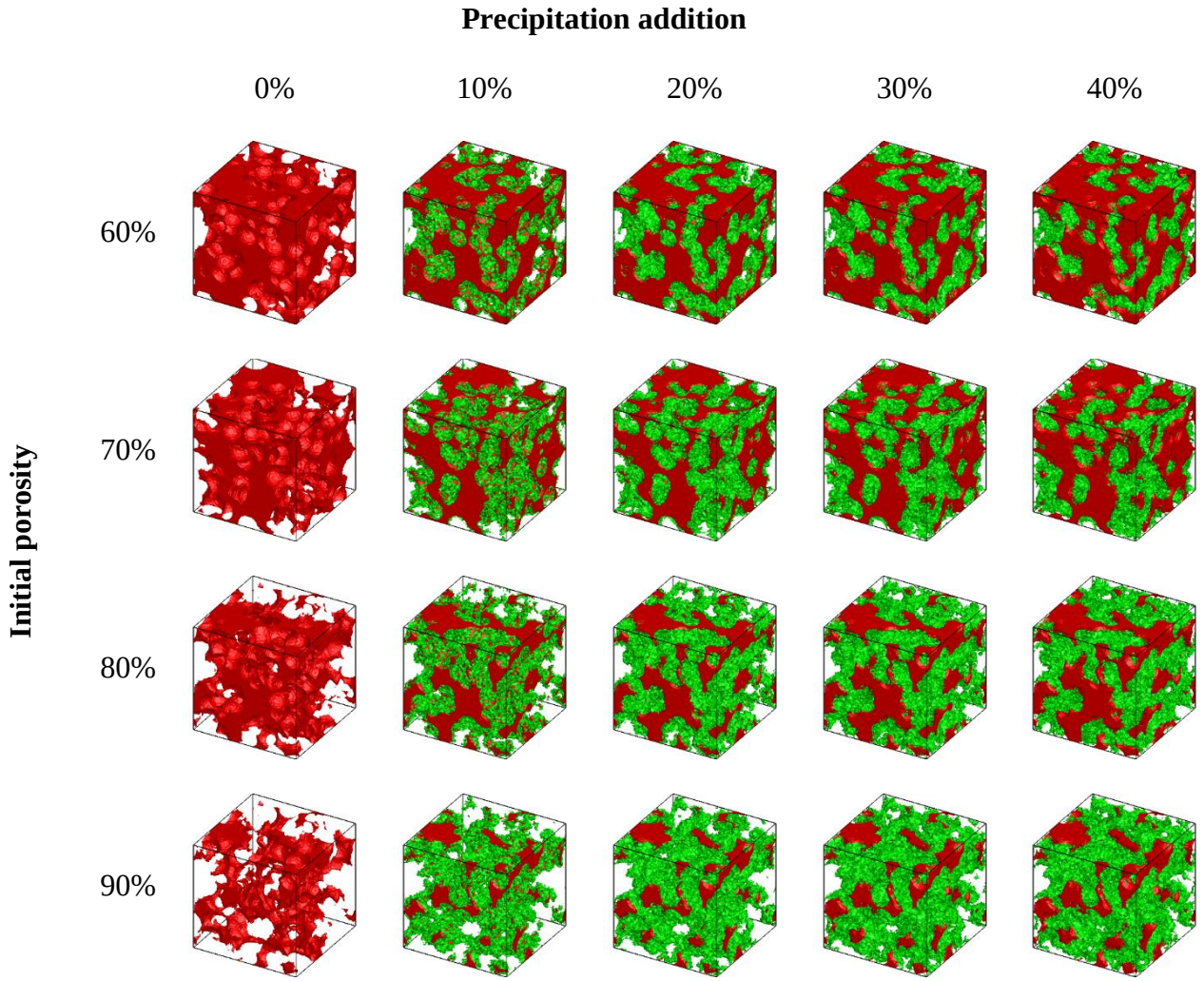

Figure 12. Energy Partition Coefficient of 0.8

As shown in the figures, area 01 decreases rapidly as precipitation addition increases. Area 21 and area 20 are increasing as area 01 becomes less available. Average tortuosity increases as precipitation addition increases. Average conductivity remains the same because precipitates are highly insulating. Therefore, it does not affect the conductivity of the conductive material. In addition, the conductive material has a high conductivity value. Conductivity only increases when the amount of conductive material increases. The total percentages for porosity, conductive material and precipitation addition should always equal to hundred percent.

Although the overall trend is similar, distinct differences are observed in area 01, area 20, area 21 and tortuosity when Energy Partition Coefficient is considered. For example, area 01 for a microstructure with 60% porosity and 20% precipitation addition are 0.0024285 and 0.129844681m^2/m^3 for Energy Partition Coefficient of 0.2 and 0.8, respectively. Area 20 and area 21 have significant differences as well when compared with different Energy Partition Coefficients. Based on the results, it can be concluded all three areas are a combined function of porosity, precipitation addition and Energy Partition Coefficient. Similarly, tortuosity is varying for different Energy Partition Coefficient. However, a smaller fluctuation is observed between all four Energy Partition Coefficients. Interestingly, conductivity does not vary between all four Energy Partition Coefficients which suggested that conductivity is only a function of porosity and precipitation addition.

2.6 Data Trends and Correlation Extraction

It is necessary to fit the data by formulating multiple correlation equations for interfacial area 01, interfacial area 20, interfacial area 21, tortuosity and conductivity. These equations are important toward discharge capacity calculations which will be further discussed in details. Based on the data trends, the correlation equations were found to be the following,

$$\tau = (a_0 + \varepsilon_2(a_1 + a_2\varepsilon_2 + a_3 w)) \cdot (\varepsilon_0 - \varepsilon_2)^{(b_0 + \varepsilon_2(b_1 + b_2\varepsilon_2 + b_3 w)}$$

$$\sigma = a_0(1 - \varepsilon_0)^{a_1}$$

$$a_{01} = (a_0 + a_1(1 - \varepsilon_0) + a_2(1 - \varepsilon_0)^2) \cdot \left(1 - \left(\frac{\varepsilon_2}{a_3 + a_4 w^{a_5}}\right)^{a_6}\right)$$

$$a_{12} = (a_0 + a_1(1 - \varepsilon_0) + a_2(1 - \varepsilon_0)^2) \cdot \varepsilon_2(a_3 + a_4\varepsilon_2 + a_5 w)$$

$$a_{20} = (a_0 + a_1(1 - \varepsilon_0 + \varepsilon_2) + a_2(1 - \varepsilon_0 + \varepsilon_2)^2) \cdot \varepsilon_2(a_3 + a_4\varepsilon_2 + a_5 w)$$

$$a_{1(0+2)} = a_0 + a_1(1 - \varepsilon_0) + a_2(1 - \varepsilon_0)^2$$

where τ is the average tortuosity, σ is the average conductivity, ε_0 is the initial porosity, ε_2 is the precipitation addition, w is the Energy Partition Coefficient, a_{01} is the effective interfacial active area in the microstructure, a_{12} is the dimensionless area between conductive material and precipitates, a_{20} is the dimensionless area between precipitates and pore and $a_{1(0+2)}$ is the summation of a_{01} and a_{12}. All other variables are constants.

In tortuosity, a power fit was chosen to fit the data as tortuosity increases rapidly when precipitation addition increases. As mentioned before, conductivity does not depended on Energy Partition Coefficient. Similar conclusion can also be seen in $a_{1(0+2)}$. The values of conductivity are the same which suggested that it is not depended on Energy Partition Coefficient. A polynomial function was used to characterize its increment for different initial porosities. In addition, the initial percentage of conductive material strongly influences the conductivity value. Power function was also chosen for a_{01}. In the data results, a_{01} for 60% initial porosity at Energy Partition Coefficient of 0.2, the initial area is between 1E-1 to 1. After 50% precipitation addition, the new value is between 1E-5 to 1E-6. A significant decay was observed. For a_{12} and a_{20}, small increase was observed at every 10% interval. Therefore, a polynomial function was used to characterize the behavior.

Using nonlinear curve fitting, the equations were found to be closely fit with the presented data in Figure 13 to 18 and the corresponding R-squared values are shown in Table 15.

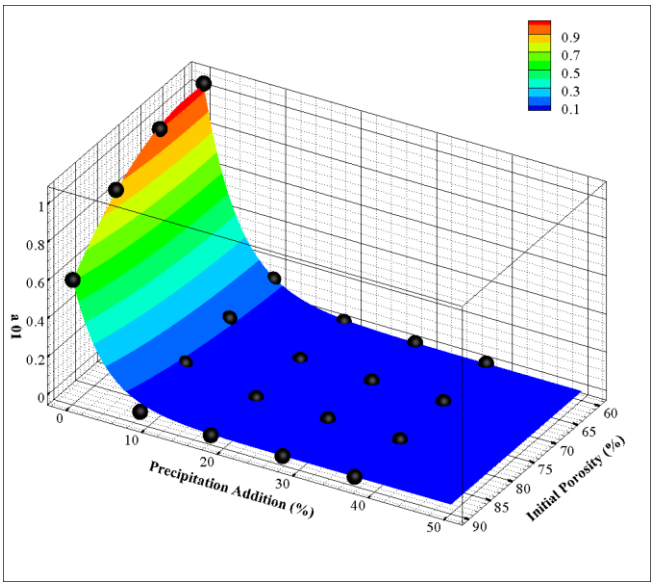

(a)

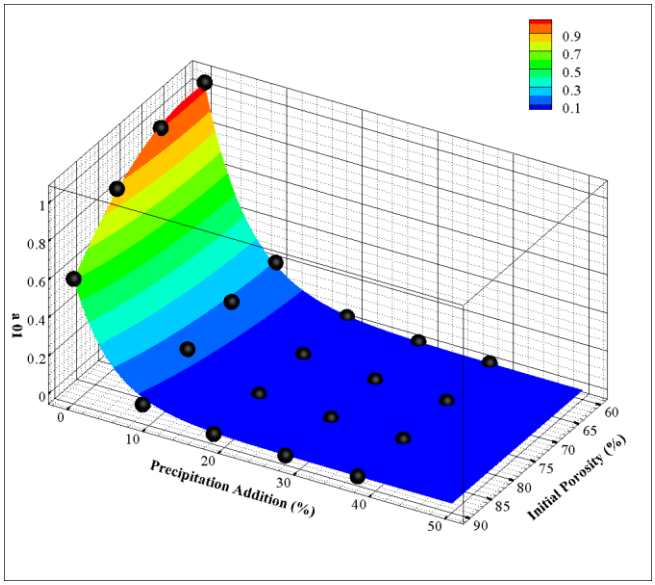

(b)

Figure 13. Curve fits for a01 with Energy Partition Coefficient: (a) 0.2 (b) 0.4 (c) 0.6 (d) 0.8

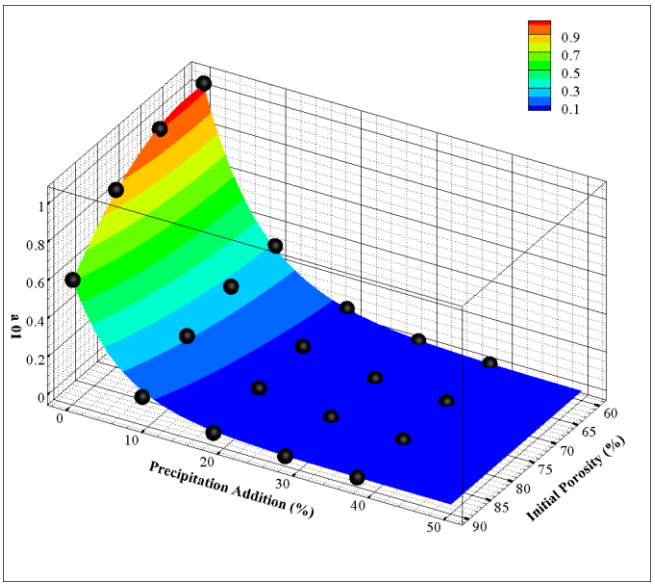

(c)

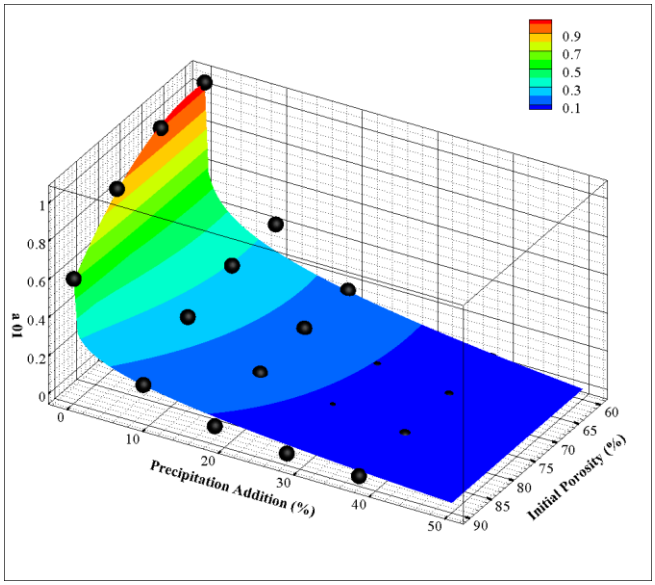

(d)

Figure 13. Continued

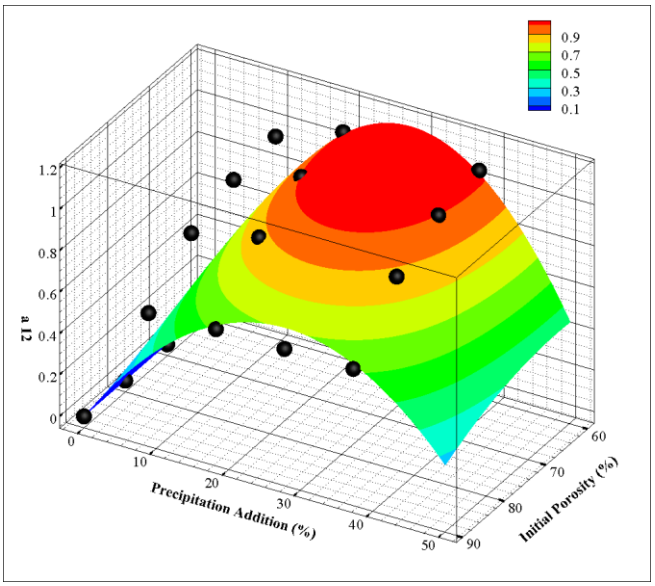

(a)

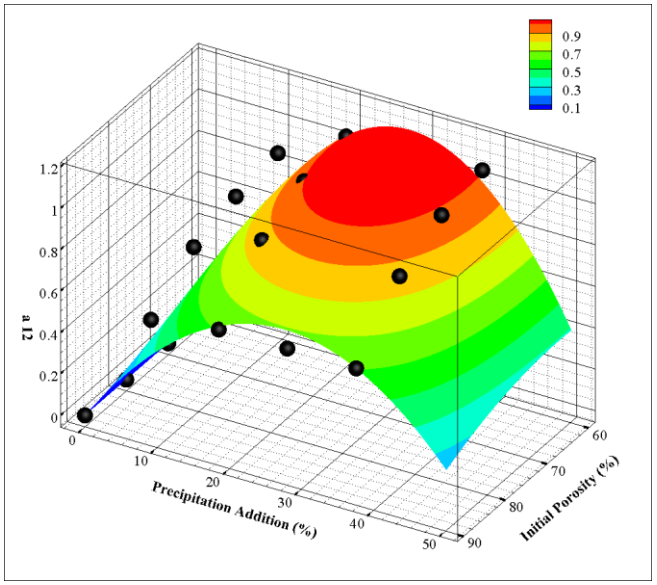

(b)

Figure 14. Curve fits for a12 with Energy Partition Coefficient: (a) 0.2 (b) 0.4 (c) 0.6 (d) 0.8

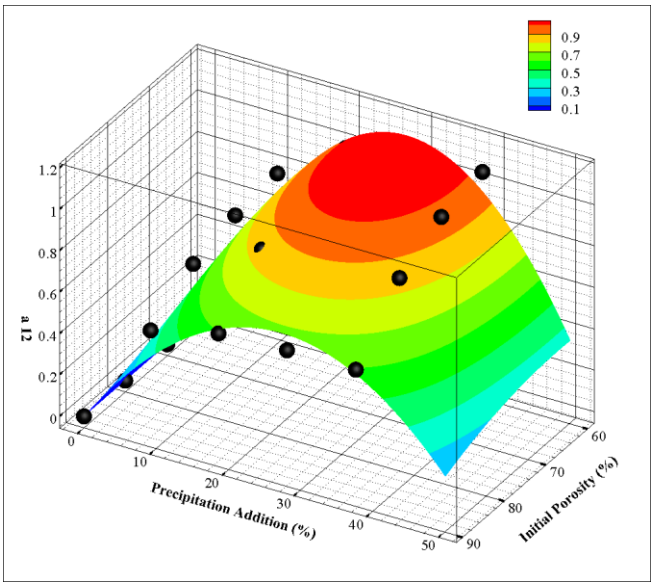

(c)

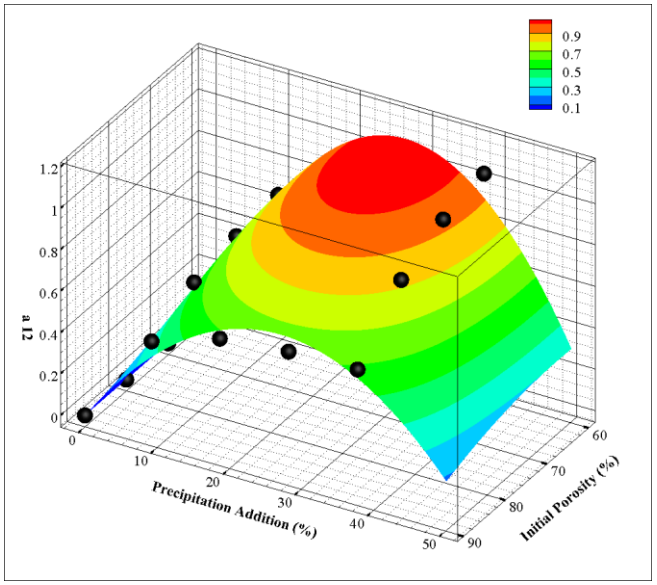

(d)

Figure 14. Continued

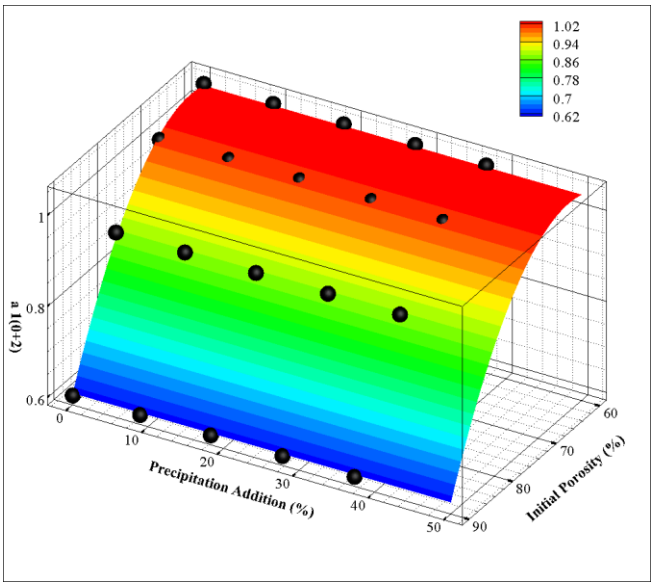

(a)

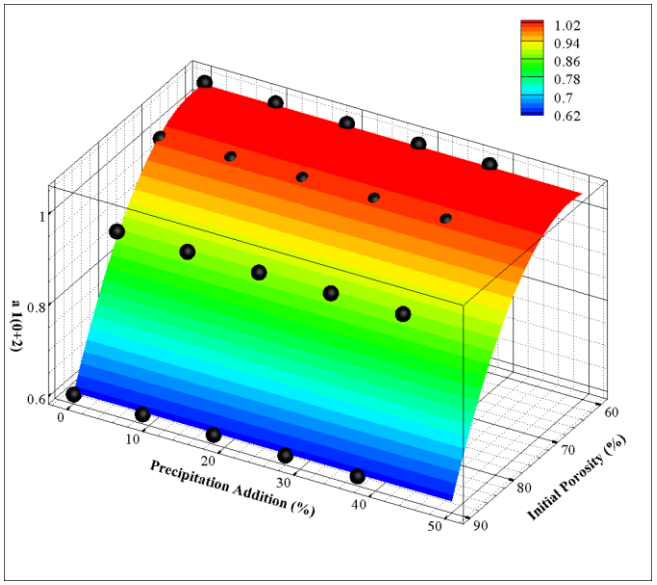

(b)

Figure 15. Curve fits for a1(0+2) with Energy Partition Coefficient: (a) 0.2 (b) 0.4 (c) 0.6

(d) 0.8

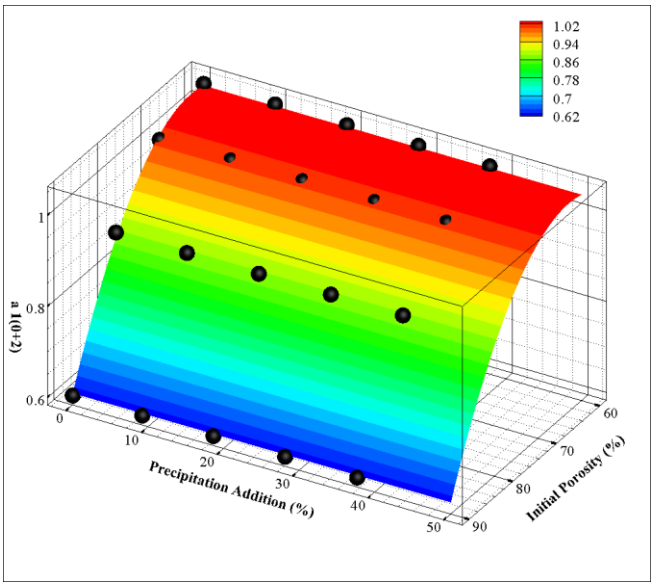

(c)

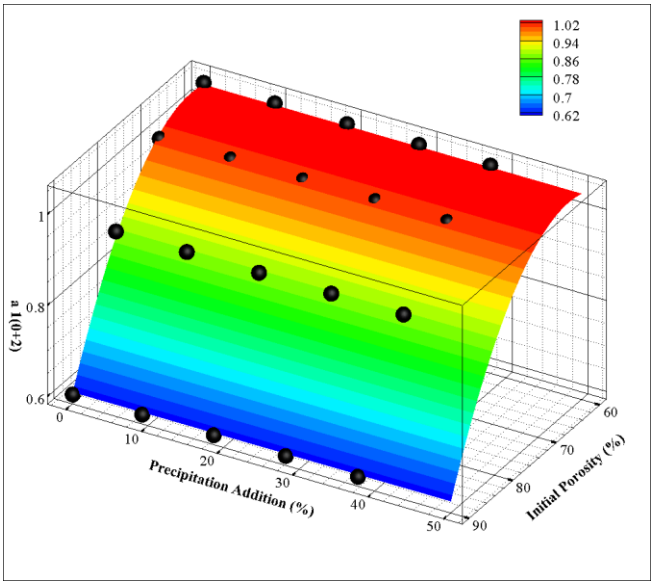

(d)

Figure 15. Continued

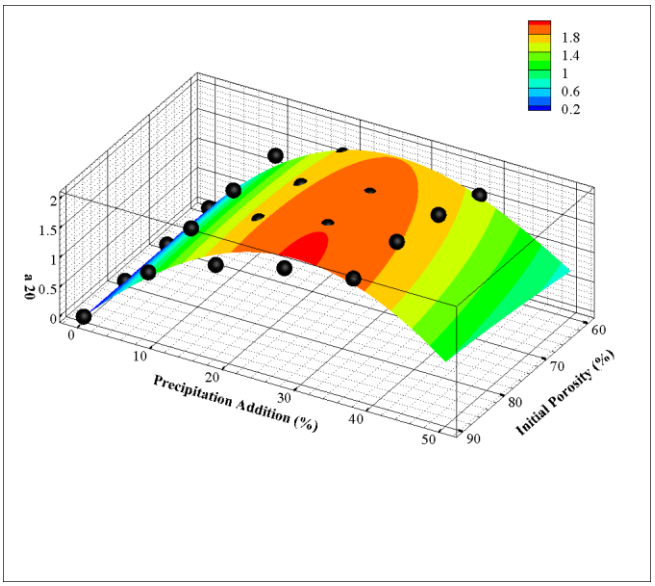

(a)

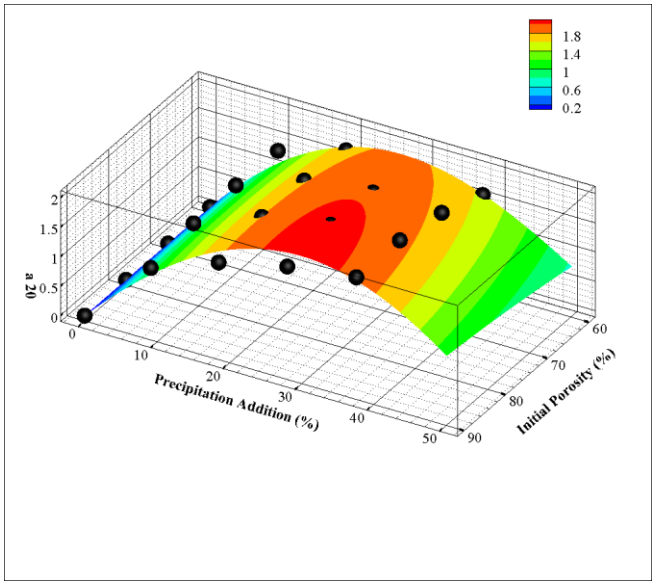

(b)

Figure 16. Curve fits for a20 with Energy Partition Coefficient: (a) 0.2 (b) 0.4 (c) 0.6 (d) 0.8

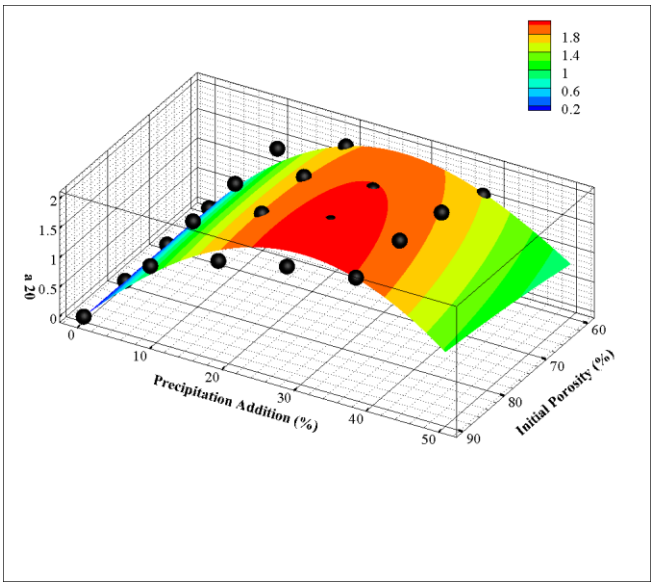

(c)

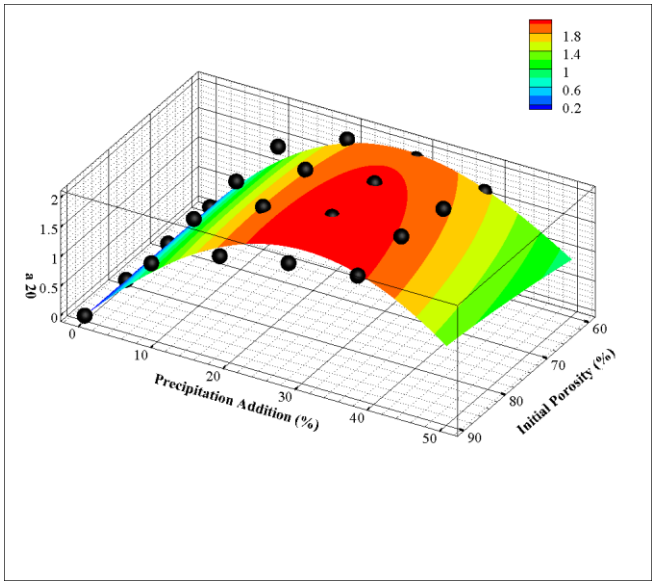

(d)

Figure 16. Continued

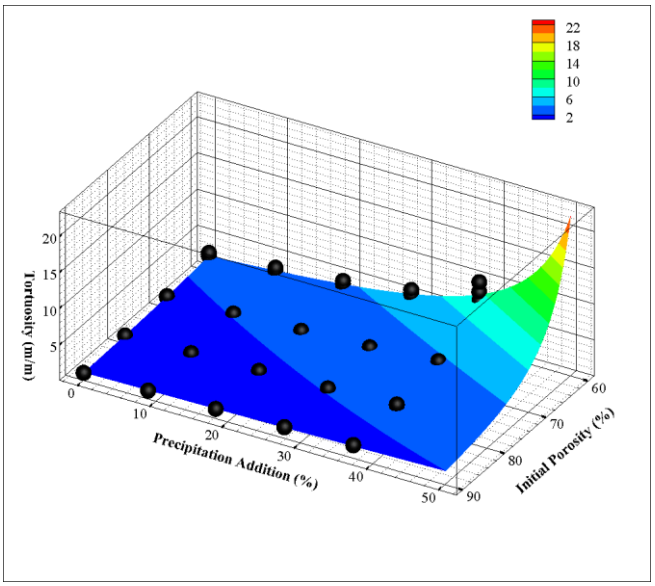

(a)

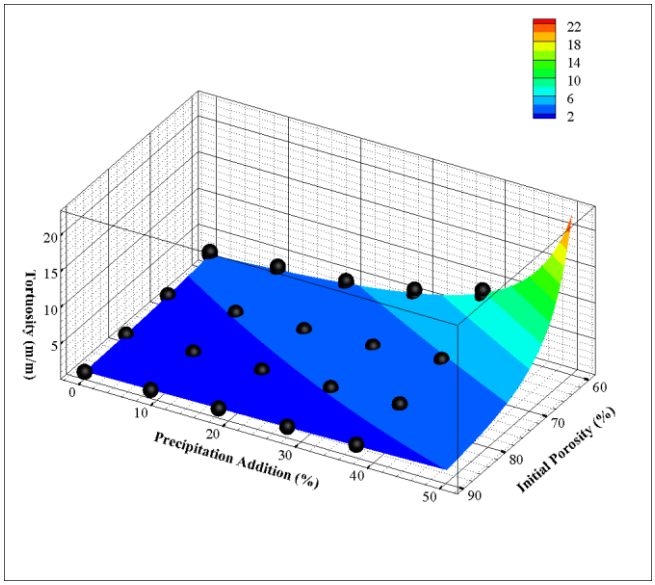

(b)

Figure 17. Curve fits for τ with Energy Partition Coefficient: (a) 0.2 (b) 0.4 (c) 0.6 (d) 0.8

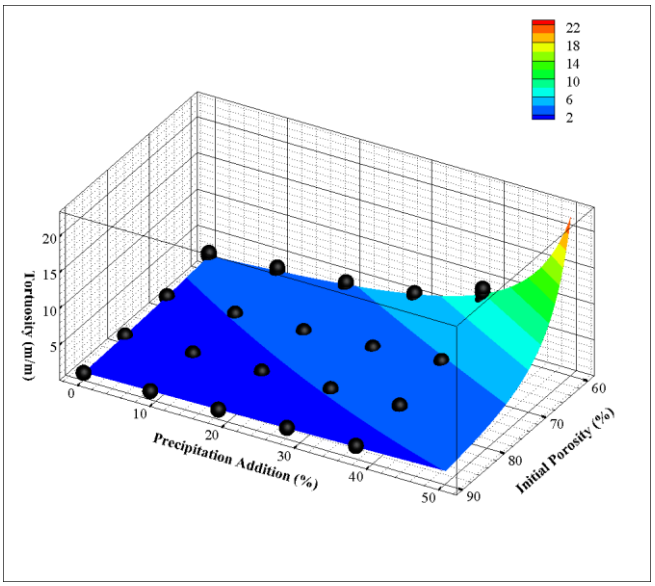

(c)

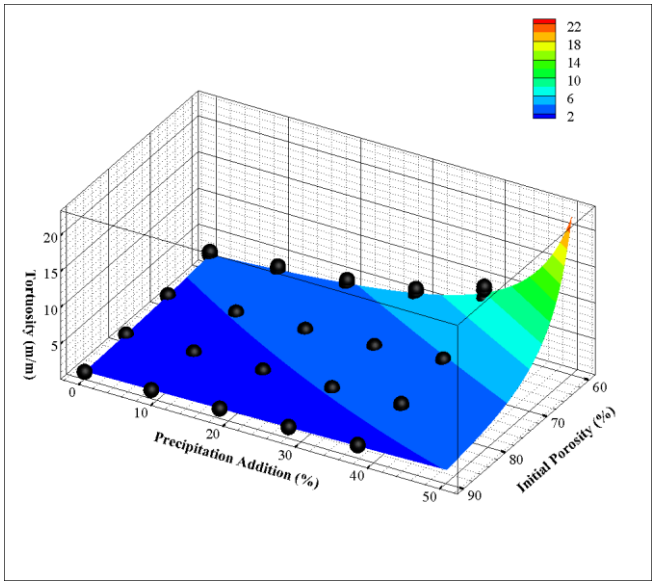

(d)

Figure 17. Continued

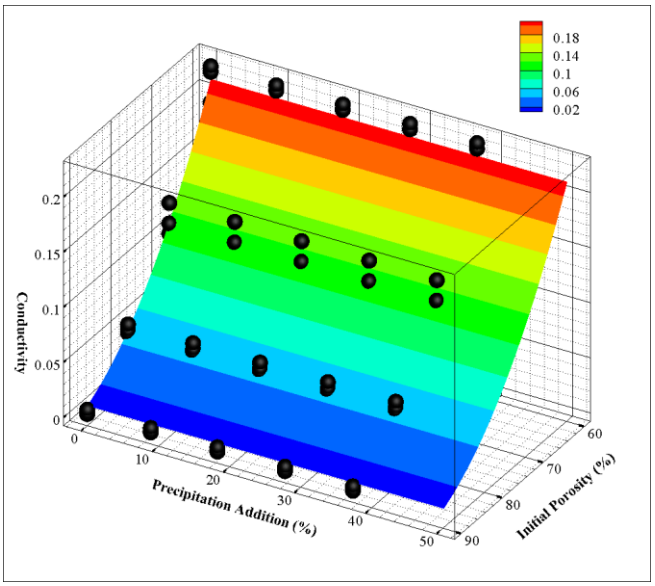

(a)

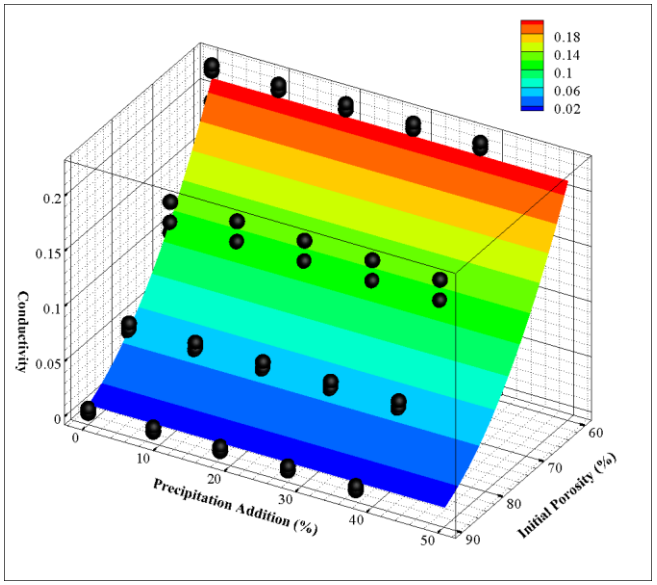

(b)

Figure 18. Curve fits for σ with Energy Partition Coefficient: (a) 0.2 (b) 0.4 (c) 0.6 (d) 0.8

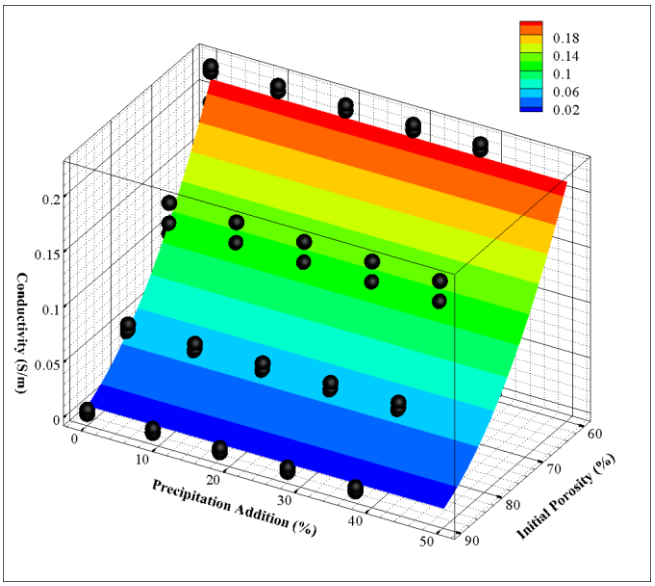

(c)

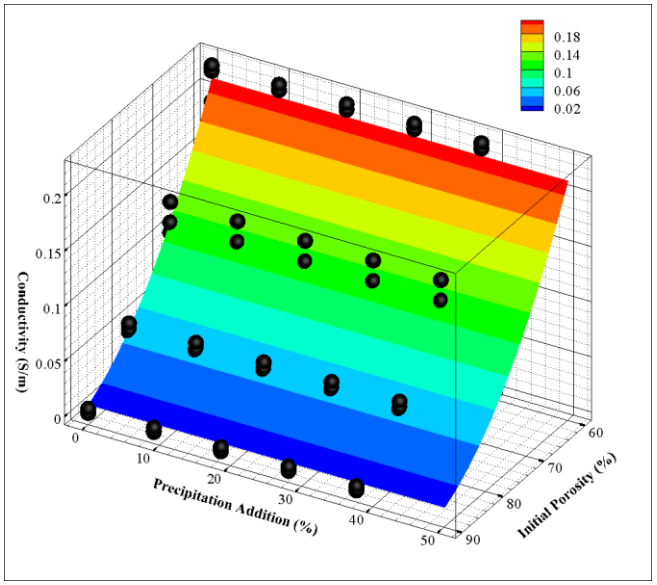

(d)

Figure 18. Continued

Functions	R-squared
τ	0.9686
σ	0.9837
a01	0.9852
a12	0.9303
a20	0.9655
a1(0+2)	0.9973

Table 15. R-squared values for all correlation equations

As shown in Table 15, the correlation equations are closely fit to the data points. The range for the R-squared values are from 0.96 to 0.99. After determining the correlation equations, tortuosity and effective interfacial active area can be implemented into the discharge capacity calculations. The following section will describe the mathematical model used for Li-S cell.

2.7 Discharge Capacity Calculations

In performance comparison, a mathematical model was developed to simulate the discharge process of a Li-S cell. Finite volume method was used as a numerical scheme to implicitly solve multiple coupled governing equations such as species conservation and charge conservation. It is noteworthy to discuss the reaction mechanics of Li-S and

its governing equations before going in depth. Unlike the mechanic of Li-ion cell, Li-S cell discharges based on dissolution of polysulfides. Therefore, there are multiple species to be considered. It is necessary to list out all electrochemical and chemical reactions involved during Li-S cell discharge operation.

$$Li \leftrightarrow Li^{+} + e^{-}$$

$$\frac{1}{2}S_8^{2-} \leftrightarrow \frac{1}{2}S_{8(l)} + e^{-}$$

$$2S_6^{2-} \leftrightarrow \frac{3}{2}S_8^{2-} + e^{-}$$

$$\frac{3}{2}S_4^{2-} \leftrightarrow S_6^{2-} + e^{-}$$

$$S_2^{2-} \leftrightarrow \frac{1}{2}S_4^{2-} + e^{-}$$

$$S^{2-} \leftrightarrow \frac{1}{2}S_2^{2-} + e^{-}$$

$$S_{8(l)} \leftrightarrow S_{8(s)}$$

$$2Li^{+} + S^{2-} \leftrightarrow Li_2S_{(s)}$$

First reaction described as the oxidation of lithium during discharge. The second to sixth Reactions describes the soluble products as high order polysulfides turn into low order polysulfides. Last two reactions describe the precipitation and dissolution process for Li_2S and solid elemental sulfur. It should be noted that the last two reactions are chemical reactions. After accounting all reactions, a model representation is formed.

Figure 19 shows a schematic for this Li-S cell model.

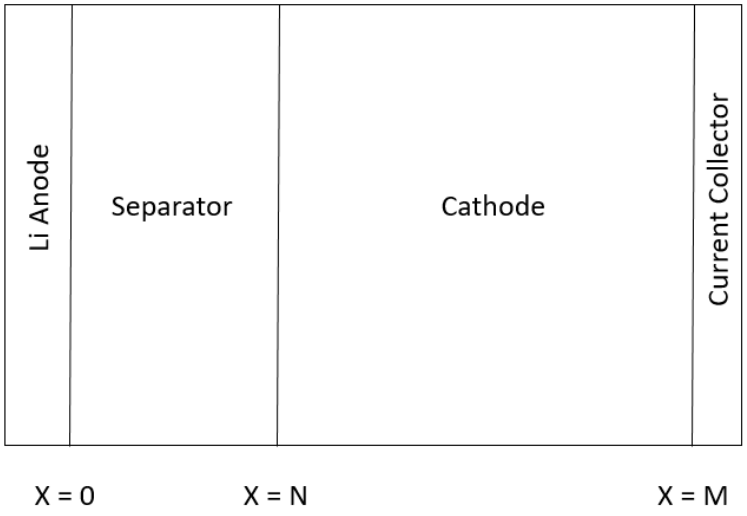

Figure 19. Schematic of Li-S cell for the Mathematical Model

In Figure 19, the left side of the separator was set as the origin. The interface between the separator and the cathode was set as x = N while the interface between the cathode and the current collector was set as x = M.

For this porous model with multiple species, the species conservation was defined as,

$$\frac{\partial(\varepsilon C_i)}{\partial t} = \frac{\partial}{\partial x}\left(D_i \frac{\varepsilon}{\tau}\frac{\partial C_i}{\partial x}\right) + \frac{\partial}{\partial x}\left(z_i F \frac{D_i}{RT}\frac{\varepsilon}{\tau} C_i \frac{\partial \phi_e}{\partial x}\right) + R_i$$

$$i = Li^+, S_{8(l)}, S_8^{2-}, S_6^{2-}, S_4^{2-}, S_2^{2-}, S^{2-}, A^-$$

where ε is the porosity of the cathode, C_i (mol/m^3) is the concentration of species i, D_i (m^2/s) is the diffusion coefficient of species i, τ is the tortuosity of the cathode, z_i is the charge number of species i, F is the Faraday's constant, R (J/mol*K) is the gas constant, T (K) is temperature and ϕ_e is the potential in electrolyte phase. The species conservation only involves migration and diffusion. A total of eight species were considered in this case and they are lithium ions (Li^+), polysulfides ($S_{8(l)}, S_8^{2-}, S_6^{2-}, S_4^{2-}, S_2^{2-}, S^{2-}$) and the anions of the lithium salt in the electrolyte (A^-). Table 16 shows the initial concentration, diffusion coefficient and charge number of all species.

Species	Concentration (mol/ m^3)	Diffusion coefficient (m^2/s)
Li^+	1001.04	1E-10
$S_{8(l)}$	19.0	1E-9
S_8^{2-}	0.178	6E-10
S_6^{2-}	0.324	6E-10
S_4^{2-}	0.020	1E-10
S_2^{2-}	5.229E-7	1E-10
S^{2-}	8.267E-10	1E-10
A^-	1000.0	4E-10

Table 16. Initial concentration, diffusion coefficient and charge number of all species

The eight species indicate there are eight governing equations which means three boundary conditions and one initial boundary for the species concentration are required. Table 16 shows the initial concentration for each species at beginning of time. The species flux is zero at the interface between the current collector and the cathode since the current collector is a physical obstacle in the Li-S cell. Therefore, no species can pass through it. Next, the species flux is continuous at the interface between the separator and the cathode. The number of species going through the separator is equal to the number of

species entering the cathode. Lastly, all species flux is zero at the interface between the anode and the separator except lithium because lithium is the only reacting species at the anode. The porosity of the cathode also changes over time due to precipitation/dissolution reactions. Accounting for the production and consumption rate of species due to precipitation/dissolution reactions, the equation is defined as,

$$\frac{d\varepsilon_i}{dt} = R_i$$

$$i = S_{8(s)}, Li_2S_{(s)}$$

where ε_i is the solid fraction volume of the precipitate i and R_i (mol s^{-1} m^{-3}) is the reaction rate of production and consumption of the species. Porosity of the cathode increases as elemental sulfur turns from solid to liquid phase and decreases as more precipitates form. Throughout the cell model, precipitation/dissolution reactions will happen everywhere. However, only chemical reactions take place in separator since the separator is considered as electronically insulating. The reaction rate and solubility product assigned to $S_{8(s)}$ and $Li_2S_{(s)}$ are vital because they influence the production rate of these insoluble products. The following expression for R_i is defined as,

$$R_i = V_i k_i \varepsilon_i \left(C_i^{n_i} - k_{sp,i}\right)$$

where V_i (m^3/mol) is the partial molar volume of species $S_{8(s)}$ and $Li_2S_{(s)}$, n is the number of moles, C_i are all ionic species involved in the precipitation process, n_i is the number of moles of the involved species, k_i is the reaction rate for solid sulfur dissolution and Li_2S precipitation and $k_{sp,i}$ is solubility product of species k in electrolyte. Herein, the values of the reaction rate and solubility product for $S_{8(s)}$ and $Li_2S_{(s)}$ are 1.0 s^{-1}, 19.0 mol m^{-3} and 27.5 m^6 mol^{-2} s^{-1}, 3.0 mol^3 m^{-9}, respectively. At the beginning of discharge, initial porosity will be the porosity of the cathode while solid volume fractions of the precipitates are zero. As discharge continues, sulfides began to accumulate and the precipitation process began by reacting with lithium ions. In this process, porosity goes hand in hand with the performance of the Li-S cell based on the previous correlation. Specific surface area is significantly reduced as initial porosity decreases rapidly over time. Aside from species conservation, charge conservation is important as well and it is defined as,

$$\sum_i \left(\frac{\partial}{\partial x} \left(z_i^2 F^2 \frac{D_i}{RT} \frac{\varepsilon}{\tau} C_i \frac{\partial \phi_e}{\partial x} \right) + \frac{\partial}{\partial x} \left(z_i F D_i \frac{\varepsilon}{\tau} \frac{\partial C_i}{\partial x} \right) \right) + \sum_k a j_k = 0$$

$$\frac{\partial}{\partial x} \left(\sigma \frac{\partial \phi_c}{\partial x} \right) = \sum_k a j_k$$

$$k = 2,3,4,5,6$$

where a (m^2/m^3) is the specific surface area, j_k (A/m^2) is the current density and ϕ_c is the potential in solid phase. It should be noted that charge conservation includes electrochemical reactions. Therefore, reactions (2) to (6) are included in this case. Equivalent amount of charge will enter and leave a phase based on these equations. There are three boundary conditions for ϕ_c and ϕ_e at each interface. At the anode/separator interface, the solid potential is zero and there is a current density at the electrolyte phase for lithium ion. At the separator/cathode interface, the solid potential flux is zero and the current density at the electrolyte phase is continuous. At the cathode/current collector interface, there is a potential flux due to applied current and the current density at the electrolyte phase is zero. The current density can be obtained by using the Butler-Volmer (B-V) equation. The B-V equation describes the fundamental relationship between current and electrode potential and it is defined as,

$$j_k = j_{k,ref}\left\{\left(\frac{C_i}{C_{i,ref}}\right)^p \exp(\frac{\alpha_a F}{RT}\eta) - \left(\frac{C_i}{C_{i,ref}}\right)^q \exp(-\frac{\alpha_c F}{RT}\eta)\right\}$$

$$k = 2,3,4,5,6$$

where $j_{i,ref}$ (A/m^2) is the exchange current density of the electrochemical reaction at reference concentration, $C_{i,ref}$ is the reference concentration, p is the number of moles for anodic species, q is the number of moles for cathodic species, α_a and α_c are the charge transfer coefficients, η is the overpotential. k represents the electrochemical

reactions (2) to (6). Table 17 shows the values for $j_{k,ref}$, α_a and α_c.

$j_{k,ref}$	α_a	α_c
(k = 2) 1.972	0.5	0.5
(k = 3) 1.972e-2	0.5	0.5
(k = 4) 1.972e-2	0.5	0.5
(k = 5) 1.972e-4	0.5	0.5
(k = 6) 1.972e-7	0.5	0.5

Table 17. Exchange current density at reference concentration and charge transfer coefficients

Although most parameters are known in the B-V equation, the overpotential must be calculated as well and it is defined as,

$$\eta = \phi_c - \phi_e - U_k$$

where U_k is the open circuit potential (OCP) of the electrochemical reaction k. Based on both equations, B-V equation is coupled with the species and charge conversation. The open circuit potential of the electrochemical reaction can be calculated by the Nernst equation. The Nernst equation determines the potential change due to concentration and it is defined as,

$$U_k = U_{k,ref} + \frac{RT}{n_k F} \ln\left(\frac{C_{i,ref}}{1000}\right)$$

where $U_{k,ref}$ is the OCP of the electrochemical reaction k at reference concentration and n_k is the number of exchange electrons. Table 18 shows the values for OCP of the electrochemical reaction k at reference concentration.

Reactions	$U_{k,ref}$
(k = 2)	2.39
(k = 3)	2.37
(k = 4)	2.24
(k = 5)	2.04
(k = 6)	2.01

Table 18. OCP of the electrochemical reaction k at reference concentration

Each reaction happens at a specific OCP. Based on literature review, low order polysulfides are formed at a lower potential while higher order polysulfides are associated with higher potential. After solving for potential at both solid phase and electrolyte phase, the cell voltage can be calculated. As the cell discharges, each time step is recorded. Using equation 19, the discharge capacity of the Li-S cell at each time step can be calculated.

$$discharge\ capacity_t = cap_{theoretical} * \frac{t}{3600} * C$$

where $cap_{theoretical}$ (mAh/g) is the theoretical capacity of sulfur, t (s) is time, and C is the C-rate or discharge rate. Plotting the discharge capacity against voltage at each time step, the performance can be seen and compared.

3. RESULTS AND DISCUSSION

3.1 Trends Found in Literature

Before discussing about the discharge performance, it is necessary to see if the mathematical model can display similar trends found in experiments. Typically, it is common for a cell to have a higher discharge capacity when a low C-rate is applied. This is because higher C-rate passivates the active area on the cathode as opposed to a lower C-rate. Figure 20 shows a comparison between experimental trend and the model with the effect of C-rate.

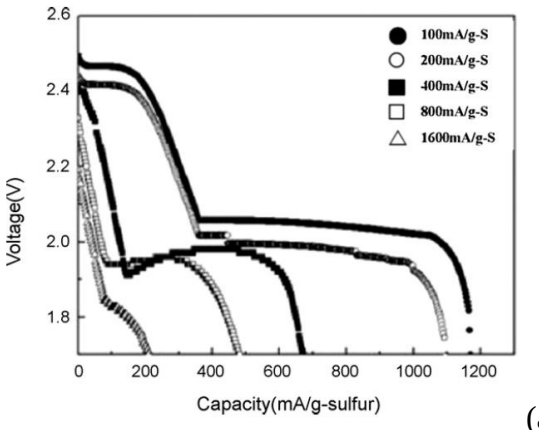

(a)

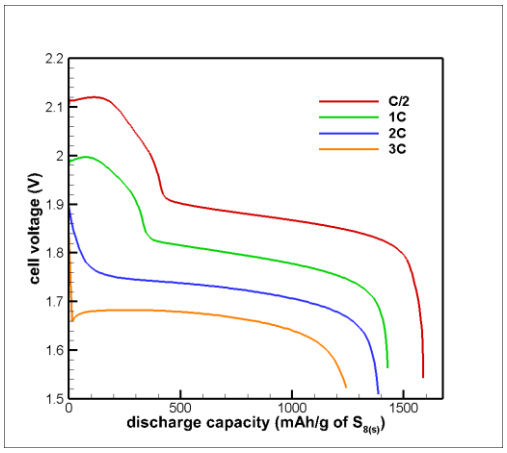

(b)

Figure 20. Effect of C-rate for Li-S cell (a) Experimental result from literature [66] (b) Model result

As shown in Figure 20(a) and (b), the increase of C-rate demonstrates a decrease of discharge capacity. Typically, two plateau regions can be seen in at a lower C-rate. As mentioned before, the first plateau is associated with high order lithium polysulfides. As the discharge operation continues, high order lithium converts to lower order lithium polysulfides which is associated to the second plateau. In Figure 20(a), C/2 shows a small increment in voltage then it drops rapidly to the second plateau. This is because solid elemental sulfur is being converted to liquid S_8 which open more active area. Therefore, a slight increase in voltage was expected. However, the voltage drops rapidly when the cathode becomes saturated with lower order polysulfide species. For 2C and 3C, the upper plateau is not visible at all. This is because reaction occurs faster at high C-rate which causes only partial amount of S_8 being converted to Li_2S_n ($4 < n < 8$). Therefore, a high amount of elemental sulfur remains unutilized in the cathode. Another trend which was found in literature is the effect of sulfur loading. Typically, sulfur loading is found to be less than 60% in most literatures. Although higher sulfur loading provides a better energy density, it does not necessarily mean a better performance or discharge capacity. In fact, high sulfur loading can be detrimental if insulating sulfur covered all available active area. Not only electrochemical reactions won't be able to take place but the discharge capacity becomes significantly worse. Figure 21 shows a comparison between experimental trend and the model with the effect of sulfur loading.

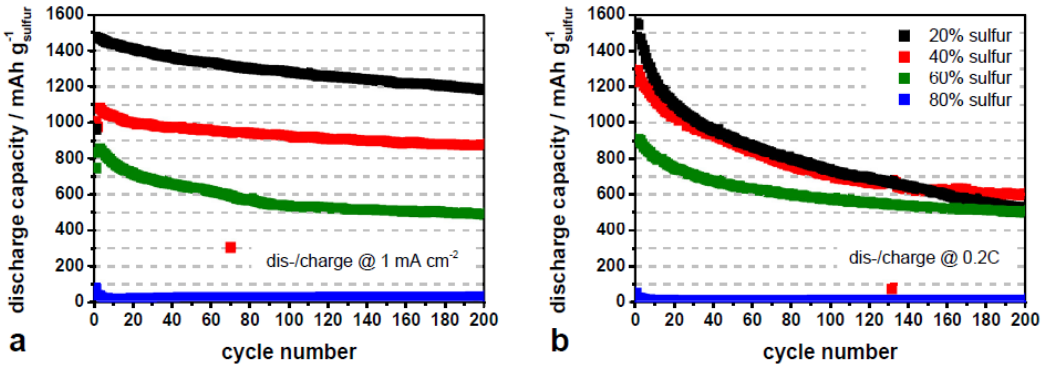

(a)

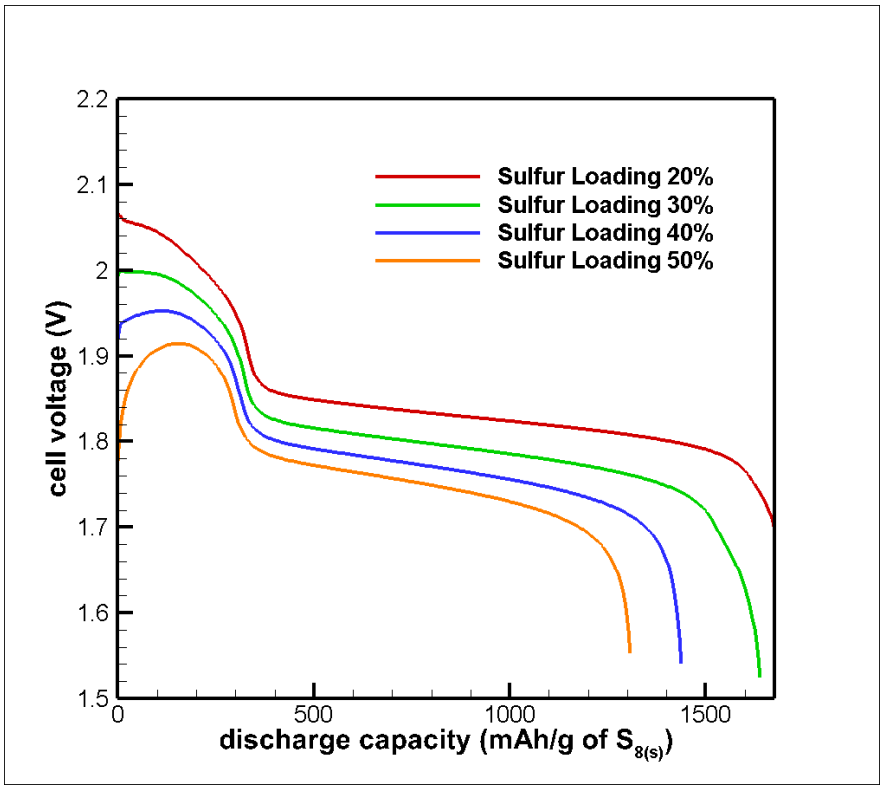

(b)

Figure 21. Effect of sulfur loading for Li-S cell (a) Experimental result from literature [40] (b) Model result

As shown in Figure 21(a) and (b), 20% sulfur loading has a better initial discharge capacity compared to that of 50% sulfur loading. Interestingly, 80% sulfur loading has almost no sulfur utilization during discharge. In Figure 21(a), 50% sulfur loading shows a high increment in voltage which was explained previously. Another trend which was found in literature is the effect of cathode thickness. Typically, the increasing cathode thickness can increase the energy density of the Li-S cell. However, transport limitation could come into play when the thickness increases. When lithium ions diffuse from anode to cathode, they are more likely to react with sulfur closer to the interface between the cathode and separator. If the cathode thickness becomes too thick, it might be harder for lithium to react with the sulfur closer to the current collector side. Therefore, sulfur is not being well utilized in this situation. Figure 22 shows a comparison between experimental trend and the model with the effect of cathode thickness.

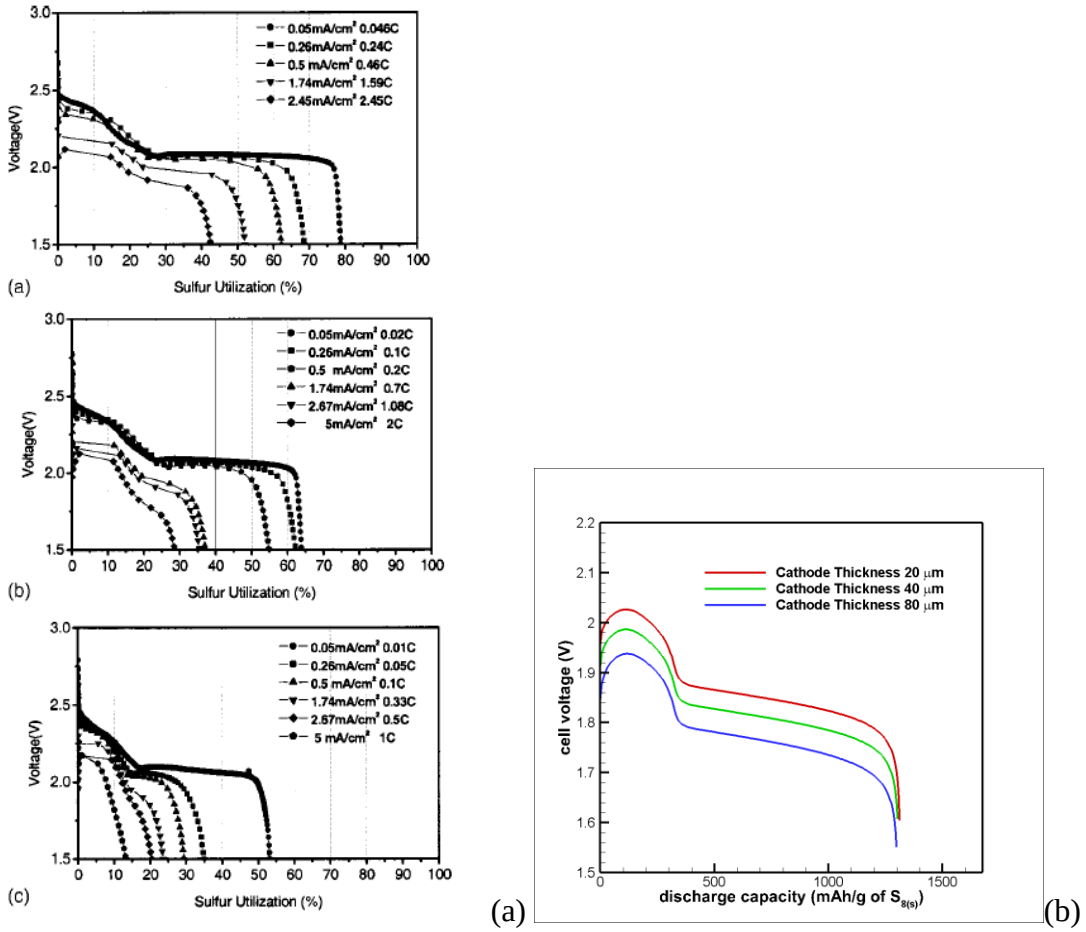

Figure 22. Effect of cathode thickness for Li-S cell (a) Experimental result from literature: Increasing cathode thickness from top to bottom (15 μm, 30 μm, 60 μm) [66] (b) Model result

In Figure 22(a) and (b), the discharge capacity decreases as the cathode thickness increases.

3.2 Energy Partition Coefficient and Sulfur Loading Limitations

Implementing formulated correlations into the mathematical model, there are six parameters which can be changed to investigate microstructural effect on Li-S cell performance. The Six parameters include C-rate, sulfur loading, cathode thickness, initial porosity, mean pore size and Energy Partition Coefficient. However, it is important to identify special cases in which surface passivation happens before the cell discharges. In this mathematical model, surface passivation occurs when active area is no longer available. Recalling the a01 correlations, three parameters govern the active area of the cathode and they are initial porosity, precipitation addition and Energy Partition Coefficient. By plotting all three parameters, an “effective zone” can be observed in Figure 23 to see the maximum limits on precipitation addition with different Energy Partition Coefficient.

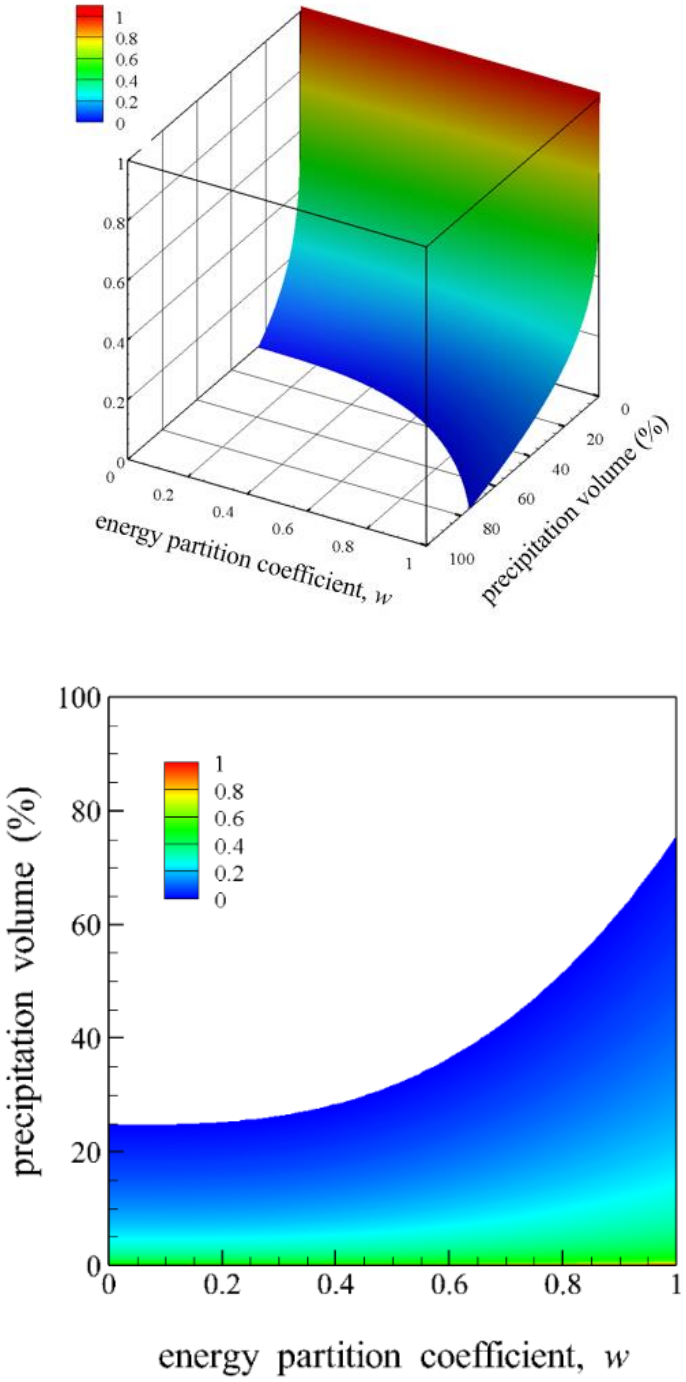

Figure 23. Energy Partition Coefficient and precipitation deposition zone for a01

In Figure 23(a), the active area decreases as precipitation deposition increases. Active area ends earlier with an Energy Partition Coefficient of 0.2 while the opposite trend was observed for higher Energy Partition Coefficient. As previously mentioned, Energy Partition Coefficient provides a location preference for Li_2S to settle. High Energy Partition Coefficient signifies conductive surfaces are less likely to be covered by Li_2S. Thus, more active area is available. In Figure 23(b), the maximum precipitation deposition zone at different Energy Partition Coefficient can be observed easily. For example, an Energy Partition Coefficient of 0.2 can only have a limit of 25% precipitation deposition. An Energy Partition Coefficient of 0.8 can have about 50% precipitation deposition. As the Energy Partition Coefficient goes up, a higher percentage of precipitation deposition is obtained.

Other than comparing a01, it is also important to look at tortuosity with different Energy Partition Coefficients and precipitation depositions. Tortuosity provides information about pore blockage. As the Energy Partition Coefficient increases, new Li_2S is more likely to deposit on top of the old Li_2S. Therefore, clusters of insoluble products are formed everywhere within the pores of the Li-S cathode. By plotting all three parameters again, an “effective zone” can be observed in Figure 24 to see the maximum limits on precipitation addition with different Energy Partition Coefficients.

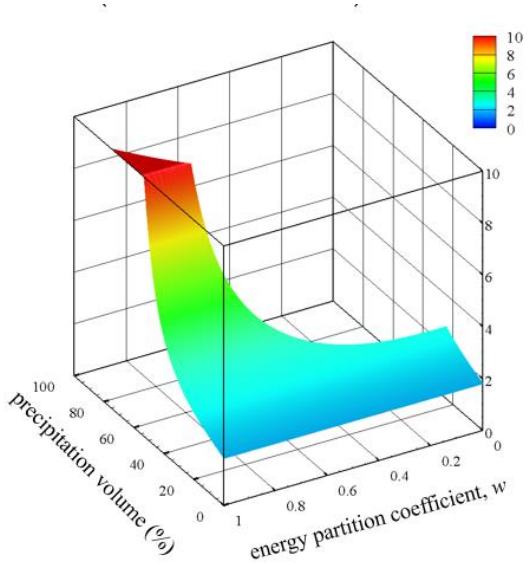

Figure 24. Energy Partition Coefficient and precipitation deposition zone for tortuosity

In Figure 24, high Energy Partition Coefficient is associated with high tortuosity. At Energy Partition Coefficient of 0.2, the tortuosity is less than 4. On the other hand, an Energy Partition Coefficient of 0.9 has a tortuosity value of 30 or higher. Using the information from Figure 23 and 24, it is possible to determine the limit for sulfur loading for different Energy Partition Coefficients as shown in Table 19.

Energy Partition Coefficient	Sulfur Loading (vol%)
0.8	~50
0.6	~35
0.4	~27
0.2	~25

Table 19. Maximum sulfur loading for different Energy Partition Coefficient

3.3 Parametric Study for Li-S Cell Discharge Performance

After obtaining the limits for sulfur loading, a parametric study was determined. As mentioned, there are a total of six parameters which could be adjusted for the study and they are C-rate (C), Energy Partition Coefficient (W), initial porosity (P), cathode thickness (CT), sulfur loading (SU) and mean pore size (PS). Based on literature reviews, a range of values was picked for each parameter and one fixed value was chosen for each parameter as shown in Table 20.

C-rate (C)	Energy Partition Coefficient (W)	Initial Porosity (P)	Cathode Thickness (CT)	Sulfur Loading (SU)	Mean Pore Size (PS)
0.5	0.2	60	20	20	1
1	0.4	70	40	30	5
2	0.6	80	80	40	10
3	0.8	90		50	

Table 20. Parametric study table

The fixed value for this parametric study was chosen as: C-rate is 1C, Energy Partition Coefficient is 0.2, initial porosity is 70 vol%, cathode thickness is 40 μm, sulfur loading is 20 vol% and mean pore size is 10 μm.

3.3.1 Sulfur Loading: Effect of Energy Partition Coefficient

Based on the previous sulfur loading limiting zone study, sixteen performance simulations were performed in Figure 25.

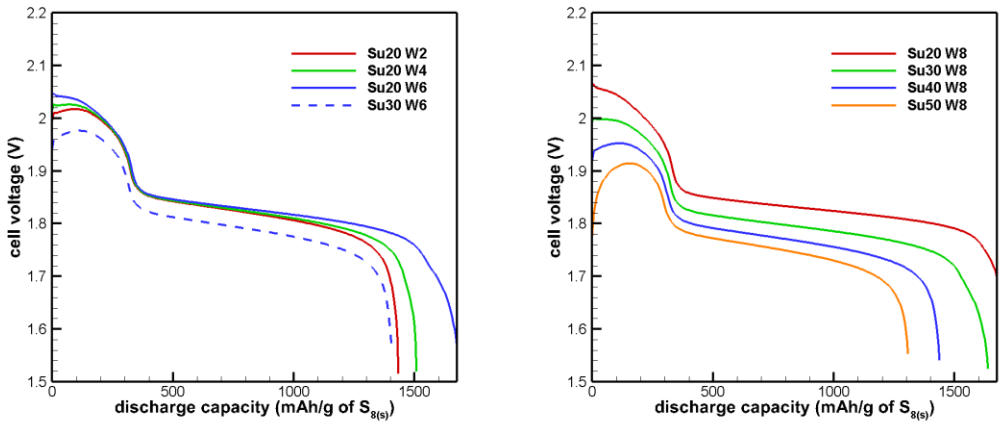

Figure 25. Sulfur Loading (Su) and Energy Partition Coefficient (W)

It can be seen in Figure 25 that there is a total of eight curves while the other eight curves are missing. At a fixed Energy Partition Coefficient of 0.2, the sulfur loading can only have an upper limit of 25%. Therefore, surface passivation has occurred before the cell discharge operation at sulfur loading of 30%, 40% and 50%. As the Energy Partition Coefficient goes up to 0.6, sulfur loading 20% and 30% can be implemented. This is because Li_2S began to have a better preference in settling on top of old precipitation at an Energy Partition Coefficient of 0.6. Lastly, sulfur loading of 20% to 50% were acceptable at an Energy Partition Coefficient of 0.8. These results directly matched the prediction based on the previous effective zone study.

3.3.2 Cathode Thickness: Effects of Sulfur Loading, Energy Partition Coefficient

As mentioned before, sulfur loading of more than 20% requires higher Energy Partition Coefficient. Therefore, the weigh factor which was used to see the effect of sulfur loading was set to 0.8 for comparison. Figure 26 shows Cathode Thickness (CT): 20, 40, 80 µm with Energy Partition Coefficient (W) of 0.8 (a) At sulfur loading (Su) of 20% (b) At sulfur loading (Su) of 20% & 30% (c) At sulfur loading (Su) of 20% & 40% (d) At sulfur loading (Su) of 20% & 50%.

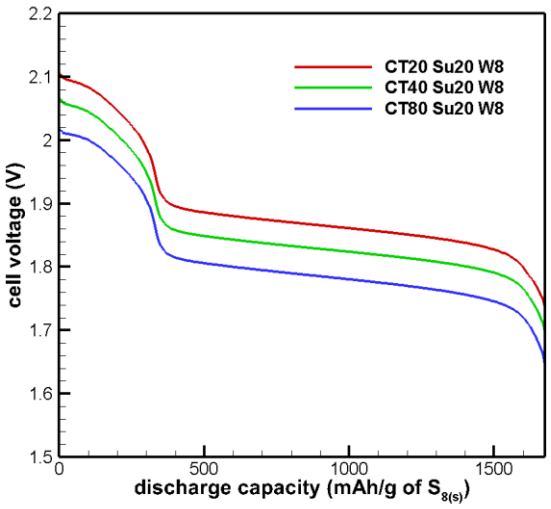

(a)

Figure 26. First discharge profile for CT: 20, 40, 80 µm with W of 0.8 (a) Su of 20% (b) Su of 20% & 30% (c) Su of 20% & 40% (d) Su of 20% & 50%

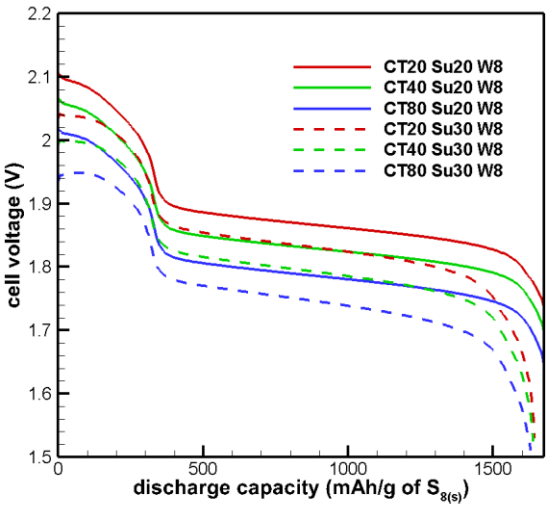

(b)

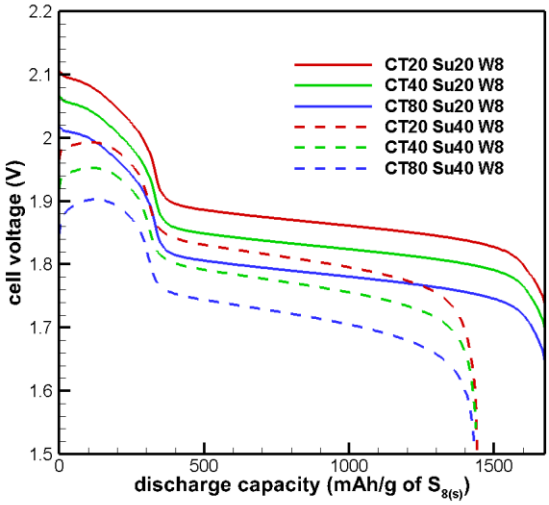

(c)

Figure 26. Continued

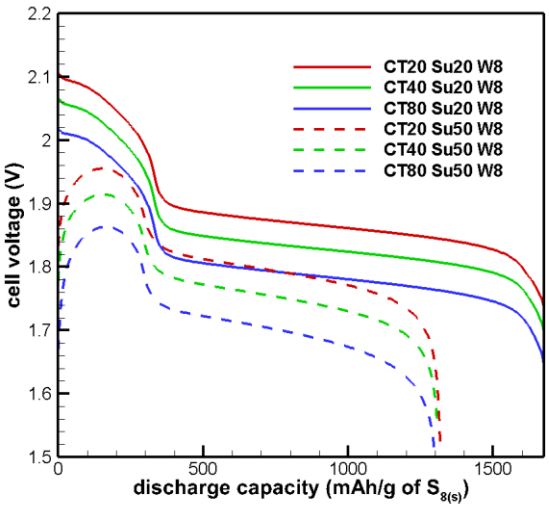

(d)

Figure 26. Continued

From Figure 26(a), CT20 has a higher cell voltage compared to the CT80 similar to literature trend. Though, all three curves reached theoretical capacity. One explanation is that the choice of Energy Partition Coefficient. At Energy Partition Coefficient of 0.8, the active area decreases slower. Therefore, surface passivation would not be able the reason in this case. As the sulfur loading increases from 20% to 50%, the discharge capacity decreases for all three cathode thicknesses. An explanation to this behavior can be explained by pore blockage as shown in Figure 27.

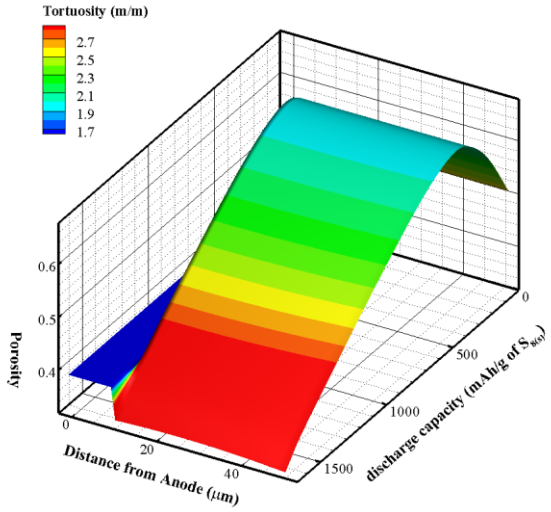

(a)

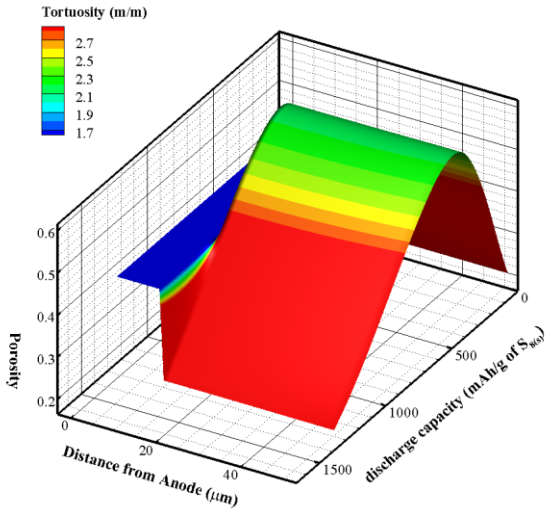

(b)

Figure 27. Tortuosity versus discharge capacity: (a) CT40 Su of 20 (b) CT40 Su of 50

In Figure 27(a) and (b), the tortuosity increases as discharge capacity increases. However, tortuosity increases rapidly for Su of 50 before the Li-S cell reaches 1000 mAh/g compared to that in Su of 20. The difference between both discharge capacities also show that Su of 50 did not have a good sulfur utilization. Based on these results, there could be an optimal limit of sulfur loading for a specific cathode thickness.

Exploring the effect of Energy Partition Coefficient on cathode thickness, Figure 28 shows cathode thickness (CT): 20, 40, 80 µm with Energy Partition Coefficient (W) of (a) 0.2 (b) 0.4 (c) 0.6 (d) 0.8.

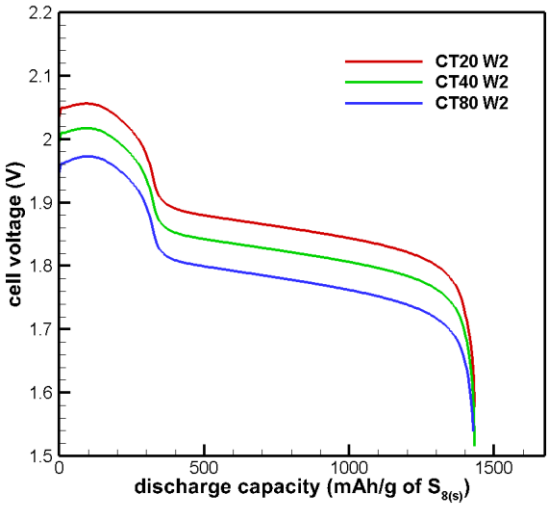

(a)

Figure 28. First discharge profile for CT: 20, 40, 80 µm with W of (a) 0.2 (b) 0.4 (c) 0.6 (d) 0.8

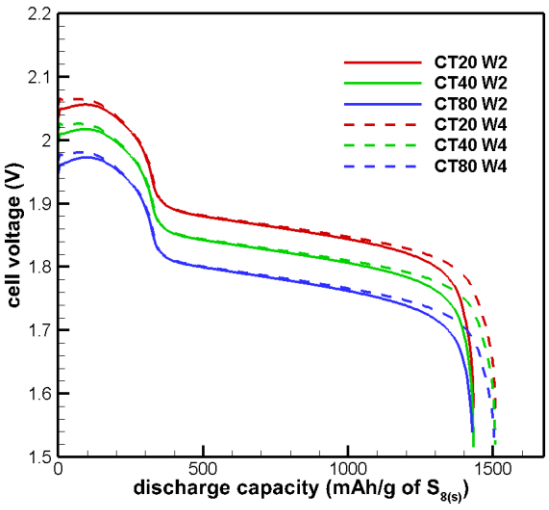

(b)

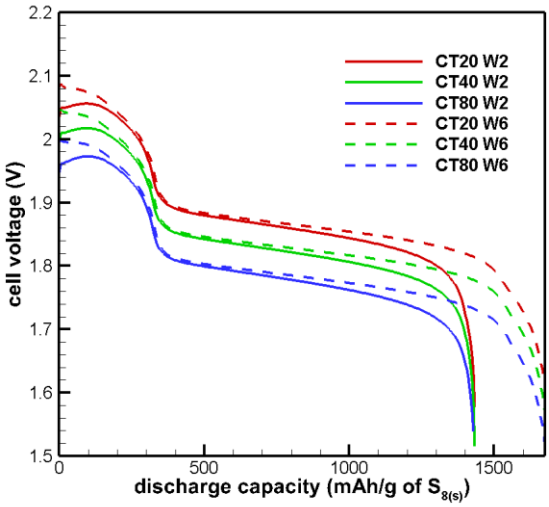

(c)

Figure 28. Continued

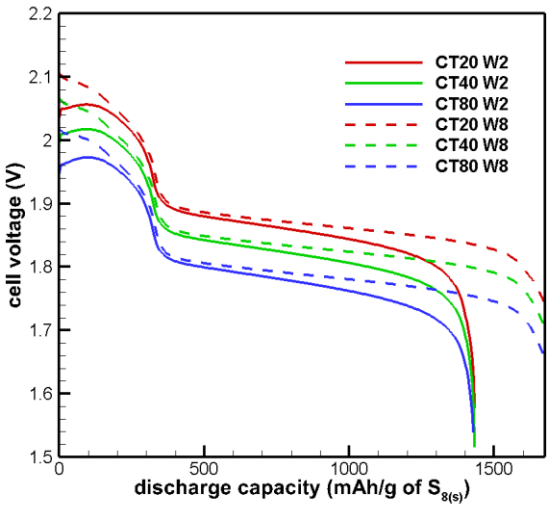

(d)

Figure 28. Continued

In Figure 28, an increase in discharge capacity was observed as the Energy Partition Coefficient goes up. This trend was explained by previous explanation. For a higher Energy Partition Coefficient, active area is much higher compared to that in a lower Energy Partition Coefficient. Comparing 28(a) and (d), all three curves have reach theoretical discharge capacity at an Energy Partition Coefficient of 0.8. As for cathode thickness, CT40 has a better discharge capacity than that of CT80 in all cases. The explanation to this behavior is that diffusion difficulty for lithium ions imposed by the extra distance from a thicker electrode. With this difficulty, more reactions take place at interface of separator and cathode. Closer toward the current collector, less lithium polysulfides are formed. Therefore, the overall sulfur utilization for the thick electrode

remains low. Figure 29 shows Tortuosity versus discharge capacity for Energy Partition Coefficient (W) of 0.2 with cathode thickness (CT): (a) 20 µm and (b) 80 µm.

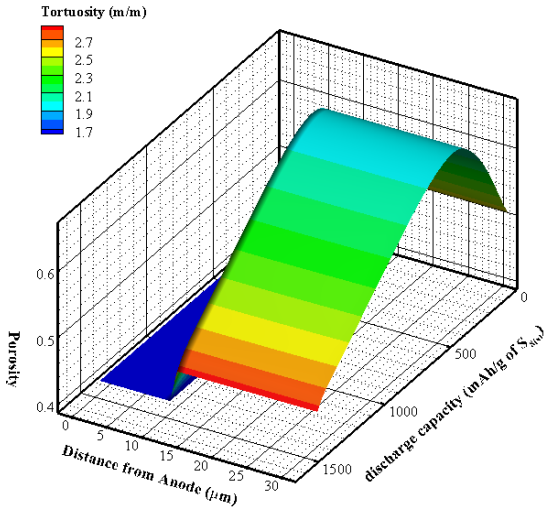

(a)

Figure 29. Tortuosity versus discharge capacity for W of 0.2 with CT: (a) 20 µm and (b) 80 µm

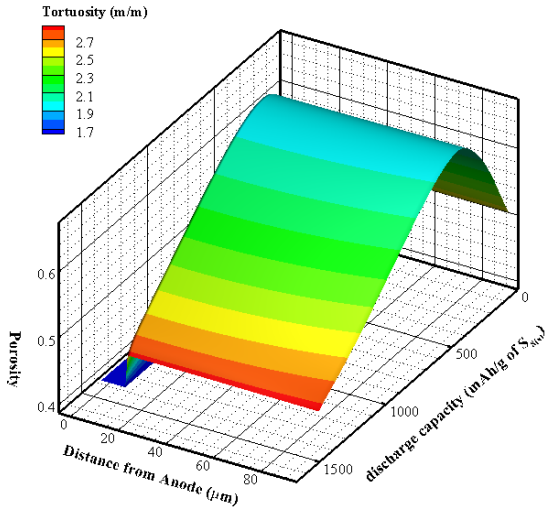

(b)

Figure 29. Continued

There is a non-uniform tortuosity distribution across the distance from anode in 29(b) compared to that in 29(a). The non-uniform tortuosity could directly explain the uneven sulfur utilization for thicker electrode. Aside from sulfur loading, it is also noteworthy to compare cathode thickness of 80 μm with different Energy Partition Coefficient as shown in Figure 30.

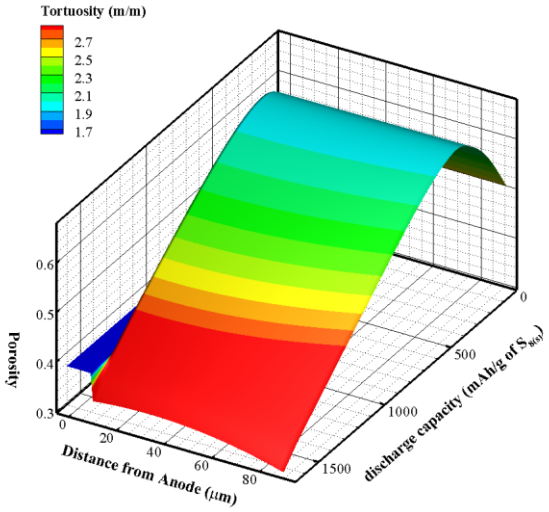

(a)

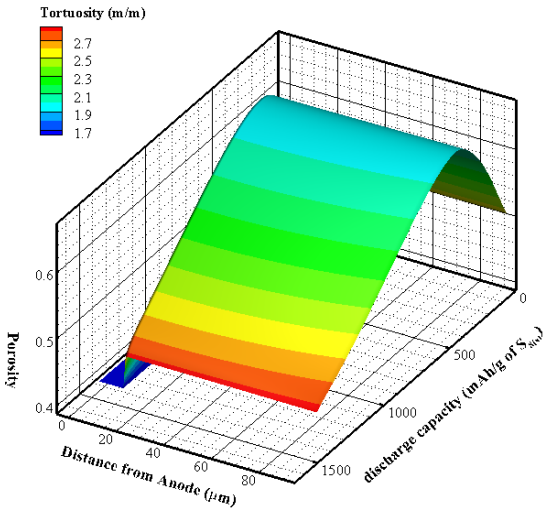

(b)

Figure 30. Tortuosity versus discharge capacity for CT80 with Energy Partition Coefficient of (a) 0.8 (b) 0.2

Surface passivation occurs much earlier for Energy Partition Coefficient of 0.2. Although the tortuosity increases a lot toward the end of discharge in 30(a), the Li-S cell could continue.

3.3.3 Porosity: Effects of C-rate, Sulfur Loading and Cathode Thickness

Typically, initial porosity for Li-S cell ranges from 60% to 90%. Different volume fractions of conductive materials could affect the discharge behavior. It is necessary to see how porosity affected by these parameters. Figure 31 shows initial porosity (P) of the Li-S cathode: 60%, 70%, 80%, 90% with: (a) 1C (b) 1C and C/2 (c) 1C and 2C and (d) 1C and 3C.

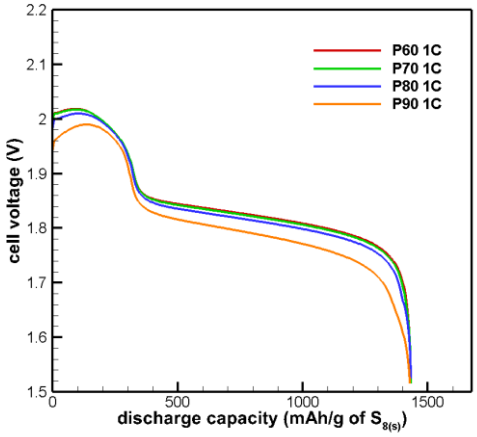

(a)

Figure 31. First discharge profile for P: 60%, 70%, 80%, 90% with (a) 1C (b) 1C and C/2 (c) 1C and 2C and (d) 1C and 3C

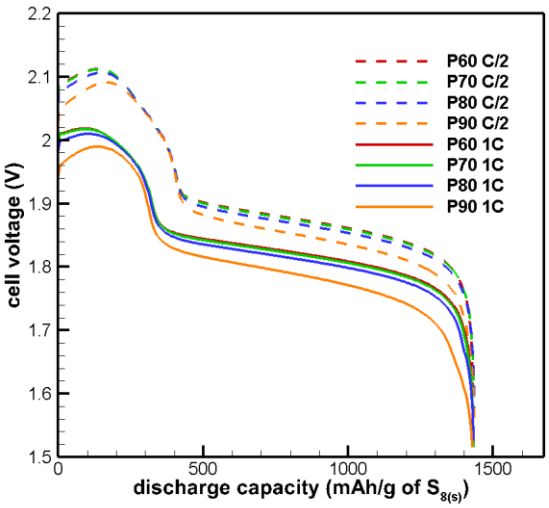

(b)

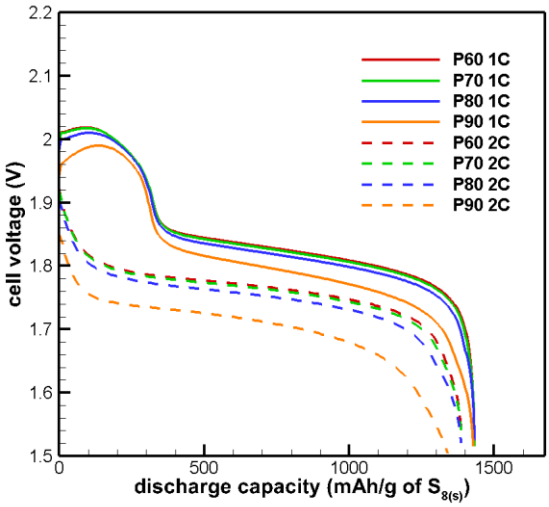

(c)

Figure 31. Continued

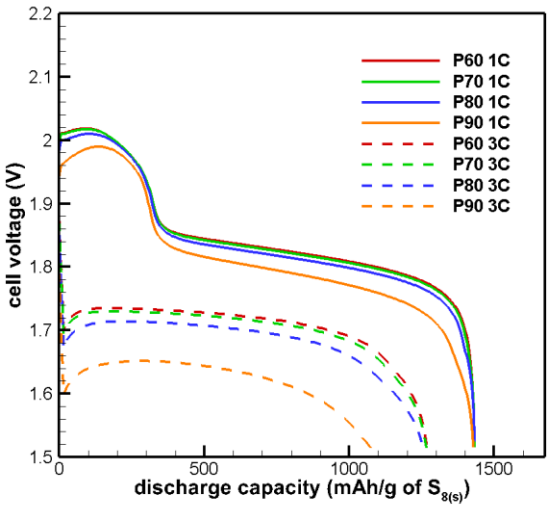

(d)

Figure 31. Continued

In Figure 31(a), initial porosities of 60% to 90% have a similar discharge capacity. However, initial porosities of 90% has a lower cell voltage. Similarly, a small difference was observed for C/2. Typically, a high active area is closely associated with 60% initial porosity. This is mainly due to higher volume fraction of conductive material. From C/2 to 3C, 60% initial porosity has a better performance. Interestingly, the difference in discharge capacity goes up for 60% initial porosity as the C-rate goes from 1C to 3C as shown in Figure 31(c) and (d). Figure 32 shows S_8 utilization versus discharge capacity for 60% initial porosity at (a) 1C (b) 3C.

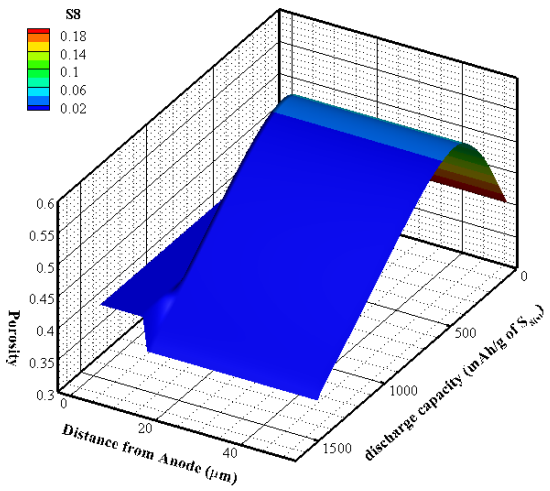

(a)

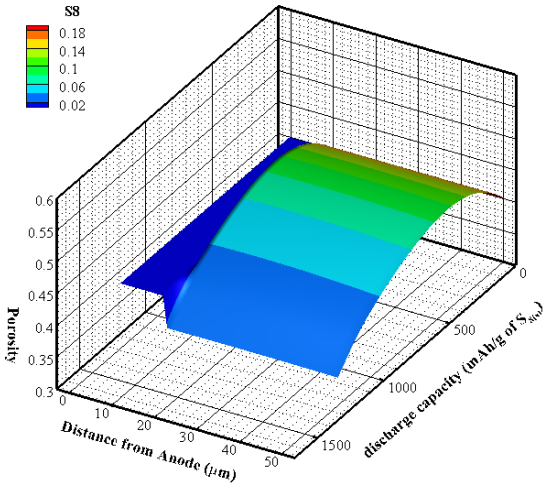

(b)

Figure 32. S8 utilization versus discharge capacity for 60% initial porosity at (a) 1C (b) 3C

In Figure 32(a), there is a high concentration of S_8 initially. As the discharge capacity increases, concentration of S_8 significantly decreases. Based on the plot, sulfur is being utilized well at 1C compared to that in 3C. Figure 32(b) shows that not only S_8 was not highly utilized initially, but a higher concentration remains unused till the end which could explain the significant reduction in discharge capacity. After comparing different C-rate, S_8 utilization versus discharge capacity was also compared for 60% and 90% initial porosity as shown in Figure 33.

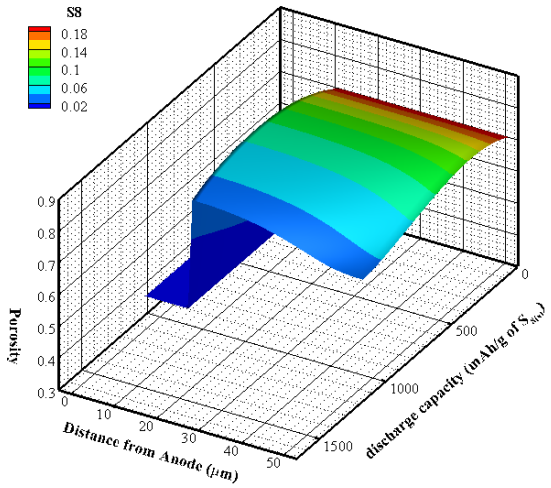

(a)

Figure 33. S8 utilization versus discharge capacity at 3C for initial porosity of: (a) 90% (b) 60%

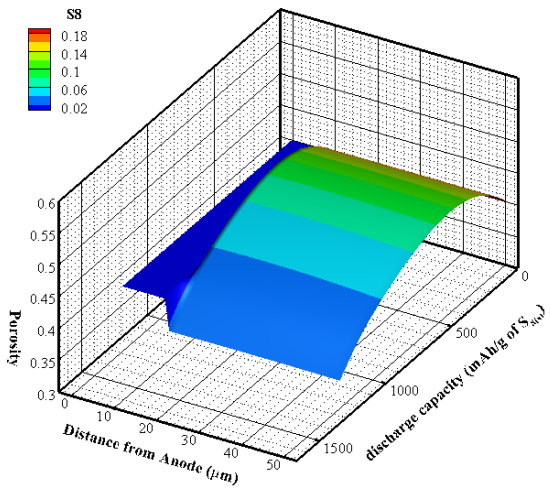

(b)

Figure 33. Continued

Herein, 60% initial porosity has a better sulfur utilization compared to that in 90% initial porosity. At a 60% initial porosity, there is higher active area since it contains a higher volume fraction of conductive material. For 90% porosity, there is only 10% volume fraction of conductive material. Therefore, the active area is limited and surface passivation occur at an earlier stage.

Next, the effect of sulfur loading was studied for various initial porosities. It should be noted that Energy Partition Coefficient of 0.8 was chosen again to observe the effect of higher sulfur loading. Figure 34 shows the effect of sulfur loading for initial porosity of 60%, 70%, 80% and 90%.

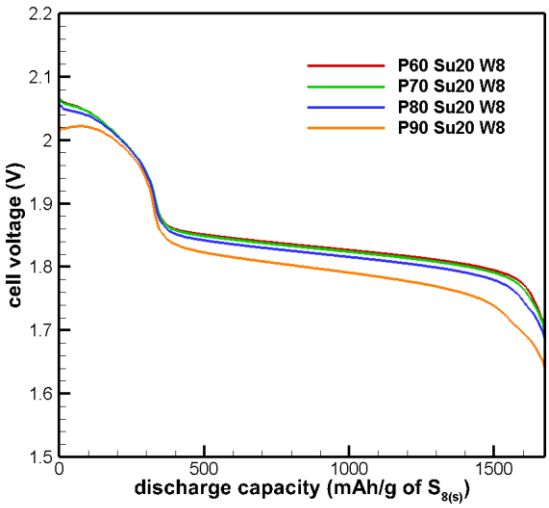

(a)

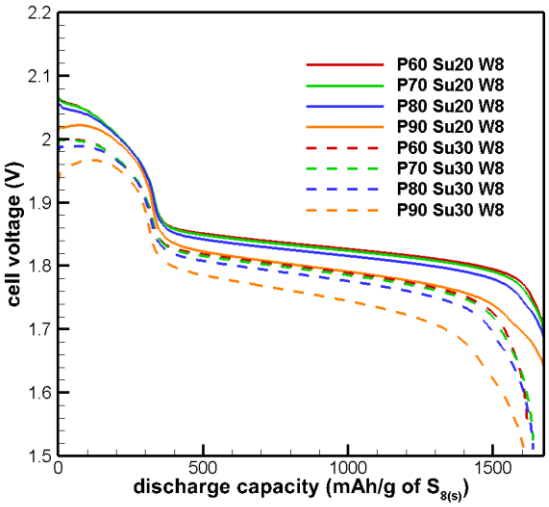

(b)

Figure 34. First discharge profile for P: 60%, 70%, 80%, 90% with W of 0.8 (a) Su of 20% (b) Su of 20% and 30% (c) Su of 20% and 40% (d) Su of 20% and 50%

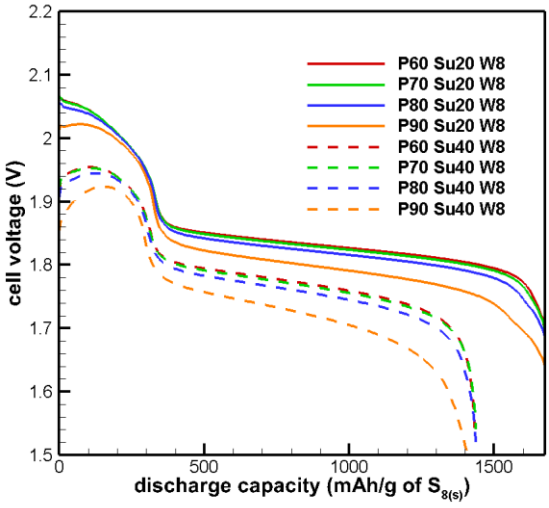

(c)

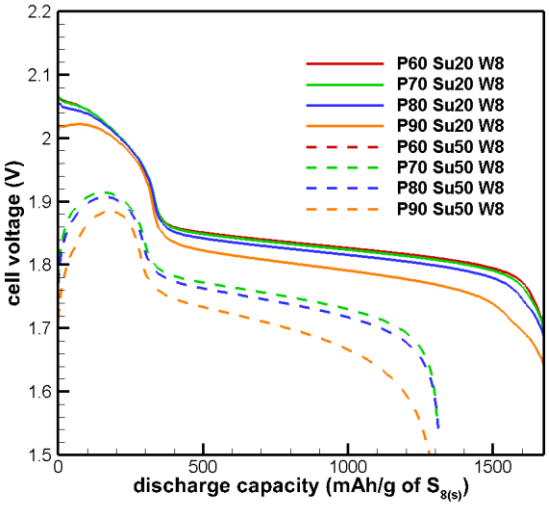

(d)

Figure 34. Continued

As the sulfur loading increases, the discharge capacity decreases for all porosities. High volume fraction of active material is not entirely desirable because surface passivation could happen beforehand which render the Li-S cell useless. Interesting, two unique discharge behaviors were found in Figure 34(b) and (d). In Figure 34(d), 60% initial porosity did not have any discharge capacity at all at sulfur loading of 50%. This result signifies the Li-S cathode was completely covered by sulfur where there is no possible way for electrochemical reactions to happen. In contrast, higher porosity was found to be more tolerable for high sulfur loading. In Figure 34(b), initial porosity of 60% has a worse performance toward the end compared to that of initial porosity of 70% and 80%. Typically, initial porosity of 60% should contain a higher active area which means it should have a better discharge capacity theoretically. However, this result completely opposed this trend. Herein, Figure 35 shows a tortuosity versus discharge capacity comparison between initial porosity of 60% and 70% with sulfur loading of 30% and Energy Partition Coefficient of 0.8.

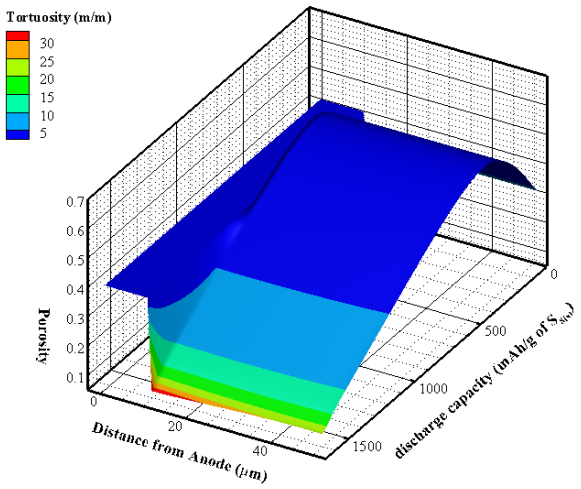

(a)

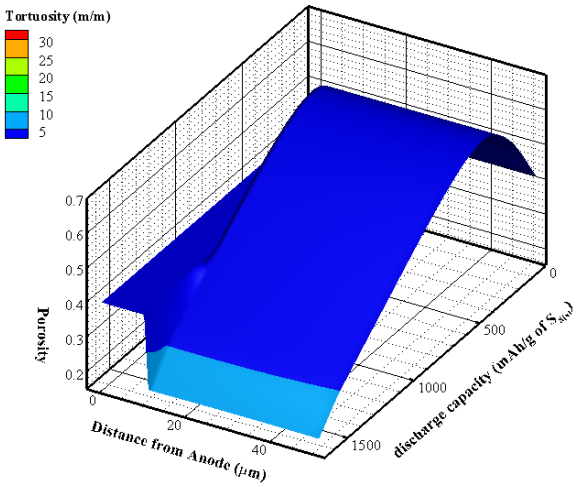

(b)

Figure 35. Tortuosity versus discharge capacity for initially porosity: (a) 60% (b) 70% at sulfur loading of 30% and Energy Partition Coefficient of 0.8

At a sulfur loading of 30%, tortuosity for 60% initial porosity reaches as high as 30 while 70% initial porosity reaches as high as 8. This results strongly indicate pore blockages. Porosity reaches to less than 20% for both Li-S cell and they did not reach theoretical capacity. In addition, 60% initial porosity has a tortuosity value of 5 or less initially while 70% initial porosity only reaches a tortuosity value of 8 toward the end of discharge. Based on these results, it can be concluded that there is an existing optimal sulfur loading for different porosities. Aside from this unique discharge behavior, it is also noteworthy to consider high sulfur loading. As mentioned previously, 90% initial porosity exhibits a poor performance compared to that of 70% initial porosity with a sulfur loading of 50%. Figure 36 shows the insoluble products Li_2S concentration versus discharge capacity for both 70% and 90% initial porosity.

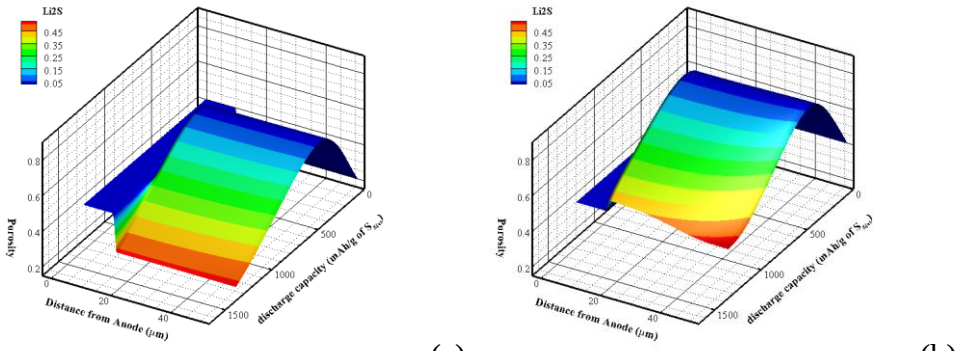

Figure 36. Li2S concentration versus discharge capacity for initially porosity: (a) 70% (b) 90% at sulfur loading of 50% and Energy Partition Coefficient of 0.8

As shown in Figure 36(b), the porosity fluctuates across the cathode. Uneven distribution of Li_2S was observed for 90% initial porosity over the discharge time. The result indicates a direct correlation between conductive material and maximum sulfur loading. For 90% initial porosity, the active area is significantly lower than 70% initial porosity. With a high concentration of sulfur, more active area is required. When active area is limited, uneven distribution of Li_2S are seen everywhere across the cathode.

Next, a study was conducted with the effect of cathode thickness. Figure 37 shows cathode thickness (CT) of 20µm, 40µm, 80µm for initial porosity (P) of: 60%, 70%, 80% and 90%.

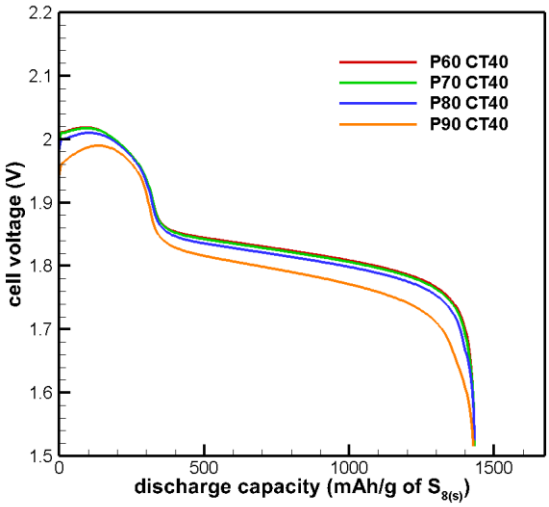

(a)

Figure 37. First discharge profile for P: 60%, 70%, 80%, 90% with CT of (a) 40µm (b) 20µm and 40µm (c) 40µm and 80µm

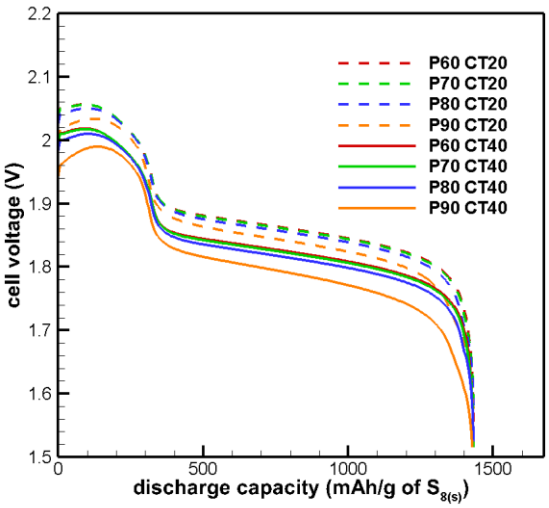

(b)

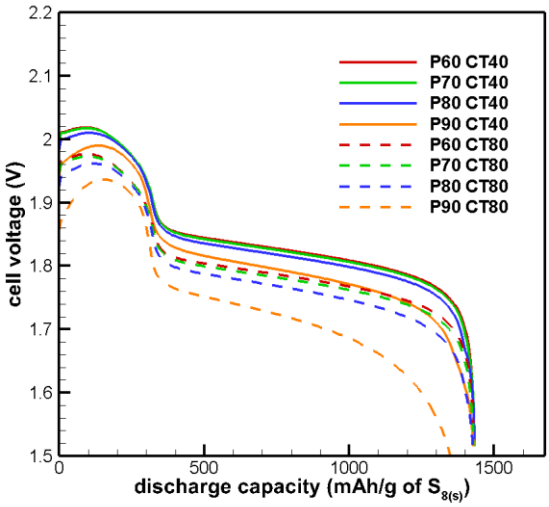

(c)

Figure 37. Continued

Cathode thickness 20µm and 40µm have a similar discharge capacity. Interestingly, a great difference was observed with 90% initial porosity between cathode thickness of 40µm and 80µm in Figure 37(b) and (c). This difference could be mainly due to pore blockage as shown in Figure 38.

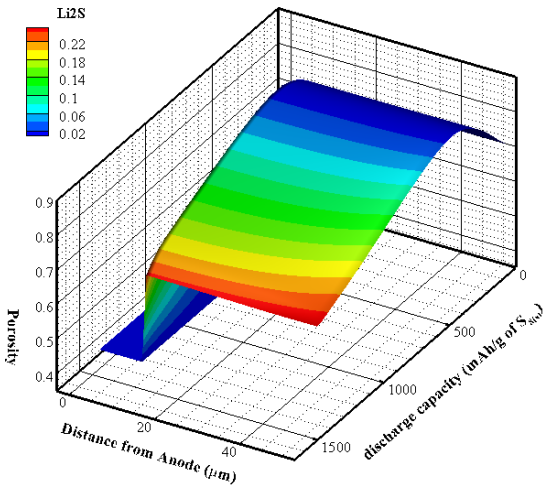

(a)

Figure 38. Li2S concentration versus capacity for initial porosity of 90% at CT: (a) 40µm (b) 80µm

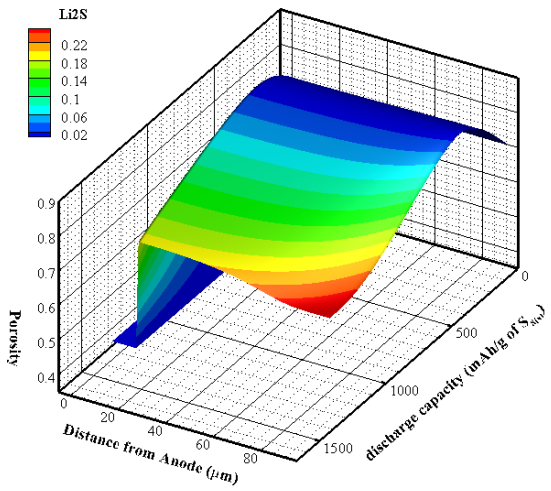

(b)

Figure 38. Continued

As shown in Figure 38(a) and (b), there is a higher concentration of Li_2S early on for initial porosity of 90% at cathode thickness of 80μm. The Li_2S settles early on within the thicker cathode which causing pore blockage. Another strong indicator of early pore blockage is the uneven porosity distribution across the cathode in 38(b). The porosity fluctuates a lot at a fixed discharge capacity compared to that in 38(a).

3.3.4 Mean Pore Size: Effects of C-rate, Sulfur Loading and Cathode Thickness

Mean pore size has a well-known correlation with pore blockage. In the first study, the effect of C-rate was conducted with mean pore size. Figure 39 shows the effect of C-rate (C) with different mean pore size (PS).

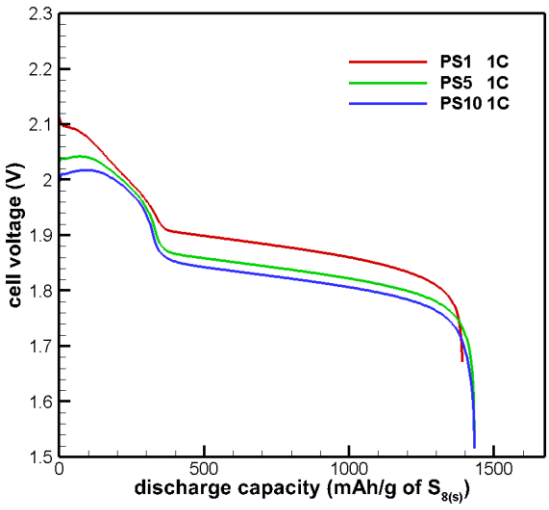

(a)

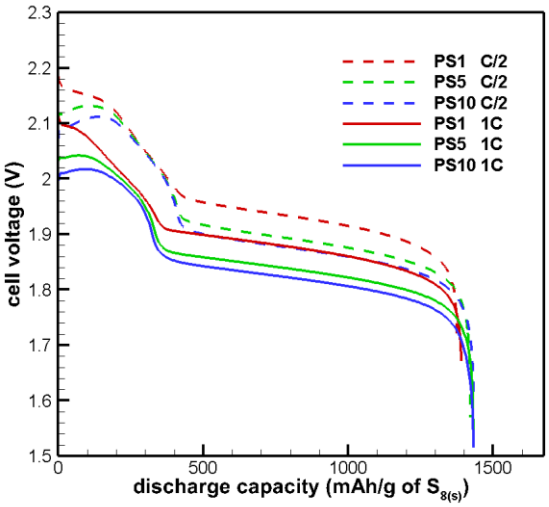

(b)

Figure 39. First discharge profile for PS: 1µm, 5µm, 10µm (a) 1C (b) C/2 and 1C (c) 1C and 2C (d) 1C and 3C

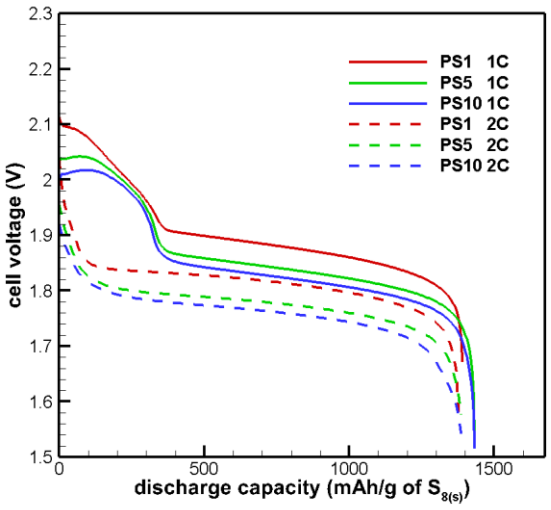

(c)

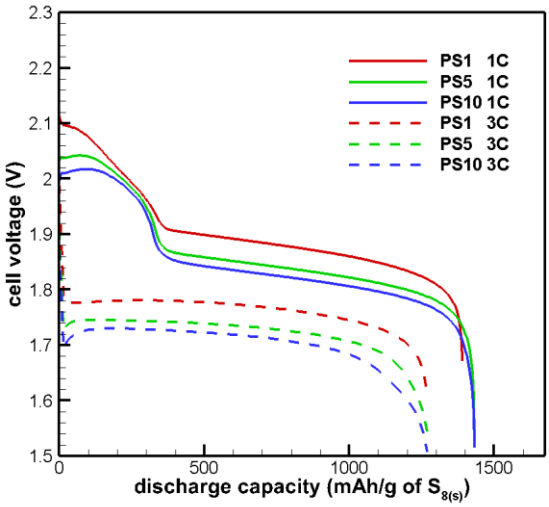

(d)

Figure 39. Continued

At 1C discharge rate, the Li-S cathode with a mean pore size of 1µm was terminated earlier compared to the mean pore size of 5µm and 10µm. This result does not follow the typical trend because smaller mean pore size usually indicates more active area for electrochemical reactions. Interestingly, the smaller particle size was found to have a better performance when a higher C-rate was applied. Tortuosity versus discharge capacity was conducted between mean pore size of 1µm and 10µm at 1C as shown in Figure 40.

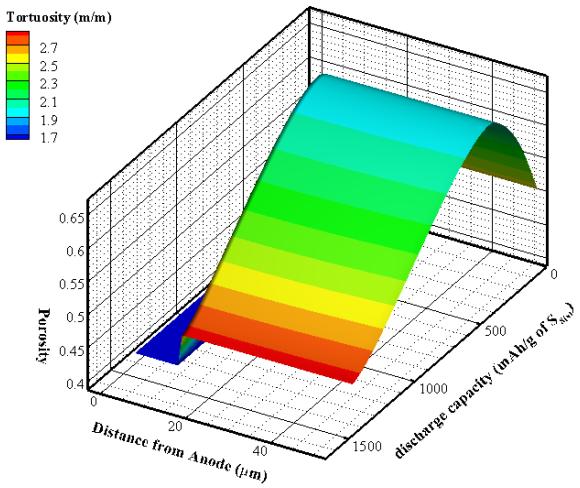

(a)

Figure 40. Tortuosity versus discharge capacity for PS: (a) 1µm (b) 10µm at 1C

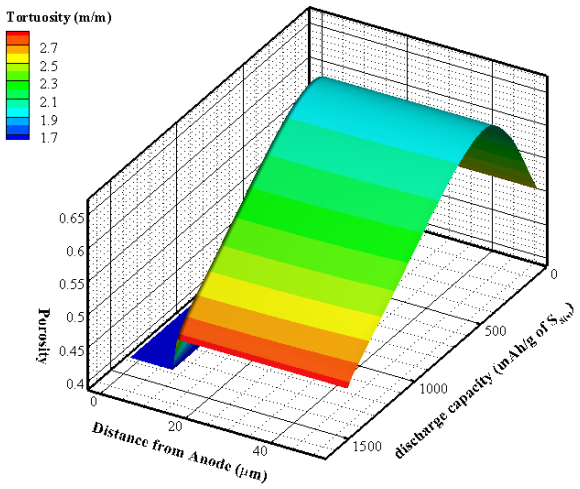

(b)

Figure 40. Continued

The tortuosity is slight higher for 1µm compared to that in 10µm. The results strongly prove that the discharge capacity for 1µm was ended early due to combination of surface passivation and pore blockage. The increase in tortuosity indicated that higher concentration of Li_2S was formed in the toward the end of discharge. These clusters of Li_2S actively block the pores which prevents further electrochemical reactions as shown in Figure 41.

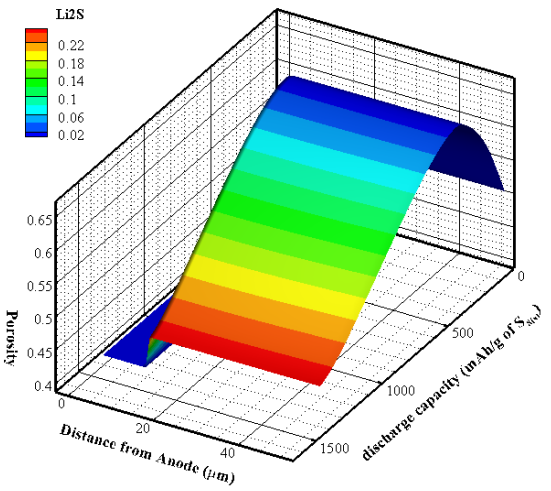

(a)

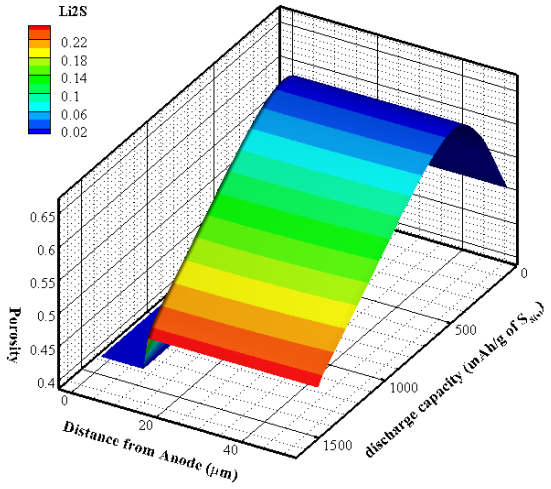

(b)

Figure 41. Li2S concentration versus discharge capacity for PS: (a) 1μm (b) 10μm at 1C

In Figure 41, a higher concentration of Li_2S was found in later stage of discharge. This result indicates that larger mean pore size allows a more even distribution of insoluble products compared to smaller mean pore size. Although larger mean pore size has less active area, its porous advantage reduced the severity of pore blockage.

Next, the effect of the sulfur loading was investigated. Again, it should be noted that an Energy Partition Coefficient of 0.8 was used here to full see the effect of higher sulfur loading. Figure 42 shows the effect of sulfur loading (Su) for various mean particle sizes (PS).

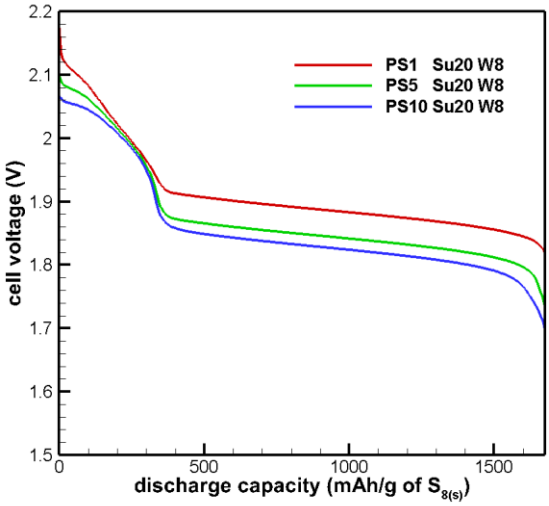

(a)

Figure 42. First discharge profile for PS: 1µm, 5µm, 10µm with Su of 50% and W of 0.8

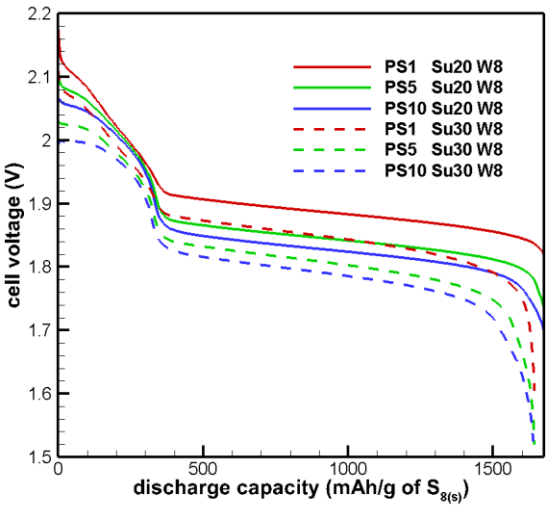

(b)

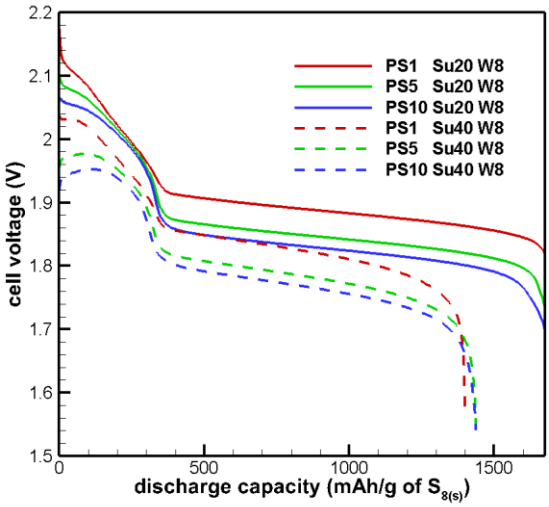

(c)

Figure 42. Continued

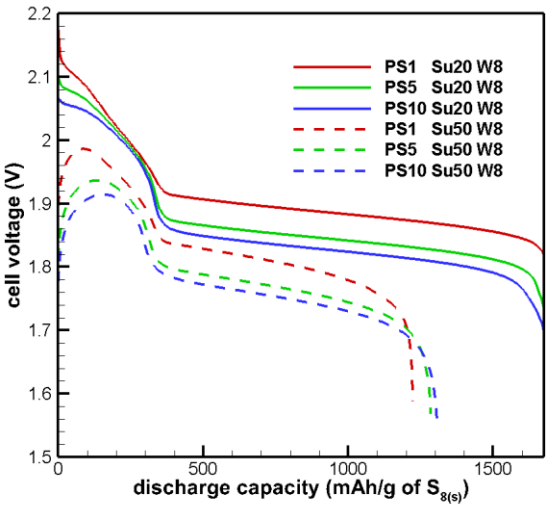

(d)

Figure 42. Continued

At a sulfur loading of 20%, a high cell voltage and performance was seen for mean pore size of 1µm. This result is expected because smaller pore size has a higher active area. However, the discharge capacity was slowly decreasing for mean pore size of 1µm as sulfur loading increases. At sulfur loading of 40% and 50% in Figure 42(c) and (d), mean pore size of 1µm has a lower discharge capacity compared to mean pore size of 5µm and 10µm. It is noteworthy to investigate the reasoning behind this behavior. Figure 43 shows the tortuosity versus discharge capacity for mean pore size: (a) 1µm (b) 10µm at sulfur loading of 50% with Energy Partition Coefficient of 0.8.

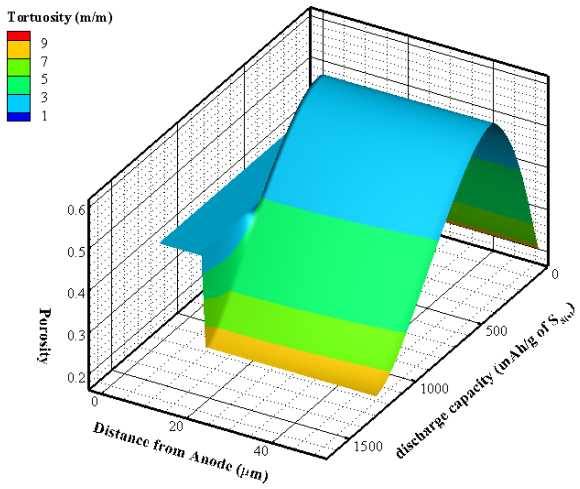

(a)

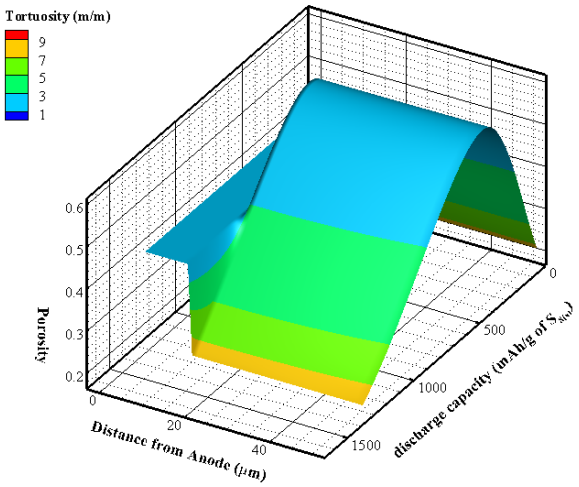

(b)

Figure 43. Tortuosity versus discharge capacity for PS: (a) 1μm (b) 10μm at Su of 50% with W of 0.8

The tortuosity value remains close for both cases initially. As the end of discharge approaches, the tortuosity value is slightly higher for 1µm which could be the reason for the difference in discharge capacity between both cases. At a high sulfur loading, smaller mean pore size might be not desirable because agglomeration of insoluble products can cause the Li-S cell to terminate earlier. This result provides insight into a potential limit on sulfur loading with a specific mean pore size.

Lastly, a study was conducted on the effect of cathode thickness. Figure 44 show the effect of cathode thickness (CT) with different mean pore sizes (PS).

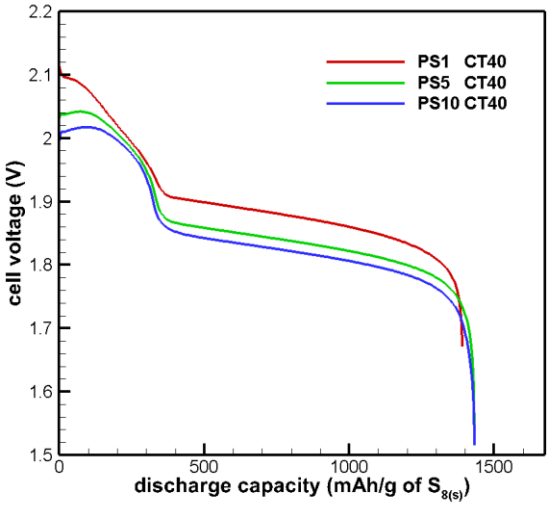

(a)

Figure 44. First discharge profile for mean pore size: 1µm, 5µm, 10µm at CT (a) 40µm (b) 20µm and 40µm (c) 40µm and 80µm

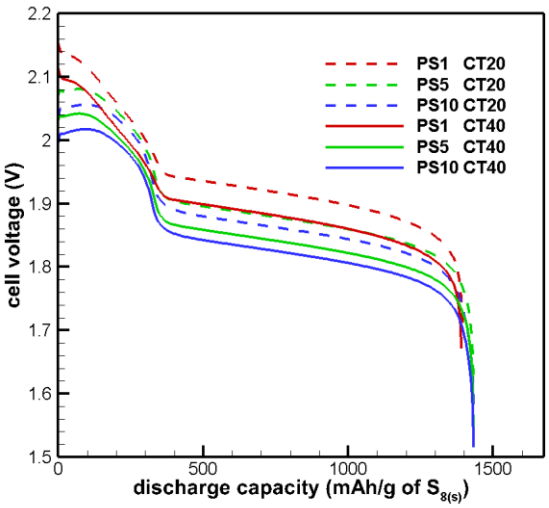

(b)

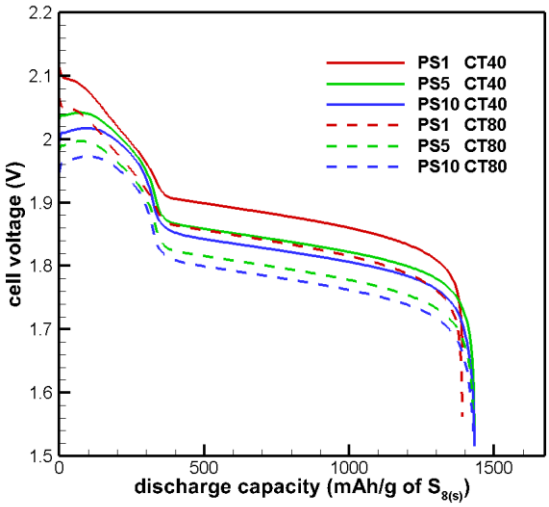

(c)

Figure 44. Continued

As cathode thickness increases, the discharge capacity for all three mean pore sizes also decreases. Mean pore size of 10µm has a better discharge capacity compared to mean pore size of 1µm. This is mainly due to pore blockage. As more insoluble products are formed, smaller pores are easily blocked out which causes difficulty for lithium ions to travel further toward the current collector side. Figure 45 shows the Li_2S concentration versus discharge capacity.

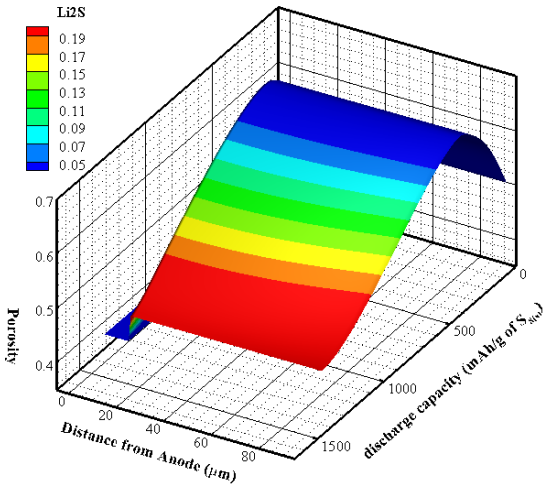

(a)

Figure 45. Li2S concentration versus discharge capacity for PS: (a) 1µm (b) 10µm at cathode thickness of 80µm

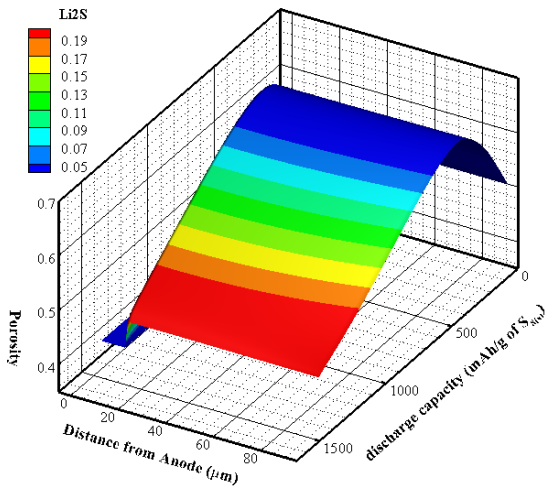

(b)

Figure 45. Continued

Comparing Figure 45(a) and (b), There is a higher concentration of Li_2S for 1μm at an earlier discharge capacity. In addition, the porosity fluctuates a little across cathode for 1μm.

3.3.5 Initial Porosity and Mean Pore Size

The last study was conducted between initial porosity and mean pore size. The combination of the two parameters might have different effects to the overall discharge behavior. Figure 46 shows the first discharge profile with multiple combinations of porosity and mean pore size.

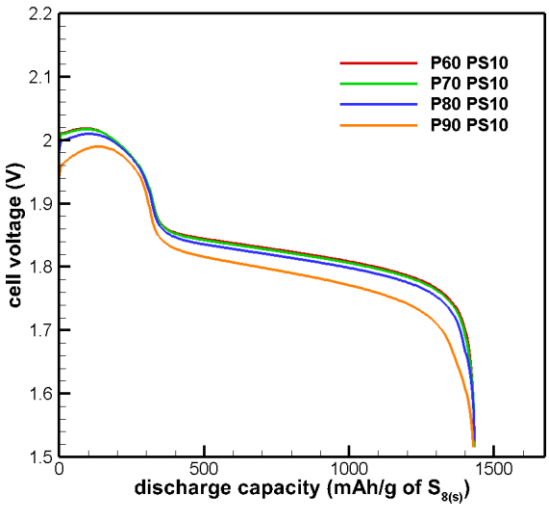

(a)

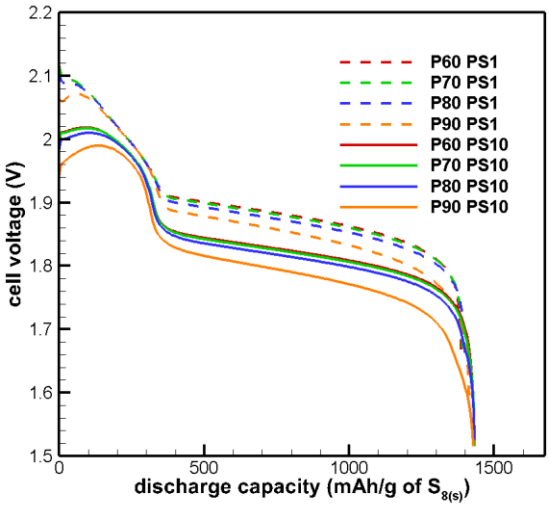

(b)

Figure 46. First discharge profile for initial porosity: 60%, 70%, 80% and 90% at mean pore size of (a) 10µm (b) 1µm and10µm (c) 5µm and10µm

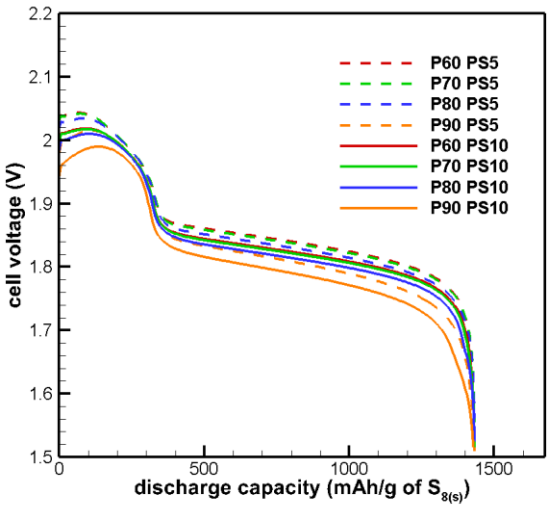

(c)

Figure 46. Continued

It is rather difficult to see the performance difference in Figure 46. Therefore, Figure 47 shows two different cases comparison for reference.

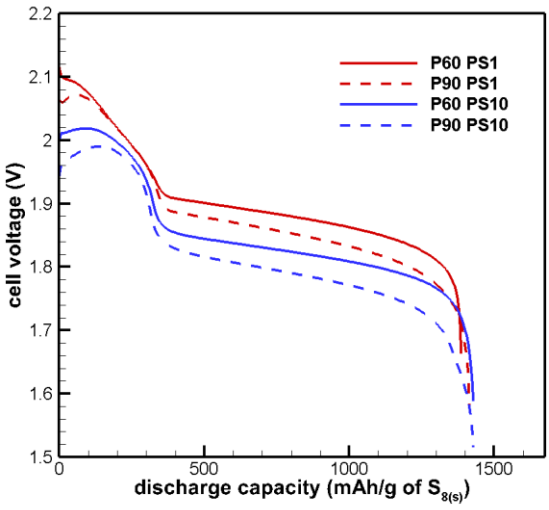

(a)

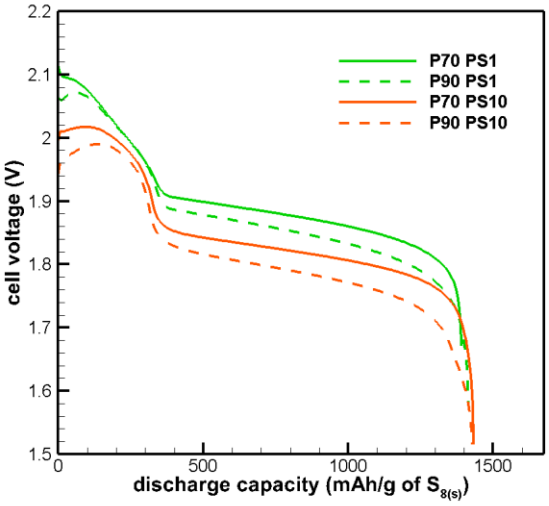

(b)

Figure 47. First discharge profile for (a) 60% and 90% initial porosity (P) with mean pore size (PS) of 1µm and 10µm (b) 70% and 90% initial porosity with mean pore size of 1µm and 10µm

As shown in Figure 47(a), mean pore size of 1µm for 90% initial porosity has a better discharge capacity compared to 60% initial porosity. This result is unique because 60% initial porosity should have a higher amount of active area as well as higher volume fraction of conductive material. Thus, a better discharge capacity should be obtained with 60% initial porosity. However, a combination of surface passivation and pore blockage provide a significant detrimental effect on the 60% initial porosity with mean pore size of 1µm. Figure 48 shows tortuosity versus discharge capacity for both cases.

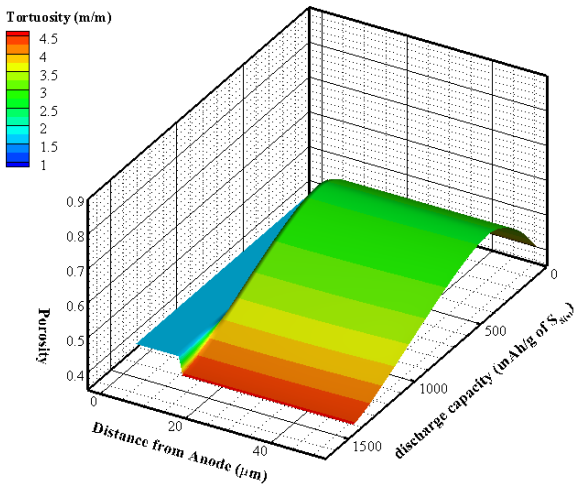

(a)

Figure 48. Tortuosity versus discharge capacity: (a) Initial porosity of 60% and mean pore size of 1µm (b) Initial porosity of 90% and mean pore size of 1 µm

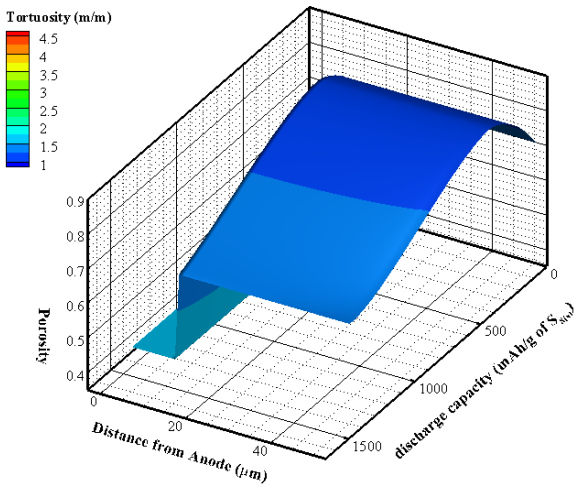

(b)

Figure 48. Continued

As shown in Figure 48, the tortuosity was significantly higher in (a) compared to that in (b). While tortuosity for initial porosity of 60% and mean pore size of 1μm reaches up to 4.5, the tortuosity for initial porosity of 90% and mean pore size of 1 μm only reaches up to 1.5. This results clearly demonstrate smaller pore size might not be good due to pore blockage. For both cases, the discharge capacity did not reach theoretical capacity which indicates that surface passivation also contributed as well. Figure 49 shows Li_2S concentration versus discharge capacity for both cases.

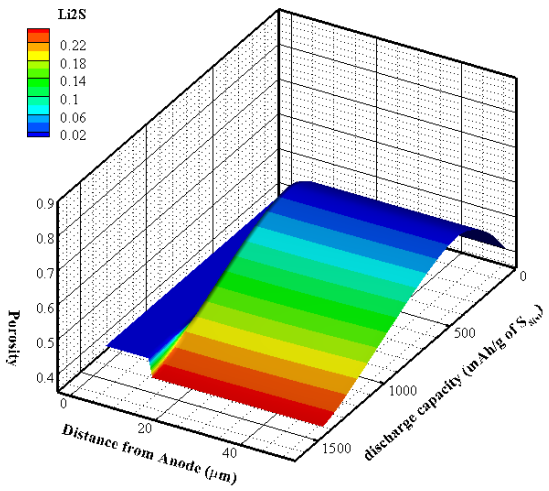

(a)

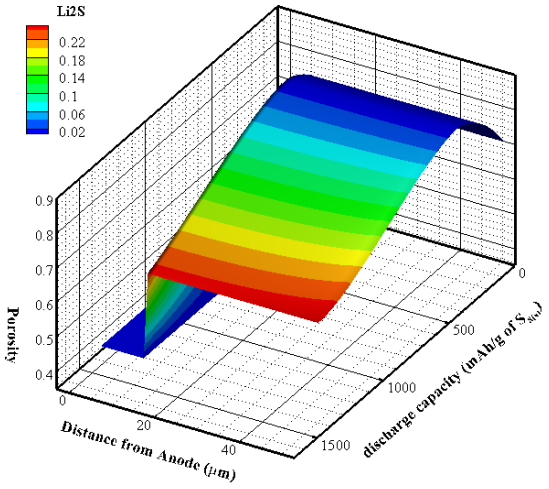

(b)

Figure 49. Li_2S concentration versus discharge capacity: (a) Initial porosity of 60% and mean pore size of 1μm (b) Initial porosity of 90% and mean pore size of 1μm

As seen in both cases, high concentration of Li_2S are seen in middle to the end of discharge. Interestingly, an opposite trend was observed as the mean pore size increases from 1μm to 10μm. The discharge capacity for 60% initial porosity has a higher discharge capacity compared to that in 90% initial porosity.

4. CONCLUSION AND FUTURE WORK

Due to challenges in Li-S sulfur cells, a standardized approach was implemented and used to provide a guideline for choosing specific microstructural properties for Li-S cathode based on its performance. In this approach, mesoporous structure was chosen for the study. Multiple microstructures were stochastically created with a commercial software. A thorough statistical study was conducted to determine a good and sufficient representation of Li-S cathode microstructure.

After conducting statistical study, microstructures were created with varying porosities and volume fractions of conductive material. Evolution of the primary structures can be created through the precipitation deposition. Herein, transport properties such as effective conductivity, tortuosity and active area were calculated for each individual microstructure at different evolution stages. Large scale data collections for transport properties were conducted over so many microstructures. Through data comparison, multiple correlations were made between transport properties and microstructural properties. The three main transport properties for this study are effective conductivity, tortuosity and effective interfacial active area. All three properties are directly correlated to porosity, precipitation addition and Energy Partition Coefficients.

Next, a mathematical model was developed to calculate the discharge capacity of Li-S cell. This mathematical model contains species and charge conservation equations which describe a Li-S cell operation within a closed system. In addition, these

conservation equations are influenced by effective conductivity, tortuosity and active area. Through implementation of all three correlations, Li-S cell discharge behavior can be affected by either surface passivation or pore blockage.

Before the discharge performance study, the model was tested to see if it exhibits similar trend found in experimental results. The model was validated with three different cases and they are C-rate, cathode thickness and sulfur loading. Lastly, discharge performance study was conducted with six operation conditions which are C-rate, cathode thickness, sulfur loading, initial porosity, mean pore size and Energy Partition Coefficient. Cathode thickness, initial porosity and mean pore size are the three main microstructural properties focused for this study. Throughout the entire study, surface passivation and pore blockage were observed with different operation conditions.

Based on the results, some future work recommendations would be side reactions and capacity fade, rate capability, temperature dependent performance and other carbon structures. For side reactions, investigation could be conducted with electrolyte. As of now, only the initial discharge performance was investigated. Therefore, it is noteworthy to see the effect of long term cycling through simulations. Operating temperature is a well-known factor which affects the kinetics of the electrochemistry inside a battery. Carbon structure such as graphene, carbon fiber, carbon nanotube could also be investigated in the future. The methodology for this thesis could be used to simulate unique discharge behavior for Li-S cell and predict its performance based on its initial microstructure. Using these results, the overall performance of Li-S cell can be greatly improved.

REFERENCES

1. Ji, X., & Nazar, L. F., *Advances in Li–S batteries.* Journal of Materials Chemistry, 2010. **20**: p. 9821–9826.

2. Song, M. K., Cairns, E. J., Zhang, Y., *Lithium/sulfur batteries with high specific energy: old challenges and new opportunities.* Nanoscale, 2012. **5**: p. 2186–2204.

3. Kumaresan, K., Mikhaylik, Y., White, R. E., *A mathematical model for a lithium–sulfur cell.* Journal of the Electrochemical Society, 2008. **155**(8): p. A576-A582.

4. Pope, M. A., Aksay, I. A., *Structural design of cathodes for Li-S batteries.* Advanced Energy Materials, 2015. **5**: p. 1-22.

5. Mikhaylik, Y. V., Akridge, J. R., *Polysulfide shuttle study in the Li/S battery system.* Journal of the Electrochemical Society, 2004. **151**(11): p. A1969-A1976.

6. Eon Sung Shin, K.K., S. H.O., W. I. C., *Polysulfide dissolution control: the common ion effect.* Chemical Communications, 2012. **49**: p. 2004-2006.

7. Shin, E. S., Kim, K., Oh, S. H., Cho, W. I., *A highly ordered nanostructured carbon–sulphur cathode for lithium–sulphur batteries.* Nature Materials, 2009. **8**: p. 500-506.

8. Song, M. S., Han, S. C., Kim, H. S., Kim, J. H., Kim, K. T., Kang, Y. M., Lee, J. Y., *Effects of nanosized adsorbing material on electrochemical properties of Sulfur cathodes for Li/S secondary batteries.* Journal of the Electrochemical Society, 2004. **151**(6): p. A791-A795.

9. Song, J., Xu, T., Gordin, M. L., Zhu, P., Lv, D., Jiang, Y. B., Wang, D., *Nitrogen-Doped Mesoporous carbon promoted chemical adsorption of sulfur and fabrication of high-areal-capacity sulfur cathode with exceptional cycling stability for lithium-sulfur batteries.* Advanced Functional Materials, 2014. **24**(9): p. 1243–1250.

10. Ji, L., Rao, M., Zheng, H., Zhang, L., Li, Y., Duan, W., Zhang, Y., *Graphene oxide as a sulfur immobilizer in high performance lithium/sulfur cells.* Journal of the American Chemical Society, 2011. **133**: p. 18522–18525.

11. Jing, H. K., Kong, L. L., Liu, S., Li, G. R., Gao, X. P., *Protected lithium anode with porous Al2O3 layer for lithium–sulfur battery.* Journal of Materials Chemistry A, 2015. **3**: p. 12213–12219.

12. Jin, J., Wen, Z., Liang, X., Cui, Y., Wu, X., *Gel polymer electrolyte with ionic liquid for high performance lithium sulfur battery.* Solid State Ionics, 2012. **225**: p. 604–607.

13. Zhang, S.S., *Effect of discharge cutoff voltage on reversibility of lithium/sulfur batteries with LiNO3-contained electrolyte.* Journal of the Electrochemical Society, 2012. **159**(7): p. A920-A923.

14. Yin, Y. X., Xin, S., Guo, Y. G., Wan, L. J., *Lithium–sulfur batteries: electrochemistry, materials, and prospects.* Angewandte Chemie, 2013. **52**: p. 13186 – 13200.

15. Liang, X., Wen, Z., Liu, Y., Wu, M., Jin, J., Zhang, H., Wu, X., *Improved cycling performances of lithium sulfur batteries with $LiNO_3$-modified electrolyte.* Journal of Power Sources, 2011. **196**: p. 9839– 9843.

16. Azimi, N., Xue, Z., Hu, L., Takoudis, C., Zhang, S., Zhang, Z., *Additive effect on the electrochemical performance of lithium–sulfur battery.* Electrochimica Acta, 2015. **154**: p. 205–210.

17. Xiong, S., Kai, X., Hong, X., Diao, Y., *Effect of LiBOB as additive on electrochemical properties of lithium–sulfur batteries.* Ionics, 2012. **18**: p. 249–254.

18. Bresser, D., Passerini, S., Scrosati, B., *Recent progress and remaining challenges in sulfur-based lithium secondary batteries – a review.* Royal Society of Chemistry, 2013. **49**: p. 10545--10562.

19. Aurbach, D., Pollak, E., Elazari, R., Salitra, G., Kelley, C. S., Affinito, J., *On the surface chemical aspects of very high energy density, rechargeable Li–Sulfur batteries.* Journal of the Electrochemical Society, 2009. **156**(8): p. A694-A702.

20. Xu, R., Li, J. C., Lu, J., Amine, K., Belharouak, I., *Demonstration of highly efficient lithium–sulfur batteries.* Journal of Materials Chemistry A, 2015. **3**: p. 4170–4179.

21. Rosenman, A., Elazari, R., Salitra, G., Markevich, E., Aurbach, D., Garsuch, A., *The effect of interactions and reduction products of $LiNO_3$, the anti-shuttle agent, in Li-S battery systems.* Journal of the Electrochemical Society, 2015. **162**(3): p. A470-A473.

22. Yang, Y., McDowell, M. T., Jackson, A., Cha, J. J., Hong, S. S., Cui, Y., *New nanostructured Li_2S/silicon rechargeable battery with high specific energy.* Journal of the American Chemical Society, 2010. **10**: p. 1486-–1491.

23. Hassoun, J., Kim, J., Lee, D. J., Jung, H. G., Lee, S. M., Sun, Y. K., & Scrosati, B., *A contribution to the progress of high energy batteries: a metal-free, lithium-ion, silicon–sulfur battery.* Journal of Power Sources, 2011. **202**: p. 308– 313.

24. Fu, Y., Su, Y. S., Manthiram, A., *Li_2S-carbon sandwiched electrodes with superior performance for lithium-sulfur batteries.* Advanced Energy Materials, 2014. **4**: p. 1-5.

25. Wang, L., He, X., Li, J., Gao, J., Fang, M., Tian, G., Fan, S., *Graphene-coated plastic film as current collector for lithium/sulfur batteries.* Journal of Power Sources, 2013. **239**: p. 623e627.

26. Zhang, J. X., Ma, Z. S., Cheng, J. J., Wang, Y., Wu, C., Pan, Y., Lu, C., *Sulfur@metal cotton with superior cycling stability as cathode materials for rechargeable lithium–sulfur batteries.* Journal of Electroanalytical Chemistry, 2015. **738**: p. 184–187.

27. Zhang, Y., Bakenov, Z., Zhao, Y., Konarov, A., Wang, Q., Chen, P., *Three-dimensional carbon fiber as current collector for lithium/sulfur batteries.* Ionics, 2014. **20**: p. 803–808.

28. Cheng, X. B., Peng, H. J., Huang, J. Q., Zhu, L., Yang, S. H., Liu, Y., Zhang, Q., *Three-dimensional aluminum foam/carbon nanotube scaffolds as long- and short-range electron pathways with improved sulfur loading for high energy density lithiumesulfur batteries.* Journal of Power Sources, 2014. **261**: p. 264-270.

29. Urbonaite, S., Poux, T., Novák, P., *Progress towards commercially viable Li–S battery cells.* Advanced Energy Materials, 2015. **5**: p. 1-20.

30. Scheers, J., Fantini, S., Johansson, P., *A review of electrolytes for lithium sulphur batteries.* Journal of Power Sources, 2014. **225**: p. 204-218.

31. Zhang, S. S., Tran, D. T., *How a gel polymer electrolyte affects performance of lithium/sulfur batteries.* Electrochimica Acta, 2013. **114**: p. 296– 302.

32. Wei, H., Ma, J., Li, B., Zuo, Y., Xia, D., *Enhanced cycle performance of lithium−sulfur batteries using a separator modified with a PVDF-C layer.* Journal of American Chemical Society, 2014. **6**: p. 20276−20281.

33. Lin, Z., Liang, C., *Lithium–sulfur batteries: from liquid to solid cells.* Journal of Materials Chemistry A, 2015. **3**: p. 936–958.

34. Sun, J., Huang, Y., Wang, W., Yu, Z., Wang, A., Yuan, K., *Application of gelatin as a binder for the sulfur cathode in lithium–sulfur batteries.* Electrochimica Acta, 2008. **53**: p. 7084–7088.

35. Bao, W., Zhang, Z., Gan, Y., Wang, X., Lia, J., *Enhanced cyclability of sulfur cathodes in lithium-sulfur batteries with Na-alginate as a binder.* Journal of Energy Chemistry, 2013. **22**: p. 790–794.

36. Sun, L., Li, M., Jiang, Y., Kong, W., Jiang, K., Wang, J., Fan, S., *Sulfur nanocrystals confined in carbon nanotube network as a binder-free electrode for high-performance lithium sulfur batteries.* Journal of American Chemical Society, 2014. **14**: p. 4044−4049.

37. Elazari, R., Salitra, G., Garsuch, A., Panchenko, A., Aurbach, D., *Sulfur-impregnated activated carbon fiber cloth as a binder-free cathode for rechargeable Li-S batteries.* Advaned Materials, 2011. **23**: p. 5641–5644.

38. Hagen, M., Dörfler, S., Fanz, P., Berger, T., Speck, R., Tübke, J., Kaskel, S., *Development and costs calculation of lithium sulfur cells with high sulfur load and binder free electrodes.* Journal of Power Sources, 2013. **224**: p. 260-268.

39. Kim, K. R., Lee, K. S., Ahn, C. Y., Yu, S. H., Sung, Y. E., *Discharging a Li-S battery with ultra-high sulphur content cathode using a redox mediator*. Scientific Reports, 2016. **6**(32433): p. 1-7.

40. Brückner, J., Thieme, S., Grossmann, H. T., Dörfler, S., Althues, H., Kaskel, S., *Lithium-sulfur batteries: Influence of C-rate, amount of electrolyte and sulfur loading on cycle performance.* Journal of Power Sources, 2014. **268**: p. 82-87.

41. Manthiram, A., Fu, Y., Su, Y. S., *Challenges and prospects of lithium-sulfur batteries.* Accounts of Chemical Research, 2012. **46**(5): p. 1125–1134.

42. Su, Y. S., Manthiram, A., *A facile in situ sulfur deposition route to obtain carbon-wrapped sulfur composite cathodes for lithium–sulfur batteries.* Electrochimica Acta, 2012. **77**: p. 272– 278.

43. Park, M. S., Yu, J. S., Kim, K. J., Jeong, G., Kim, J. H., Jo, Y. N., Kim, Y. J., *One-step synthesis of a sulfur-impregnated graphene cathode for lithium–sulfur batteries.* Physical Chemistry Chemical Physics, 2012. **14**: p. 6796–6804.

44. Xu, H., Deng, Y., Shi, Z., Qian, Y., Meng, Y., Chen, G., *Graphene-encapsulated sulfur (GES) composites with a core–shell structure as superior cathode materials for lithium–sulfur batteries.* Journal of Materials Chemistry A, 2013. **1**: p. 15142–15149.

45. Zhang, Y., Zhao, Y., Bakenov, Z., Babaa, M. R., Konarov, A., Ding, C., Chen, P., *Effect of graphene on sulfur/polyacrylonitrile nanocomposite cathode in high performance lithium/sulfur batteries.* Journal of the Electrochemical Society, 2013. **160**(8): p. A1194-A1198.

46. Wang, W., Li, G. C., Wang, Q., Li, G. R., Ye, S. H., Gao, X. P., *Sulfur-polypyrrole/graphene multi-composites as cathode for lithium-sulfur battery.* Journal of the Electrochemical Society, 2013. **160**(6): p. A805-A810.

47. Zhao, M. Q., Liu, X. F., Zhang, Q., Tian, G. L., Huang, J. Q., Zhu, W., Wei, F., *Graphene/single-walled carbon nanotube hybrids: One-step catalytic growth and applications for high-rate Li-S batteries.* ACS nano, 2012. **6**(12): p. 10759–10769.

48. Li, S., Xie, M., Liu, J., Wang, H., Yan, H., *Layer structured sulfur/expanded graphite composite as cathode for lithium battery.* Journal of the Electrochemical Society, 2011. **14**(7): p. A105-A107.

49. Zheng, S., Wen, Y., Zhu, Y., Han, Z., Wang, J., Yang, J., Wang, C., *In situ sulfur reduction and intercalation of graphite oxides for Li-S battery cathodes.* Advanced Energy Materials, 2014. **4**: p. 1-9.

50. Han, S. C., Song, M. S., Lee, H., Kim, H. S., Ahn, H. J., Lee, J. Y., *Effect of multiwalled carbon nanotubes on electrochemical properties of lithium/sulfur rechargeable batteries.* Journal of the Electrochemical Society, 2003. **150**(7): p. A889-A893.

51. Yuan, L., Yuan, H., Qiu, X., Chen, L., Zhu, W., *Improvement of cycle property of sulfur-coated multi-walled carbon nanotubes composite cathode for lithium/sulfur batteries.* Journal of Power Sources, 2009. **189**: p. 1141–1146.

52. Chen, J. J., Zhang, Q., Shi, Y. N., Qin, L. L., Cao, Y., Zheng, M. S., Dong, Q. F., *A hierarchical architecture S/MWCNT nanomicrosphere with large pores for lithium sulfur batteries.* Physical Chemistry Chemical Physics, 2012. **14**: p. 5376–5382.

53. Su, Y. S., Fu, Y., Manthiram, A., *Self-weaving sulfur–carbon composite cathodes for high rate lithium–sulfur batteries.* Physical Chemistry Chemical Physics, 2012. **14**: p. 14495–14499.

54. Jozwiuk, A., Sommer, H., Janek, J., Brezesinski, T., *Fair performance comparison of different carbon blacks in lithium-sulfur batteries with practical mass loadings e simple design competes with complex cathode architecture.* Journal of Power Sources, 2015. **296**: p. 454-461.

55. Zheng, J., Gu, M., Wagner, M. J., Hays, K. A., Li, X., Zuo, P., Xiao, J., *Revisit carbon/sulfur composite for Li-S batteries.* Journal of the Electrochemical Society, 2013. **160**(10): p. A1624-A1628.

56. Kim, J., Lee, D. J., Jung, H. G., Sun, Y. K., Hassoun, J., Scrosati, B., *An advanced lithium-sulfur battery.* Advanced Functional Materials, 2013. **23**: p. 1076-1080.

57. Rao, M., Song, X., Cairns, E. J., *Nano-carbon/sulfur composite cathode materials with carbon nanofiber as electrical conductor for advanced secondary lithium/sulfur cells.* Journal of Power Sources, 2012. **205**: p. 474– 478.

58. Zheng, G., Yang, Y., Cha, J. J., Hong, S. S., Cui, Y., *Hollow carbon nanofiber-encapsulated sulfur cathodes for high specific capacity rechargeable lithium batteries.* Journal of American Chemical Society, 2011. **11**: p. 4462–4467.

59. Li, Q., Zhang, Z., Zhang, K., Fang, J., Lai, Y., Li, J., *A simple synthesis of hollow carbon nanofiber-sulfur composite via mixed-solvent process for lithium sulfur batteries.* Journal of Power Sources, 2014. **256**: p. 137-144.

60. Cao, Z., Zhang, J., Ding, Y., Shi, Z., Huo, N., Wang, Q., Yang, S., *Lotus root-like structured carbon fibers as encapsulated sulfur host for lithium sulfur batteries.* Journal of the Electrochemical Society, 2015. **162**(10): p. A2157-A2162.

61. Lee, J. T., Zhao, Y., Kim, H., Cho, W. I., Yushin, G., *Sulfur infiltrated activated carbon cathodes for lithium sulfur cells: The combined effects of pore size distribution and electrolyte molarity.* Journal of Power Sources, 2014. **248**: p. 752e761.

62. Zhang, S., Zheng, M., Lin, Z., Li, N., Liu, Y., Zhao, B., Shi, Y., *Activated carbon with ultrahigh specific surface area synthesized from natural plant material for lithium–sulfur batteries.* Journal of Materials Chemistry, 2014. **2**: p. 15889–15896.

63. Liang, C., Dudney, N. J., Howe, J. Y., *Hierarchically structured sulfur/carbon nanocomposite material for high-energy lithium battery.* Chem. Mater., 2009. **21**: p. 4724–4730.

64. Jiang, S., Zhang, Z., Wang, X., Qu, Y., Lai, Y., Li, J., *Synthesis of sulfur/activated carbon aerogels composite with a novel homogeneous precipitation method as cathode materials for lithium–sulfur batteries.* RSC Adv., 2013. **3**: p. 16318–16321.

65. Wiegmann, A., *GeoDict: virtual microstructure simulator and material property predictor*. 2001-2011.

66. Ryu, H. S., Guo, Z., Ahn, H. J., Cho, G. B., Liu, H., *Investigation of discharge reaction mechanism of lithium|liquid electrolyte|sulfur battery.* Journal of Power Sources, 2009. **189**: p. 1179–1183.